

**On the dynamics of molecular processes:
STM investigations of porphyrins on
Cu(111)**

**Dynamik von molekularen Prozessen:
STM Untersuchungen von Porphyrinen auf Cu(111)**

Der Naturwissenschaftlichen Fakultät
in dem Fachbereich Physikalische Chemie
der Friedrich-Alexander-Universität Erlangen-Nürnberg

zur Erlangung des Doktorgrades Dr. rer. nat.

vorgelegt von

Stefanie Ditze
aus Heilbronn

Als Dissertation genehmigt
von der Naturwissenschaftliche Fakultät
vom Fachbereich Physikalische Chemie
der Friedrich-Alexander-Universität Erlangen-Nürnberg

Tag der mündlichen Prüfung: 20.01.2014

Vorsitzende/r des Promotionsorgans: Prof. Dr. Johannes Barth

Gutachter/in: Priv. Doz. Dr. Hubertus Marbach

Prof. Dr. Alexander Schneider

Contents

1	Introduction	1
1.1	Motivation	1
1.2	Outline of the thesis	4
1.3	Literature review	5
1.3.1	Molecular self-assembly	5
1.3.2	Dynamical processes on solid surfaces	8
1.3.3	Chemical surface reactions	10
2	Fundamentals and techniques	13
2.1	Scanning tunneling microscopy	13
2.2	UHV-Instrument	14
2.2.1	Temperature control	15
2.2.2	Drift compensation	17
2.3	Investigated surfaces and porphyrins	17
2.3.1	Surfaces	17
2.3.2	Porphyrins	19
2.4	Preparation procedures	23
2.4.1	Surface preparation	23
2.4.2	Preparation of porphyrin layers	24
2.4.3	Vapor deposition of nickel	25
2.4.4	Oxygen dosage	25
3	Detailed investigation of dynamic processes of porphyrins on Cu(111)	27
3.1	Reaction rate theory	27
3.2	Experimental challenges	28
3.3	Surface diffusion and molecular rotation of 2HTPP	31
3.3.1	Surface diffusion	31
3.3.2	Molecular rotation	33
3.3.3	Data acquisition	34
3.4	Self-metalation reaction of 2HTPP	34
3.5	Conformational changes of 2HTTBPP	36

4	Results	41
4.1	Adsorption behavior of TPP on Cu(111)	41
4.1.1	Unusual adsorption behavior of 2HTPP [part of P1, P2, P3]	41
4.1.2	Phase separation of two porphyrin derivatives [P1]	49
4.2	Temperature dependent behavior of 2HTPP on Cu(111)	54
4.2.1	Surface diffusion and molecular rotation [P2]	54
4.2.2	Self-metalation reaction [P3, P4, P5]	57
4.2.3	Chemical and structural transformations [P5]	63
4.3	Different aspects of 2HTTBPP on Cu(111) [P6]	67
4.3.1	Adsorption behavior of 2HTTBPP on Cu(111)	67
4.3.2	Thermal activated conformational change	69
4.3.3	Tip-induced conformational change at reduced temperature	73
4.3.4	Self-metalation reaction (unpublished data)	75
4.4	Porphyrins on model-templates [P7]	78
4.4.1	Tetraphenylporphyrins on model-templates	79
4.4.2	Octaethylporphyrin on Ni/Cu(111)	81
5	Summary	85
6	Zusammenfassung	89
7	Literature	93
8	Abbreviations and symbols	96
8.1	Abbreviations	96
8.2	Symbols	96
9	Comparison of kinetic parameters	98
10	List of raw data	100
11	Acknowledgment	101

A	Appendix.....	A 1
P1	Substrate-Mediated Phase Separation of Two Porphyrin Derivatives on Cu(111).....	A 3
P2	Diffusion, Rotation, and Surface Chemical Bond of Individual 2H-Tetraphenylporphyrin Molecules on Cu(111).....	A 15
P3	Abrupt Coverage-Induced Enhancement of the Self-Metalation of Tetraphenylporphyrin with Cu(111)	A 25
P4	Activation Energy for the Self-Metalation Reaction of 2H-Tetraphenylporphyrin on Cu(111).....	A 37
P5	Temperature-Dependent Chemical and Structural Transformations from 2H-Tetraphenylporphyrin to Copper(II)-Tetraphenylporphyrin on Cu(111).....	A 53
P6	On the Energetics of Conformational Switching of Molecules at and Close to Room Temperature.....	A 65
P7	Towards the engineering of molecular nanostructures: local anchoring and functionalization of porphyrins on model-templates....	A 93

1 Introduction

The aim of this introductory chapter is to motivate the work and results presented in this thesis. First, a general introduction into the field of nanotechnology is given, followed by a short outline of the topics of the thesis. At the end of the chapter a brief literature review about the adsorption of large organic molecules on solid surfaces is given with the focus on STM investigations of molecular self-assembly, dynamical processes and chemical surface reactions.

1.1 Motivation

In the last few years the prefix nano- has been probably one of the most popular and widely used buzzword, not only in the scientific community, but also in our daily life to indicate products and systems that have components with dimensions in the nanometer range. [1] Despite this, the exact meaning of nanoscience or nanotechnology is not well defined; the most general definition is related to the development and manipulation of structures with sizes smaller than 100 nm. [2]

Nanotechnology is naturally connected with miniaturization, for example, the outstanding developments in the field of information technology in the last few decades have been related to the progressive miniaturization of components utilized in computer systems. The motivation for this miniaturization is to increase component density, in order to lower production costs through higher yield per chip area and increased performance per device and per integrated circuit. For instance, the smallest physical gate length of transistors in currently produced microprocessors is 25 nm (this is correlated to a 22 nm node). [3] Miniaturization in nanotechnology has usually been achieved by following the top-down approach, using advanced photolithography and related technologies to reduce the structure size in microelectronic components. This miniaturization trend in the semiconductor industry has been quantitatively described for almost 50 years in Moore's law: the number of transistors per area on

integrated circuits doubles every two years. [4] The ultimate limit for miniaturization is the atomic dimension and by interpolating Moore's law this restriction will be reached within the next decades. Therefore, in the near future it will get increasingly difficult to push the top-down lithographic process towards even smaller feature sizes and industry will face the challenge upholding the miniaturization trend.

The bottom-up approach represents a promising strategy to overcome these limitations. Here, devices are built up by their fundamental building blocks, e.g. atoms or molecules. One of the bottom-up strategies is molecular self-assembly. In self-assembly nanostructures or nanostructured materials are built up of molecular building blocks that assemble spontaneously into larger aggregates, due to their molecular recognition. This opens up the perspective to engineer molecular architectures with tailored functionalities. Two main types of self-assembly can be distinguished: (i) non-templated self-assembly, where individual entities interact with each other to produce larger structures without the assistance of external forces or spatial constraints, and (ii) templated self-assembly, where the individual entities interact with each other and an external force or spatial constraint dominates the aggregation. [5] Another strategy of the bottom-up approach is direct positioning of the corresponding molecular building blocks, for example with the tip of a scanning tunneling microscope (STM). [6]

To understand the fundamental principles of the self-assembly process and also of the direct manipulation, appropriate analysis tools and preparation methods are required. Since its invention by G. Binnig and H. Rohrer in 1982 [7, 8] scanning tunneling microscopy has been proven to be an extremely powerful tool for the characterization of adsorbates, e.g. atoms or molecules, on metal surfaces at the atomic scale under defined experimental conditions (i.e. ultra-high vacuum (UHV), single crystal surfaces). In addition to characterization also manipulations, such as pushing and pulling or pick up and release of adsorbates, are feasible with the STM tip. [9-13]

Currently, one research direction concentrates on the development of molecules with specific electronic or chemical properties, which could be used for the fabrication of functional molecular devices. Among the huge number of molecular systems appropriate for such a bottom-up approach, porphyrins represent one of the most

promising candidates for different reasons: they have a high thermal stability and low vapor pressure at room temperature (RT), which enables the sublimation of these molecules under UHV conditions; the synthetic chemistry of porphyrins is well developed and most of all they exhibit versatile functionalities, basically determined by the central metal atom or attached substituents at the porphyrin macrocycle. The latter is illustrated in Fig. 1.1, by two of the most prominent porphyrins in nature. Thereby, the central metal atom as well as the different substituents and environments determine the functionality of the porphyrins. [14] Iron porphyrin in hemoglobin or myoglobin of mammals is responsible for the oxygen transport from the lung to the cells or for the oxygen storage in muscle tissues. In contrast, magnesium porphyrin in chlorophyll *a* is essential for photosynthesis.

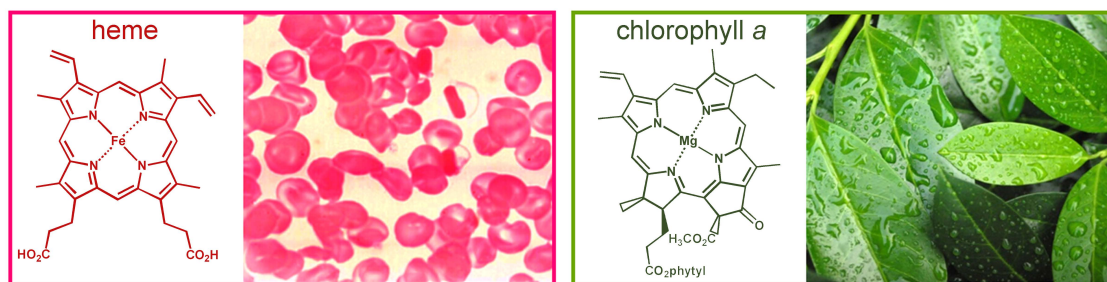


Figure 1.1: Illustration of the two most prominent metalloporphyrins in nature. Modified from [15].

This thesis aims to gain a deeper fundamental understanding of porphyrins on surfaces. In particular, free-base or metalated tetraphenylporphyrins (2HTPP or MTPP, with $M = \text{Co}, \text{Cu}$), free-base octaethylporphyrins (2HOEP) and free-base tetrakisdi-*tert*-butylphenylporphyrins (2HTTBPP), adsorbed on a Cu(111) surface are investigated. Thereby, time-resolved STM measurements in UHV allow a detailed investigation of dynamic processes, such as surface diffusion, molecular rotation, molecular conformational changes or chemical surface reactions. Furthermore, the functionality of templated self-assembly is demonstrated on the basis of two model-templates, that are Cu(111) surfaces pre-covered with a submonolayer of copper oxide or with metallic nickel, on which the selective adsorption and/or localized functionalization of various porphyrins are investigated.

1.2 Outline of the thesis

In Chapter 1 the nanotechnology field is motivated and a short literature review on adsorption of organic molecules studied by STM with focus on molecular self-assembly, dynamic processes and chemical surface reactions is given. A short introduction to the fundamentals of STM and the experimental techniques can be found in Chapter 2. Chapter 3 describes the fundamentals of dynamic processes and the experimental challenges of the STM-Movie technique, used to record these processes. Experimental results are presented in Chapter 4. First, the adsorption behavior of different TPPs on Cu(111) is described at RT in Chapter 4.1 [part of P1-P3]. In Chapter 4.2 time-resolved STM measurements of 2HTPP on Cu(111) at different constant temperatures are presented, allowing for the determination of the kinetic parameters: In the temperature range 280-330 K surface diffusion and molecular rotation of individual 2HTPP molecules is observed [P2] (see Ch. 4.2.1), around 400 K self-metalation of 2HTPP with Cu substrate atoms to form CuTPP occurs [P4] (see Ch. 4.2.2), and above 450 K structural transformations of the in-situ metalated CuTPP molecules are found [P5] (see Ch. 4.2.3). Furthermore, the dependence of the self-metalation reaction on the initial 2HTPP coverage is studied in Chapter 4.2.2 [P3]. Chapter 4.3 addresses the study of a more voluminous porphyrin on Cu(111), that is 2HTTBPP [P6]. These molecules exhibit two different intramolecular conformations, i.e. convex and concave, and they can undergo thermally induced conformational changes. The kinetics of the spontaneous conformational switching is investigated by STM-Movies in the temperature range 280-300 K (see Ch. 4.3.2). Furthermore, the STM tip-induced controlled manipulation from convex to concave is demonstrated at reduced temperature (see Ch. 4.3.3). In Chapter 4.4 it is shown that a Cu(111) surface pre-covered with a submonolayer of copper oxide or with metallic nickel can act as a suitable model-template for selective adsorption and/or localized functionalization of diverse TPP molecules or 2HOEP molecules [P7].

The publications which contribute to this cumulative PhD thesis are attached to the Appendix [P1-P7]. Note that two of them (P3 and P6) are in the review process.

1.3 Literature review

1.3.1 Molecular self-assembly

A major goal in the field of nanotechnology is the basic and comprehensive understanding of the molecular self-assembly on well-defined surfaces under UHV conditions. Applications can already be found in areas such as surface functionalization [16], biosensors [17], molecular electronics [18] and heterogeneous asymmetric catalysis [19]. Molecular self-assembly is defined as the spontaneous association of molecules under equilibrium conditions into stable, structurally well-defined supramolecular architectures joined by non-covalent bonds on surfaces. [20] As mentioned before, two types of self-assembly exist, non-templated and templated self-assembly. [5]

First, the non-templated self-assembly studied with STM will be discussed. The influence of both, the molecule geometry and its chemical structure on the resulting self-assembled arrangement, as well as the role of the substrate type were intensively investigated in the past. Porphyrins were preferentially examined, as these compounds exhibit different functionalities. In particular, a large number of different metal atoms can be coordinated at their center, and a wide variety of meso- or β -substituents can be attached to the porphyrin macrocycle, which leads to a wide range of different electronic and steric properties [21, 22]. In general, porphyrins tend to adsorb flat-lying on the substrate, i.e. the plane of the macrocycle is oriented parallel to the surface plane. [21]

Actually, the substituents attached to the porphyrin macrocycle can strongly influence the resulting supramolecular arrangement and are thus an important factor for the self-assembly. 2H-tetraphenylporphyrin (2HTPP) and 2H-tetrapyrrolylporphyrin (2HTPyP) are very similar and differ only in one carbon atom in each phenyl substituent that is replaced by a nitrogen atom at the para position. However, these rather slight differences lead to different molecular arrangements on Ag(111) at RT; 2HTPP molecules arrange in a long-range square order [23] (see illustration in Fig. 1.2), whereas 2HTPyP molecules arrange in a herringbone structure (not shown here) [24]. This example demonstrates that the variation of the porphyrin substituents is a suitable tool to influence the self-assembly of such supramolecular nanostructures.

Furthermore, the substrate plays an important role for the adsorption behavior and thus for the outcome of the molecular arrangement. As mentioned above, 2HTPyP and 2HTPP form an ordered structure on Ag(111) at RT, whereas both molecules adsorb individually and randomly distributed on Cu(111) and no tendency to the formation of a supramolecular arrangement is observed at RT [25-27] and [P1]. This behavior could be explained in terms of molecule-molecule and molecule-substrate interactions, as depicted in Fig. 1.2 for 2HTPP.

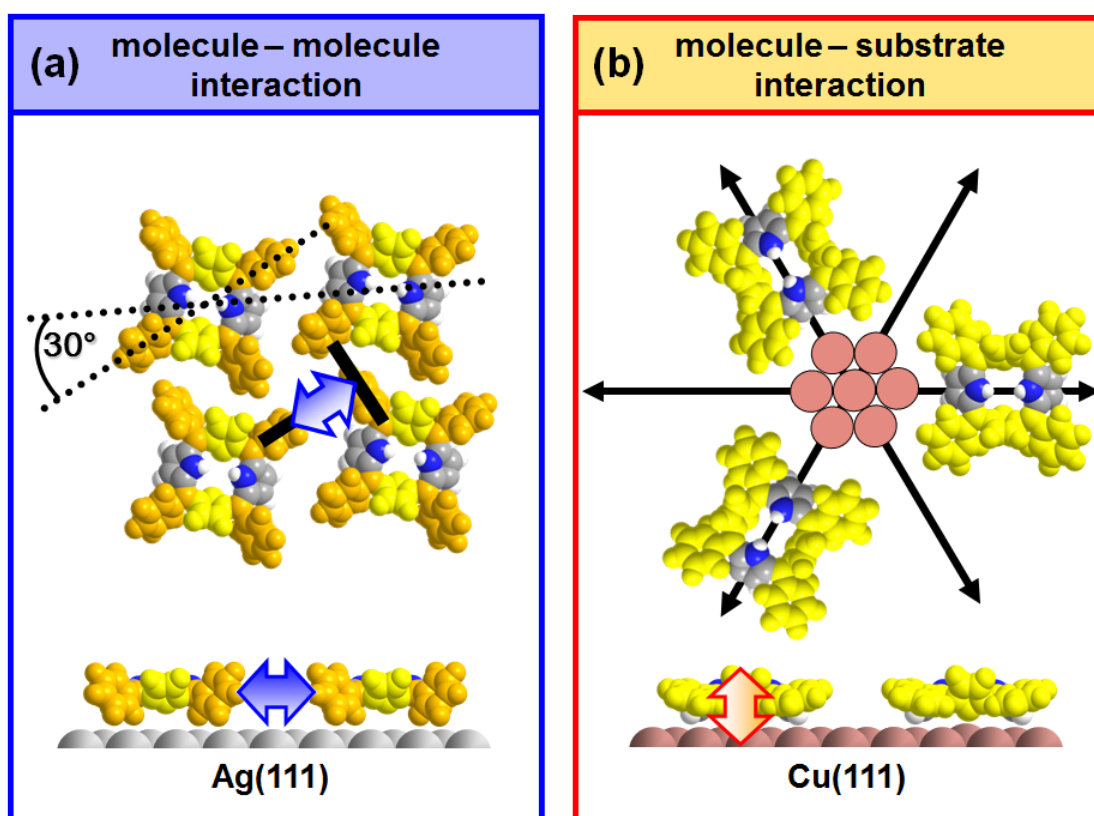


Figure 1.2: Illustration of the adsorption behavior of 2HTPP at RT considering molecule-molecule (blue double-pointed arrow) and molecule-substrate (red double-pointed arrow) interactions. (a) Weak molecule-substrate interactions lead to the formation of ordered structures on Ag(111), due to “T-type” interactions between adjacent molecules. (b) On Cu(111) strong molecule-substrate interaction (between iminic nitrogen atoms of 2HTPP and Cu substrate atoms) hinders the formation of ordered structures and the molecules adsorb as individual molecules aligned along one of the three densely packed Cu substrate rows [P1].

If the interaction between the molecules and the surface is strong, the mobility of the adsorbed molecules can be reduced and the growth of well-ordered structures can be hindered. In contrast, if the molecule-substrate interactions are weak, the molecules are able to diffuse over the surface and the formation of two-dimensional networks is possible, due to molecule-molecule interactions. In the following the domination of molecule-molecule interactions is graphically indicated by a blue double-pointed arrow and the domination of molecule-substrate interactions by a red double-pointed arrow. Indeed, the packing of 2HTPyP [25] and 2HTPP [23] layers on Ag(111) is determined by intermolecular interactions, in particular T-type interactions in the case for 2HTPP (see Fig. 1.2 a), while the orientation of the layers is induced by the coupling to the Ag(111) substrate. In contrast, the adsorption behavior for both molecules on Cu(111) is dominated by strong molecule-substrate interactions. Auwärter et al. postulate that these interactions are mediated by the lone pair electrons of the nitrogen atoms of the functional pyridyl substituents for 2HTPyP. [25] However, for 2HTPP the formation of a strong coordinative bond between the iminic nitrogen atoms of the porphyrin macrocycle and the Cu substrate atoms is assumed [P1, P2]. In addition to the adsorption behavior, 2HTPP and 2HTPyP [27] show the same one-dimensional diffusion behavior with similar energy barriers for diffusion on Cu(111). Thus, it seems to be probable that mainly the iminic nitrogen atoms of the porphyrin macrocycle are responsible for the peculiar behavior on Cu(111). This demonstrates that a subtle balance between molecule-molecule and molecule-substrate interactions controls the adsorption behavior of large organic molecules on well-defined surfaces.

Templated self-assembly introduces an additional element of patterning and therefore to control the position of the molecules, due to molecular recognition. [5] One example to create a patterned surface has been described by Spillmann et al. [28, 29] Here, a zinc-porphyrin with two ditertbutylphenyl and two cyanophenyl groups attached to the porphyrin macrocycle was deposited on Ag(100) and Ag(111) surfaces, which on both surfaces resulted in the formation of an ordered network. The pores of this “template” served then as a host system for guest molecules, such as C₆₀. Templates via controlled oxidation of a Cu(110) surface at high temperatures were

also created, which lead to the formation of alternating one-dimensional bare Cu stripes and (2 x 1)-O reconstructed stripes. On this template π -conjugated organic molecules, like α -quinoxithiophene [30], rubrene [31] or the so called “Lander molecule” [32] were found to adsorb only on the bare Cu areas, due to attractive interaction between the central π -system of the molecules and the metallic surface. Another example is the modulation of surface adsorption of Co(II)-phthalocyanine molecules (CoPc) on a Si(111) surface covered with Pb layers of different thickness: In this system, selective CoPc adsorption is only found on layers of certain thickness, and not on others, which was attributed to quantum-size effects related to the thickness of the Pb layers. [33]

In this thesis, the adsorption behavior of various porphyrins with different functionalities (i.e. 2HTPP, MTPP, 2HOEP and 2HTTBPP) is analyzed at RT on Cu(111) (see Ch. 4.1 and 4.3). Furthermore, the acquired knowledge is used to demonstrate the functionality of templated self-assembly (see Ch. 4.4).

1.3.2 Dynamical processes on solid surfaces

In the past ST-microscopy turned out to be a powerful tool for the study of the surface dynamics of large organic molecules including surface diffusion, molecular rotation and conformational changes, by use of the STM-Movie technique. This technique allows the measurement of rate constants of dynamic processes and if the rates are determined at different temperatures the activation energies and pre-exponential factors are in most cases accessible by using the Arrhenius equation (see Ch. 3).

Surface diffusion of large organic molecules is examined in great detail. The first investigations of surface diffusion by time-resolved STM measurements were performed for acetylene on Pd(111) [34] and on Cu(001) [35], for the asymmetric organic molecule transpyridylvinylbenzoic acid on Pd(110) [36] and for the similar large aromatic molecules decacyclene (DC) and hexatertbutyldecacyclene (HtBDC) on Cu(110) [37]. For the latter two molecules it was found that the diffusion process is dominated by long jumps, i.e. the molecules do not jump from one adsorption site to the nearest neighbor adsorption site. Furthermore, it was demonstrated that a reduction of the molecule-surface interaction caused by six tert-butyl groups raising HtBDC from the surface compared to DC leads to a significant increase of the diffusion

constant. Also more complex systems have been studied such as the lock-and-key effect for the “Violet Lander” molecule on Cu(110) [38] and the wheel-like directional rolling motion for single molecule nanocars on Au(111) [39] and Cu(111) [40]. Recently, it was demonstrated that the diffusion characteristics of molecules adsorbed on Cu(111) strongly depends on molecule-substrate interactions. For example, dithioanthracene is designed such that two thiol groups are linked to the copper substrate [41]. This molecule-substrate interaction leads to an inherently one-dimensional motion of the molecules along one of the three high-symmetry substrate directions. For 2HTPP on Cu(111) an one-dimensional diffusion behavior is observed, which is attributed to a strong molecule-substrate bond [P2]. The dependence of the diffusion on the temperature and the determination of the activation barrier for diffusion are presented in Chapter 4.2.1.

In contrast to the well investigated surface diffusion only a few STM studies were performed on the molecular rotation of large organic molecules on clean surfaces mainly at low temperatures. The first study was performed by Gimzewski et al. for HtBDC molecules, which form an ordered network on Cu(100). [42] Thereby, molecules that are not integrated correctly into the 2D network are able to rotate very fast at RT. In the past, most investigations report the rotation for molecules incorporated in the holes of a molecular network. For instance, CoPc trapped in the pores of a C₆₀ network on Au(111) [43, 44] or Zn(II)-octaethylporphyrins (ZnOEP) trapped in the pores of diaminoperylenequinonediimine network on Cu(111) [45]. For these network systems a dependence of the rotation rate on temperature was found. Recently, a theoretical and experimental study on single thioether molecules with varying length on Au(111) surfaces revealed that the size of the molecules, their flexibility and steric repulsion of the surface are important for the rotation process. [46] The study of the rotation process of 2HTPP molecules adsorbed individually on Cu(111), presented in this thesis (see Ch. 4.2.1), is the first example for the direct observation of rotation of porphyrin molecules around RT on a “native” support [P2].

Moreover, also studies concerning the intramolecular conformation were performed. Many of them focused on the identification or the STM tip-induced manipulation of the molecular conformation. For example Cu(II)-tetrakisdi-tert-butyl-

phenylporphyrins (CuTTBPP) exhibits different intramolecular conformations, when adsorbed on different substrates, such as Cu(100), Au(110) and Ag(110). [47] Besides this, Co(II)-tetrakisdi-*tert*-butylphenylporphyrins (CoTTBPP) molecules arrange in four different molecular conformations on Ag(111), with each arrangement consisting of a distinguishable different intramolecular conformation. [48] Tip-induced manipulation between different conformations was demonstrated for Sn(II)-phthalocyanine molecules adsorbed on Ag(111) at 7 K [49] and for Zn(II)-etioporphyrin I adsorbed on NiAl(110) at 13 K [50]. Only minor focus has been on the investigation of the dynamics of spontaneous conformational changes. [51] In Chapter 4.3 of this thesis the thermal induced conformational changes of 2HTTBPP on Cu(111) will be investigated by time-resolved STM measurements [P6]. Further, the controlled manipulation of the conformation with the STM tip is demonstrated at reduced temperature [P6].

1.3.3 Chemical surface reactions

The metalation reaction of free-based porphyrins with metal atoms on solid surfaces is a very well investigated surface reaction and has gained significant attention in recent years. This high interest on the formation of metalloporphyrin compounds is due to their role in nature, where the functionality of the porphyrin is mainly determined by the central metal atom (see Fig. 1.1), and their potential in technological applications. They are used in colorimetric [52] and transistor-based sensors [53] for organic species, as sensitizer in solar cells [54, 55] or as support on solid surfaces for heterogeneous catalysts [56].

Usually the metalation of free-based porphyrins is realized in one of three ways [57]: (i) by coordination with metal atoms after their deposition onto a porphyrin layer, (ii) by coordination of previously deposited metal-atoms or (iii) by self-metalation, i.e. coordination with substrate atoms without additionally evaporated metal atoms. For the first two ways, the in-situ metalation proceeds at RT or after moderate annealing and was studied in detail by ST microscopy, ST spectroscopy (STS), X-ray photoelectron spectroscopy (XPS) and near edge x-ray absorption fine structure spectroscopy (NEXAFS) for 2HTPP molecules with Co [58], Fe [59-62], Zn [63] and Ce [64, 65] on Ag(111) and Ni [66] on Au(111). The investigations

thereby mainly focused on the chemical reactivity, i.e. which metal species undergoes the metalation reaction, and on the influence of the order of deposition of the reactants. Interestingly, the formation of complexes with Ag- and Au-atoms from the substrate was not detected. The self-metalation was first observed on Cu substrates for 2H-protoporphyrin IX (2HPPIX) on Cu(110) and Cu(100) at RT [67], 2H-tetrabromophenylporphyrin on Cu(111) at 420 K [68], for 2H-diphenylporphyrins and 2H-porphyrin on Cu(110) between 360-420 K [69] and 2HTPP on Cu(111) at 420 K [70]. Recently, the self-metalation of 2HTPP molecules on the highly reactive Fe(110) and Ni(111) surfaces was reported to occur already at RT. [71] The mechanism by which the metal is inserted into a porphyrin has been studied by DFT calculations for 2H-porphyrin in the gas phase and three elementary steps were found: (i) formation of an initial complex in which the metal atom is coordinated by the intact unreduced porphyrin, (ii) successive transfer of the two hydrogen atoms from the aminic nitrogen atoms to the metal atom, where the transfer of the first hydrogen is the rate-limiting step and (iii) formation and release of H₂. [72]

In this thesis the self-metalation reaction of 2HTPP with Cu atoms from a Cu(111) surface is studied depending on the temperature [P4] and the initial 2HTPP coverage [P3]. It will be demonstrated that the metalation reaction could be followed by STM measurements which enables the determination of kinetic parameters and that the reaction rate strongly depends on the initial coverage (see Ch. 4.2.2).

In addition to the metalation reaction also investigations on the formation of networks by coupling coordination of porphyrins with Cu atoms on Au or Cu substrates were reported. 2HTPyP molecules are able to develop a two-dimensional metal-organic coordination network with coadsorbed Cu atoms on Au(111) at RT. Thereby, the 2HTPyP molecules coordinate Cu(0) atoms with the N atoms in the peripheral pyridyl groups, such that one Cu atom links two pyridyl groups of neighboring molecules linearly, and further Cu(0) is also coordinated by the four N atoms of the central porphyrin macrocycle. [73] Haq et al. reported the formation of one-dimensional organometallic wires of 2H-porphyrin, Cu(II)-porphyrin, 2H-diphenylporphyrin and Zn(II)-diphenylporphyrin on Cu(110) upon annealing to high temperatures (>420 K),

which leads to a C-H bond scission at the outer porphyrin core, i.e. a dehydrogenation reaction, and the formation of C-Cu-C bonds between neighboring molecules. [69]

In this thesis the adsorption behavior of 2HTPP on Cu(111) is analyzed upon annealing to higher temperatures up to 500 K. Thereby the molecules undergo three irreversible transformations: first a metalation reaction to CuTPP [P4] (see Ch. 4.2.2) and then two intramolecular structural changes, which are attributed to successive dehydrogenation reactions [P5] (see Ch. 4.2.3).

2 Fundamentals and techniques

2.1 Scanning tunneling microscopy

Scanning tunneling microscopy enables to image structures on the atomic scale in real space on conducting and semiconducting solid surfaces in various environments. The basic idea for the instrumental design of a scanning tunneling microscope came from Young et al. [74]. Binnig and Rohrer built 1982 the first instrument with the ability to resolve atomic surface details. [7, 8, 75] Over the years, STM has proven to be an extremely versatile and powerful technique for many disciplines in condensed matter physics, chemistry, material science and biology. In addition, STM can be used as a tool for nano-fabrication, e.g. manipulation of individual atoms and molecules. [76] In the following the basic STM principles are briefly reviewed, for a complete theoretical treatment the reader is referred to [76, 77].

Scanning tunneling microscopy is based on the quantum-mechanical effect of electron tunneling. It allows an electron to tunnel through a potential barrier (e.g. the gap between tip and surface) even though its kinetic energy is lower than the barrier's height. The scanning tip is a sharp tip made of metal (e.g. platinum iridium (90:10), or tungsten) and is mounted on a piezoelectric scanning unit whose extensions can be controlled precisely in three dimensions x , y , and z . The piezoelectric ceramics in the scanning unit are employed as electromechanical transducers, as they can convert electric signals into mechanical motion in the range from a few Å up to a few μm . [78] The tip is approached toward the surface until a tunneling current I flows. In general, this occurs when the distance d between tip and sample is in the order of roughly 1 nm. The simplified proportional correlation (eq. 2.1) shows the sensitive dependency of the tunneling current from surface distance.

$$I \propto V \cdot e^{-\frac{2d}{\hbar} \sqrt{2m_e \Phi}} \quad (2.1)$$

Φ is the barrier height between tip and sample, m_e is the mass of an electron and V the applied bias voltage between tip and sample. After the tunneling contact is established, the tip scans over the surface (x, y) either by using the constant-current or the constant-height mode. In the constant-current operation mode the height of the tip is adjusted by a feedback controller in such a way that the tunneling current is kept constant. Thus, an image consists of a map $z(x, y)$ of tip height versus lateral position x, y . This mode is mostly used as it allows the scanning of rough surfaces since the distance between the tip and sample is adjusted by the feedback circuit. Alternatively, it is also possible to keep the height of the tip constant during scanning over the surface, then the variation of the tunneling current $I(x, y)$ reflects the atomic corrugation of the surface. This constant-height mode is advantageous if high scan speeds are required, but it is limited to very flat surfaces since a large surface corrugation can cause a crash of the tip.

For all experiments in this thesis the given bias voltage refers to the sample and the STM images are recorded in constant-current mode. The STM raw data is processed with WSxM© [79], typically moderate low pass filtering and background subtraction is applied to the STM data for noise reduction.

2.2 UHV-Instrument

The main parts of the UHV system are the preparation and the analysis chamber separated by a gate valve with a base pressure in both chambers in the low 10^{-10} mbar regime. The set-up is vibration-isolated by three laminar flow stabilizers (*Newport I-2000 series*). In the following, the UHV instrument will be briefly described; for further details the reader is referred to [80] and [81].

The preparation chamber houses various sample preparation and characterization tools like a sputter gun, an *Omicron Focus EFM 3* electron beam evaporator for metal deposition, gas inlets, a *SPECS ErLEED* optics for low energy electron diffraction (LEED) and a quartz crystal microbalance (QCM) for deposition calibration. Additionally, a home-built Knudsen cell evaporator for the deposition of organic

molecules can be introduced into the preparation chamber. The entire evaporator is connected to a separate turbo molecular pump and can be isolated from the preparation chamber by a VAT UHV gate valve, which allows a fast exchange of deposition material without breaking the vacuum of the preparation chamber. The quadrupole mass spectrometer (QMS) is a *Pfeiffer HiQuad QMG700* system, with a mass limit of m/z 2000, which is a prerequisite for the detection of large organic molecules such as porphyrins ($m/z > 500$). Furthermore, the manipulator in the preparation chamber is equipped with a heating and cooling system and temperature readout.

A commercial STM *RHK UHV VT STM 300* system is located in the analysis chamber. The main parts of the commercial STM are the scan head and the sample stage mount. The latter contains the vibrational decoupled sample stage including heating and cooling stage, sample holder and temperature readout. A flow cryostat is connected to the sample stage by several flexible copper braids. Further, a gas dosage system is attached to the analysis chamber; via leak valve and subsequent multi-capillary array-doser gases can be introduced into the UHV system. The STM is controlled by *SPM 100* electronics from *RHK Technologies*, connecting the STM to a PC for data acquisition via a digital interface. A variable gain low noise current pre-amplifier (*FEMTO DLPCA-200*) with a maximum amplification factor of 10^9 V/A in low noise mode is used to measure the very low tunneling currents in the range of 10 pA to 100 pA.

2.2.1 Temperature control

One important aspect in this thesis is the exact adjustment of the sample temperature to determine kinetic parameters of dynamic processes or chemical reactions under isothermal conditions. Thereby, temperatures in the range from 200 up to 500 K are applied using a variable temperature STM.

A radiative heater in form of a retractable tungsten filament placed underneath the sample is used to heat the sample. The sample temperature is directly measured at the substrate using a K-type thermocouple. For accurate temperature adjustment (± 0.1 K) a *Eurotherm 818* controller is employed. The STM is further equipped with a liquid nitrogen continuous flow cryostat allowing sample cooling with liquid N_2 .

However, if the sample cooling is performed with liquid N₂, scanning is in most cases not possible, due to strong vibrations in the system, which can be traced back to boiling nitrogen or turbulences in the line. In order to eliminate these vibrations a setup was developed which allows the cooling with cold N₂ gas (see Fig. 2.1). The setup consists of a 60 L liquid nitrogen vessel with a heating cartridge. The heating cartridge converts the liquid nitrogen to gaseous nitrogen. In order to keep the gas pressure in the vessel constant, the gas pressure is regulated with a *Eurotherm 3216*. Thus a continuous flow of cold N₂ gas is fed to the cryostat by the gas pressure inside the vessel. The flow rate is controlled by a needle valve on the output of the vessel. With this setup sample temperatures, as low as 180 K, can be reached within one hour.

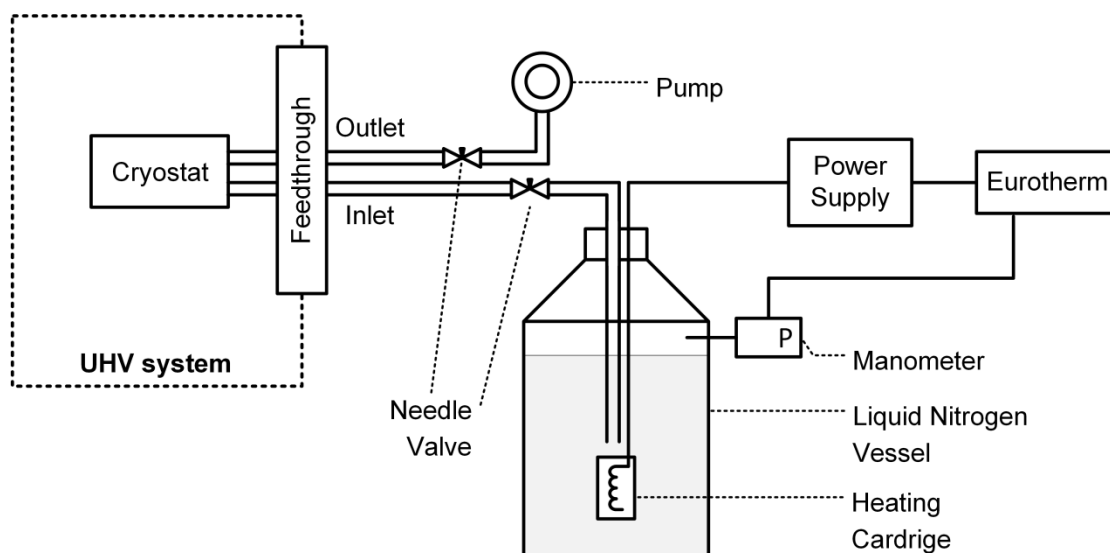


Figure 2.1: Scheme of the new cooling setup.

The achieved sample temperatures (200-500 K) can be maintained constant to within ± 0.1 K. In order to measure the same area on the surface repeatedly for different temperatures (especially for recording STM-Movies), the thermal drift in z and x - y direction has to be reduced with a software-implemented drift compensation routine (see Ch. 2.2.2).

To follow the metalation reaction of 2HTPP with Cu atoms from the Cu(111) substrate (see Ch. 4.2.2), it is necessary to keep the sample at an elevated temperature for an accurate time interval and afterwards to cool the sample temperature down to RT as fast as possible to avoid the unintended progression of the metalation reaction.

Therefore, the sample is heated via a tungsten-filament while the corresponding cryostat is moderately cooled with a constant flow of cold nitrogen gas.

2.2.2 Drift compensation

This thesis addresses the understanding of dynamic processes of porphyrins on surfaces. To obtain an insight into these dynamic processes STM-Movies are recorded which consist of a large number of STM images, taken at the same area on the surface by repeatedly scanning it at fixed time intervals over extended periods of time. To compensate the drift due to thermal or piezoelectric effects during the recording of a STM-Movie, a software-implemented drift compensation routine from *XPMPProTM* is used.

With this software function a characteristic feature or point of interest on the surface can be traced automatically. First, a distinctive feature on the surface (e.g. an immobile molecule, surface defect or crossing of steps) is initially marked and also the size of the area within the feature is searched is set. The position of this feature in the image is determined and the pixel-information in the surrounding area is stored as a reference. Following the acquisition of each image, the position of the characteristic feature in the image is automatically determined by adjusting the defined reference to the image. If this pattern-recognition detects that the position of the characteristic feature has changed compared to the reference, the drift compensation interferes in such a way that the feature is brought closer to the original position in the following image. With this automated software routine it is possible to keep the exact position over many minutes up to hours.

2.3 Investigated surfaces and porphyrins

2.3.1 Surfaces

The adsorption behavior of porphyrins is investigated on a single crystalline Cu(111) surface and on two model-templates, which are Cu(111) surfaces pre-covered with either a submonolayer of copper oxide or metallic nickel.

To understand the adsorption behavior of porphyrins on the different surfaces the knowledge of the atomic arrangement of the surface accompanied by the electronic

properties of the substrate is important. Both copper and nickel crystallize in a face centered cubic (fcc) lattice, which is typical for many coinage metals (see Fig. 2.2 a).

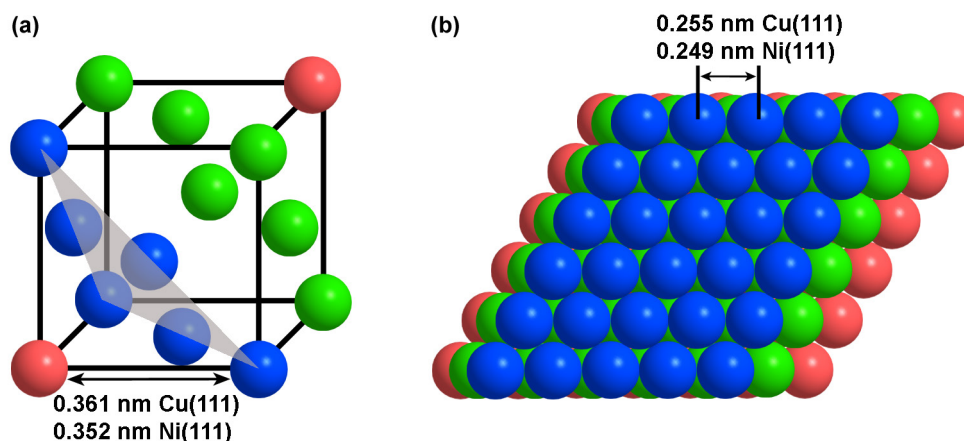


Figure 2.2: (a) Face centered cubic (fcc) crystal lattice with drawn in (111) plane. (b) Top view on the (111) plane.

The lattice parameter for Cu is 0.361 nm and for Ni 0.352 nm. Thus, the next neighbor distance in the close-packed (111)-plane is 0.255 nm for Cu and 0.249 nm for Nickel (see Fig. 2.2 b). Consequently, one can state a very small lattice mismatch between Cu and Ni, i.e. less than 3 %, which enables a heteroepitaxial growth of Ni on Cu(111) and leads to formation of flat two-dimensional Ni islands on the planar Cu(111) surface.

Figure 2.3 (a) depicts a STM image of a clean Cu(111) surface acquired at RT showing large flat terraces of 30-200 nm width. The quality of the freshly prepared Cu(111) is also checked with a LEED. The LEED pattern shows six sharp diffraction spots (see inlet in Fig. 2.3 a), which evidences the long-ranged hexagonal close-packing of the surface. For details of the preparation of the clean Cu(111) surface and both model-templates see Chapter 2.4.1.

Adsorption of Ni onto the Cu(111) surface first leads to the formation of Ni stripes along the Cu step edges and thereafter two-dimensional hexagonal Ni islands are observed on the Cu(111) terraces aligned along the close packed substrate directions (see Fig. 2.3 b). Interestingly, some of the larger Ni islands exhibit smaller islands on top. By STM- and STS-measurements it was shown that the Ni islands are partially

capped by a Cu layer [82, 83], in the following referred to as 2nd story copper layer. The driving force for this is the lower surface energy of Cu compared to Ni. [84-86]

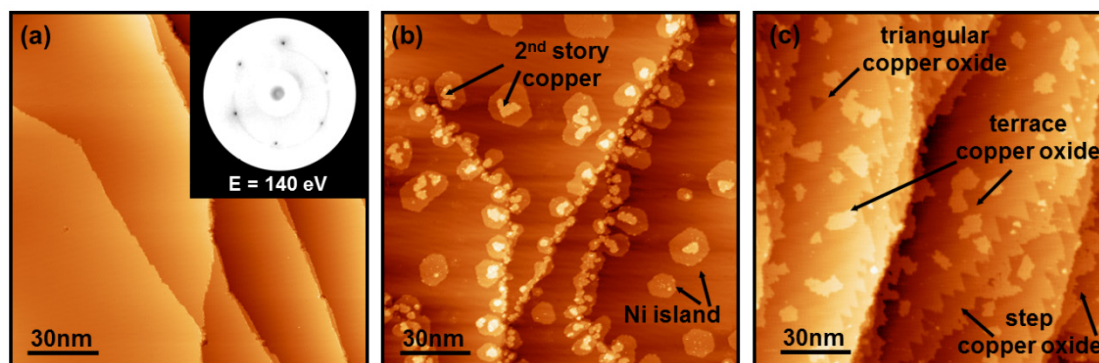


Figure 2.3: Room temperature STM images (a) of a clean Cu(111) surface, with the corresponding LEED pattern, and of Cu(111) surfaces pre-covered with (b) metallic nickel or (c) copper oxide. Tunneling parameters are: (a) $U_{\text{bias}} = -1.00 \text{ V}$, $I_{\text{set}} = 29.1 \text{ pA}$ (b) $U_{\text{bias}} = -1.53 \text{ V}$, $I_{\text{set}} = 30.1 \text{ pA}$ and (c) $U_{\text{bias}} = -1.66 \text{ V}$, $I_{\text{set}} = 40.4 \text{ pA}$.

The oxygen modified Cu(111) surface is shown in Fig. 2.3 (c), with the three characteristic structural features indicated [87, 88]. (i) Initially, triangular structures are formed along the Cu(111) step edge, which are attributed to the formation of two-dimensional disordered copper oxide islands, which grow from the lower step edges into the upper terraces, by consumption of Cu atoms from the upper terrace. (ii) With increasing oxygen exposure dark triangular islands within the Cu(111) terrace evolve; their growth starts from vacancy islands initially present on the terraces. (iii) Finally, at even higher exposures bright islands of arbitrary shape are formed on top of the Cu(111) terrace.

2.3.2 Porphyrins

Porphyrins represent one class of heterocyclic compounds in which the parent macrocycle consists of four pyrrole rings linked together by four methine bridges (see Fig. 2.4). [14] The macrocycle is aromatic as it obeys Hückel's rule for aromaticity and thus porphyrins have highly conjugated π -systems. [89]

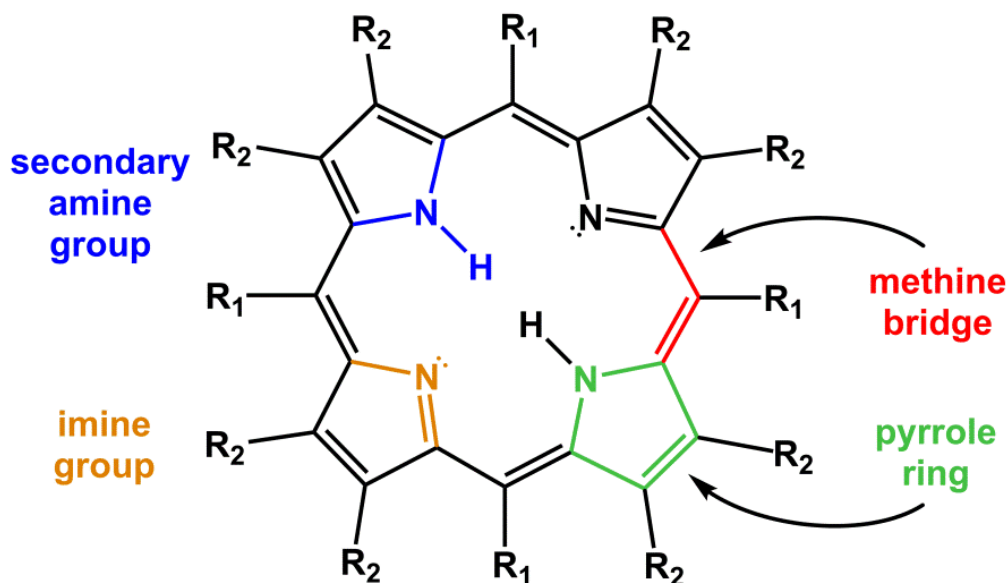


Figure 2.4: Schematic drawing of a porphyrin molecule. Diverse functional groups are color coded.

Because many substituents can be attached to the macrocycle a porphyrin nomenclature is necessary. However, the nomenclature of porphyrins is complex and inconsistent in literature, as there exists the older numbering system of Fischer, which was later replaced by IUPAC and also many trivial and semi-systematic names are in use. The most common nomenclature for porphyrins is as follows: substituents bound to the carbon atom at the methine bridge (R_1 in Fig. 2.4) are called meso-substituents, while substituents attached to the pyrrole rings (R_2 in Fig. 2.4) are referred to as β -substituents. [90] The porphyrins used in this thesis are highly symmetrically substituted, i.e. on all eight β - or on all four meso-positions, which reduces the naming of porphyrins by acknowledging the trivial name of the substituents and their respective number. Therefore, tetraphenylporphyrin (TPP) or tetrakisdi-tert-butylphenylporphyrin (TTBPP) consists of a porphyrin macrocycle with four phenyl- or four di-tert-butylphenyl-rings attached to the meso-position, whereas octaethylporphyrin (OEP) is a porphyrin with eight ethyl groups at the β -positions (see Fig. 2.5).

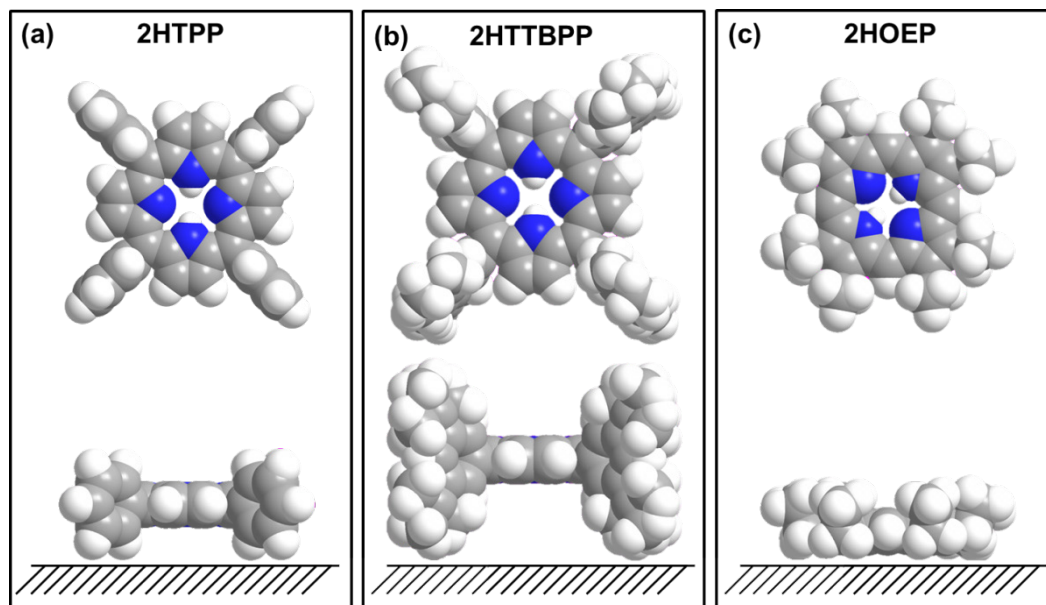


Figure 2.5: Top and side view space filling models of different functionalized 2H-porphyrins.

The porphyrin center can host two hydrogen atoms or one metallic ion. Without such a metal center they are referred to as free-base or 2H-porphyrins. These porphyrins contain two opposite pyrrole rings with secondary amine groups, with N-bound hydrogen atoms, and two opposite pyrrole rings with iminic groups having a lone pair at the nitrogen atom pointing towards the center (see Fig. 2.4). If a metal atom is coordinated by the four nitrogen atoms, the respective metal is added to the name, as in Copper-tetraphenylporphyrin for instance.

In Fig. 2.5 top and side view space filling models of different 2H-porphyrins are shown. Note that the space filling models show the configuration of the porphyrins as intuitively expected in the gas phase and not the internal conformation upon adsorption on a surface, i.e. the phenyl rings of the space filling models are oriented nearly perpendicular to the macrocycle plane. Especially, meso-substituted porphyrins, like TPP, have certain geometrical flexibility upon adsorption on solid surfaces. The internal conformation is described by the dihedral or twist angle θ around the σ -bonds between phenyl rings and macrocycle plane and the tilt angle ϕ of the phenyl rings relative to the macrocycle plane (see Fig. 2.6). [48, 91, 92] Both angles are 0° when the porphyrin core and the phenyl substituents are in plane. Furthermore, TPPs adsorbed on metal surfaces exhibit a saddle-shape conformation of

the macrocycle. Thereby, the central macrocycle is deformed in such a way that two opposite pyrrole rings are tilted upward and the other two downward [62, 64, 93], as illustrated in Fig. 2.6 for 2HTPP and CuTPP on Cu(111). This deformation was reported to be induced by a twisting of the phenyl rings towards the macrocycle plane, which causes a steric repulsion between the *ortho*-hydrogen atoms of the phenyl rings and the β -hydrogen atoms of the pyrrole ring. [47]

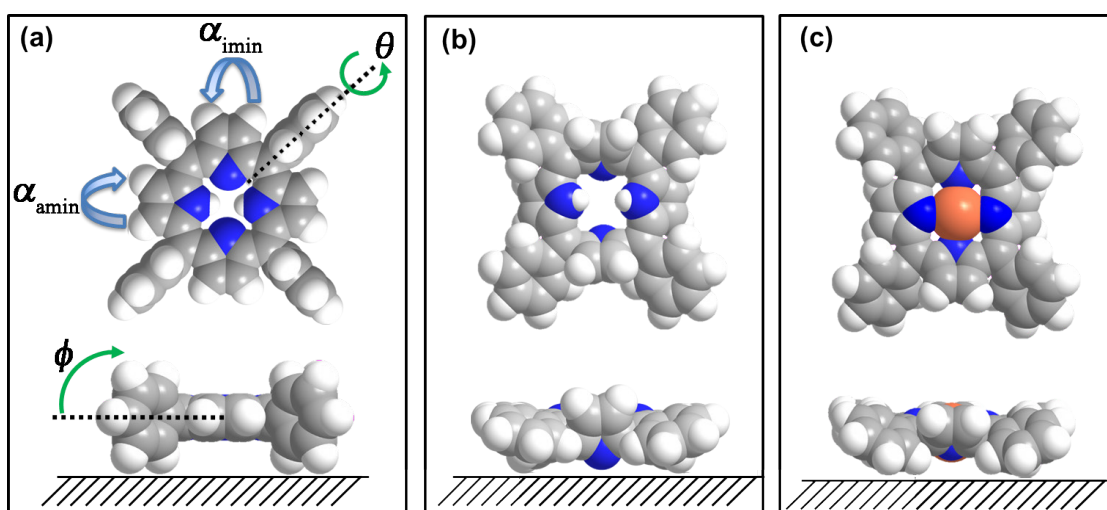


Figure 2.6: (a) Model of a 2HTPP molecule. The angles α_{imin} and α_{amin} describe the inclination of the respective pyrrole rings out of the macrocycle plane, while θ refers to the dihedral or twist angle and ϕ to the tilt angle. (b) and (c) show the internal conformation of 2HTPP and CuTPP upon adsorption on Cu(111). The model in (b) is characterized by $\alpha_{imin} = 60^\circ$, $\alpha_{amin} = 40^\circ$, $\theta = 20^\circ$ and $\phi = 0^\circ$ and the model in (c) $\alpha_{imin} = \alpha_{amin} = 10\text{-}20^\circ$, $\theta = 40\text{-}50^\circ$ and $\phi = 0^\circ$. [70]

In this thesis a variety of free-base and metallo-porphyrins are investigated on Cu(111). All porphyrin compounds were purchased from *Porphyrin Systems* with a specified purity of 98 %, with one exception: 2HTTBPP was synthesized by N. Jux et al. from the Chair of Organic Chemistry II at the Friedrich-Alexander-Universität Erlangen-Nürnberg.

2.4 Preparation procedures

2.4.1 Surface preparation

The substrate used in this work is a Cu single crystal (purity >99.99 % purchased from *MaTeck*) with a polished (111) surface, which is aligned to $< 0.1^\circ$ with respect to the nominal orientation. Minor cleaning cycles of the substrate between the experiments are necessary. First, Ar^+ -ion sputtering ($E = 500 \text{ eV}$) at an argon pressure of $p_{\text{Ar}} = 5 \times 10^{-5} \text{ mbar}$ and a sample current of $I_{\text{sample}} = 1\text{-}3 \mu\text{A}$ and subsequent annealing to 850 K by electron bombardment is applied. More precisely, the crystal is heated with a temperature rate of 1 K/s to 850 K and held at this temperature for 10 minutes and then slowly cooled down to RT with a rate of 0.3 K/s (i.e. to achieve wide terraces and monoatomic steps). During annealing of the sample the manipulator is cooled down to about 170 K using liquid nitrogen. This is necessary, because without cooling a drastic increase of the background pressure occurs as a result of desorption of residual gas from the hot manipulator. The corresponding gases are able to adsorb on the Cu surface, which results in the observation of unsolicited cavities on the surface in STM images, as shown in Fig. 2.7.

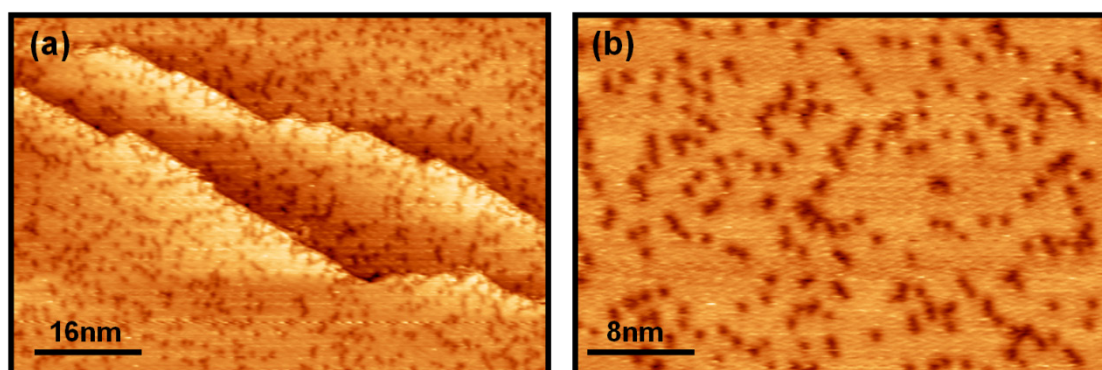


Figure 2.7: Room temperature STM images of Cu(111) after a cleaning cycle without cooling of the manipulator during annealing to 850 K (see Fig. 2.3 (a) for comparison of a clean Cu(111) surface). The tunneling parameters are: (a), (b) $U_{\text{bias}} = -0.43 \text{ V}$, $I_{\text{set}} = 41.6 \text{ pA}$.

2.4.2 Preparation of porphyrin layers

Porphyrins are compounds with a sufficiently low vapor pressure at RT, which allows preparation of molecular layers by means of sublimation at high temperatures under UHV conditions. Note that these sublimation temperatures are too low to decompose the porphyrin molecules. The layers are prepared by vapor deposition with a home-built Knudsen cell evaporator onto the substrate held at RT.

Prior to deposition of porphyrins on a surface, the peak intensity in the mass spectrum of the respective porphyrin is monitored with a QMS to find out the corresponding sublimation temperature. Figure 2.8 shows such a QMS spectrum for 2HTPP. The position of the peaks correlates very well with the theoretical molecular weight of 614.74 g/mol. The peak pattern can be attributed to isotope effects. The molecular weights and the applied sublimation temperatures of the used porphyrins are given in Fig. 2.8. Note that each substance is outgassed in vacuum by heating to 420 K for at least 6 hours, before vapor-deposition is performed. In this thesis the coverage of porphyrins on Cu(111) is given by the molecular density ρ . Thereby, the molecular density is defined as the number of adsorbed porphyrins per surface area.

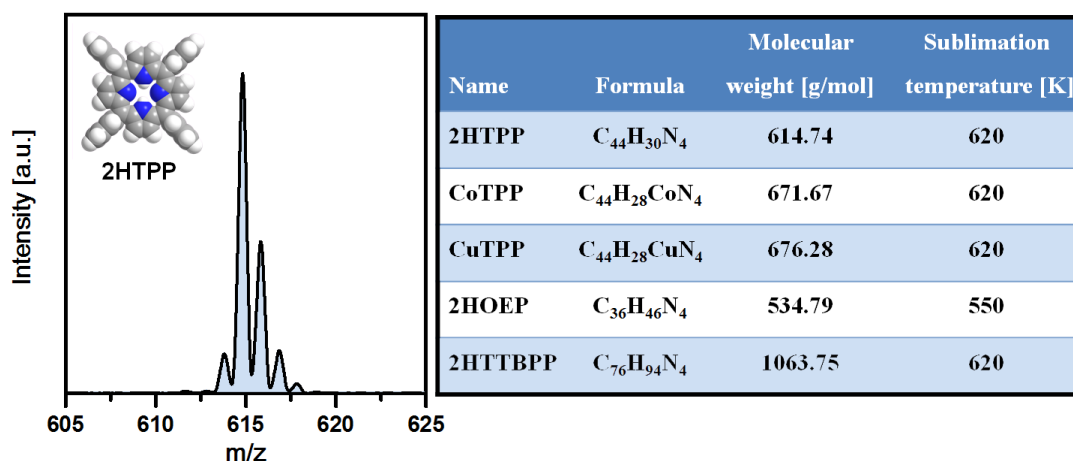


Figure 2.8: Mass spectrum of 2HTPP. The table gives the molecular weights and the applied sublimation temperatures of the porphyrins used in this thesis.

2.4.3 Vapor deposition of nickel

The vapor deposition of nickel onto the Cu(111) surface held at RT is carried out with an electron beam evaporator, which is controlled by *EVC 300* electronics. The evaporation material is a nickel rod with a diameter of 2 mm and a purity of 99 % purchased from *MaTeck*.

The evaporation process is calibrated by using a standard retractable QCM and a *Sycon Instruments STM-100/MF* control unit. At a given setting of the filament, $I_{\text{fil}} = 1.9$ A and $I_{\text{em}} = 17$ mA, and an acceleration voltage of $U = 810$ V, the ion flux is measured. The flux is thereby determined with an ion collector at the beam exit column, and is directly proportional to the flux of evaporated atoms. For the evaporation experiment a stable ion flux of $I_{\text{flux}} = 5$ nA is adjusted and calibrated with the QCM. Finally, a growth rate of 0.13 ML/min is achieved. 1 ML is defined as one Ni atom per surface Cu atom.

2.4.4 Oxygen dosage

Oxygen (purchased from *Linde* with a purity of 99.99 %) is introduced into the UHV-system through a multicapillary array doser at pressures varying between 1×10^{-8} and 1×10^{-7} mbar. The oxygen exposure is given in Langmuir ($1 \text{ L} = 1.33 \times 10^{-6}$ mbar·s). The adsorbed oxygen on the Cu(111) surface held at RT is monitored in-situ with STM to achieve the desired oxygen coverage.

3 Detailed investigation of dynamic processes of porphyrins on Cu(111)

For the design of molecular nanostructures it is important to understand dynamic processes such as surface diffusion, molecular rotation, conformational changes or chemical reactions of large organic molecules on well-defined surfaces. In this regard the determination of the fundamental kinetic parameters such as activation energies and pre-exponential factors are of fundamental importance. Most dynamic processes are thermally activated and as a good approximation can be described by reaction rate theory.

In the following the fundamentals of reaction rate theory, the fundamentals of dynamic processes as well as the experimental challenges and techniques to determine reaction rates with scanning tunneling microscopy are discussed.

3.1 Reaction rate theory

The effect of the temperature on the reaction rate constant k of dynamic processes can be described by the empirically established Arrhenius equation (3.1) [94], given by an pre-exponential factor A and a thermodynamic factor consisting of the Boltzmann constant k_B , the temperature T and the energy barrier for activation E_a .

$$k = A \cdot e^{\frac{-E_a}{k_B T}} \quad (3.1)$$

The pre-exponential factor and the activation energy are usually determined experimentally from the slope ($-E_a/k_B$) and the ordinate intercept ($\ln(A)$) by plotting the natural logarithm of the reaction rate constants ($\ln(k)$) against the corresponding inverse temperature ($1/T$). One drawback of the Arrhenius analysis is that the interpretation of the pre-exponential factor is difficult and does not provide physical

insight into its nature, which is important for example for entropy driven processes. An alternative description, which refers to the transition state theory, is the Eyring equation (3.2) [95], given by the transmission factor κ , the Planck constant h and entropy ΔS^\ddagger and enthalpy ΔH^\ddagger change.

$$k = \kappa \left(\frac{k_B T}{h} \right) \cdot e^{\frac{\Delta S^\ddagger}{k_B}} \cdot e^{\frac{-\Delta H^\ddagger}{k_B T}} \quad (3.2)$$

Provided that the enthalpy and the entropy contributions are both temperature independent, the enthalpy and entropy contributions can be determined experimentally from the slope ($-\Delta H^\ddagger/k_B$) and the ordinate intercept [$\ln(\kappa) + \ln(k_B/h) + (\Delta S^\ddagger/k_B)$] by plotting $\ln(k/T)$ against the corresponding inverse temperature ($1/T$). The determination of the entropy contribution depends on the magnitude of the transmission factor and in most cases the value is assigned to unity [96].

There exists a close analogy between the outcome of the latter analysis and the Arrhenius analysis counterpart [96]:

$$E_a = \Delta H^\ddagger + k_B T \quad \text{and} \quad A = \kappa \left(\frac{k_B T}{h} \right) \cdot e^{\frac{\Delta S^\ddagger}{k_B}} \quad (3.3)$$

3.2 Experimental challenges

The observation of dynamic processes with STM requires sufficient time resolution and thus needs to address STM specific problems, like thermal drift, the finite scanning speed and the influence of the scanning process itself. These problems have been discussed in detail by Morgenstern et al. [97, 98] and therefore only a short description is given in the following.

Finding the appropriate scanning speed is the main problem which arises when STM-Movies are recorded. The scanning speed is limited by the eigenfrequencies of the ST microscope and the control and data-acquisition electronics. Furthermore, the interplay between the scanning speed and the velocity of the dynamic process of the molecules must be considered in order to determine size, intramolecular conformation,

position and azimuthal orientation of the molecules with sufficient precision. This is illustrated in Fig. 3.1 for surface diffusion (a)-(d) and molecular rotation (e)-(f). Three different cases have to be distinguished. (i) The molecule will not be imaged at all or the STM image will show a superposition of all possible orientations, respectively, if the scanning speed is much slower than the movement or the rotational speed of the molecule. (ii) Size and shape of the moving molecule might be observed deformed (see Fig. 3.1 (b), diffusing 2HTPP molecules at 345 K) or a donut-shaped image of the rotating molecule is detected (see Fig. 3.1 (f), rotating 2HTPP molecules at RT) if the scanning speed and the movement or the rotational speed are about equal. (iii) Only if the scanning speed is higher than the movement or the rotational speed of the molecules, the surface diffusion or molecular rotation of the molecule can be monitored correctly from image to image. This is depicted in Fig. 3.1: (c) and (d) show subsequently recorded images of the same area at RT of three diffusing 2HTPP molecules. The molecules appear in the STM image as two elevated parallel rods. The positions of the molecules in (c) are highlighted in (d) with crosses. The dashed lines indicate the direction of the one-dimensional diffusion. The rotation of a 2HTPP at 330 K is shown in Fig. 3.1, where the upper molecule changes the direction from (g) to (h) by 120° . As in this thesis the dynamic processes are studied under isothermal conditions at different temperatures the appropriate scanning speed has to be selected individually for each temperature and the different processes.

Another issue which has to be addressed is the thermal drift of the sample against the tip. In order to measure the same area on the surface by repeated scans over extended time periods (necessary to obtain sufficient statistics) a software-implemented drift compensation routine is used, as described before in Chapter 2.2.2.

Finally, it must be excluded that the observed dynamic process is caused or influenced by the scanning process itself, which is possible for processes with low activation energies [99]. Therefore, the scanning parameters, like tunneling current, tunneling voltage (magnitude and polarity), scanning speed and scanning direction, have to be varied and the experimental values of each measurement have to be compared. Furthermore, the influence of the time of tip-sample interaction must be ruled out.

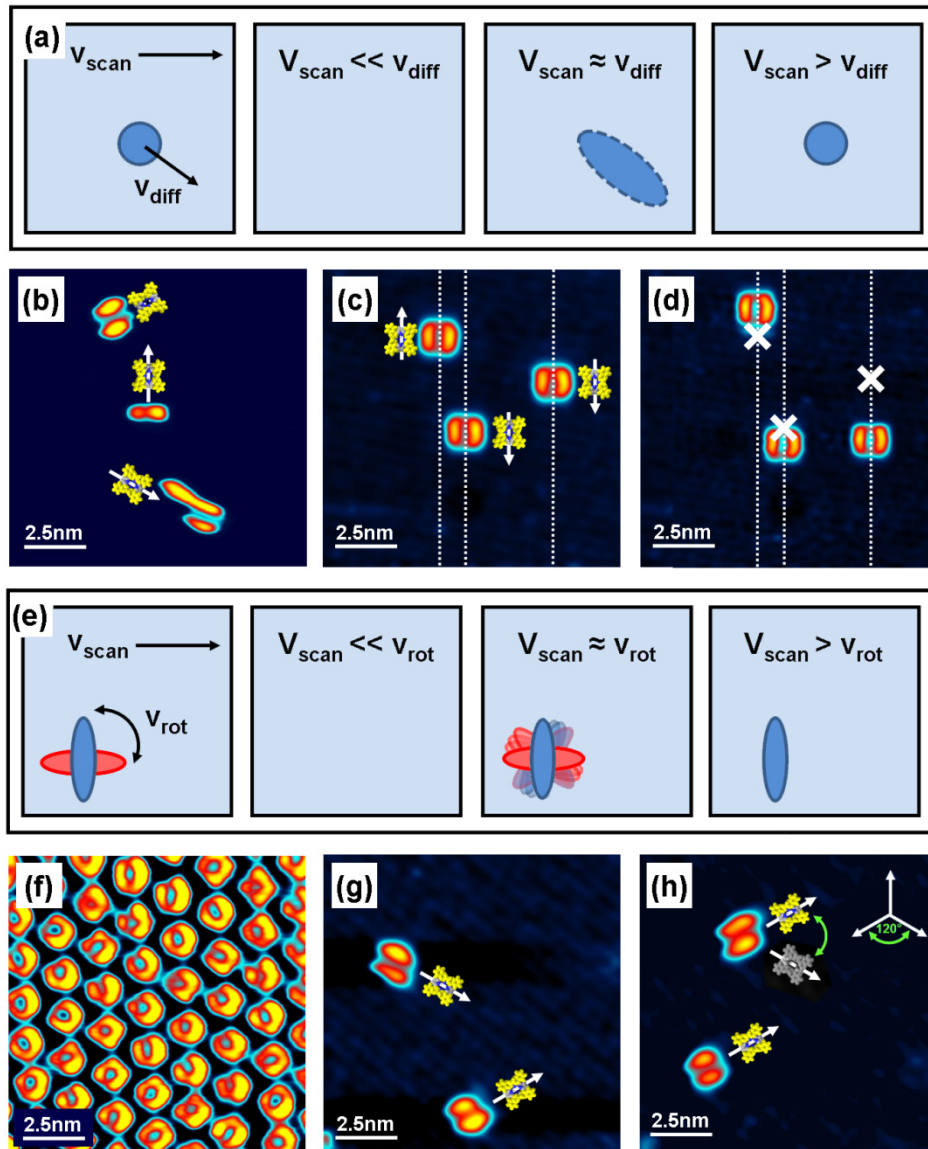


Figure 3.1: Illustration of the interplay between scanning speed and velocity of the dynamic process: Different cases shown for (a) molecule diffusion and (e) molecule rotation. STM images of one-dimensional moving 2HTPP molecules on Cu(111): (b) Scanning speed about equal to the movement, deformed molecules are imaged and (c), (d) subsequent recorded images for the case that the scanning speed is higher than the movement. (f) Donut-shaped image of 2HTPP molecules on Cu(111) for the case scanning speed about equal to rotational speed. (g), (h) showing subsequent recorded images of the same area, demonstrating the change of orientation for the upper 2HTPP molecule. The tunneling parameters are (b)-(d) $U_{\text{bias}} = -1.49 \text{ V}$, $I_{\text{set}} = 29.9 \text{ pA}$ (f) $U_{\text{bias}} = 1.00 \text{ V}$, $I_{\text{set}} = 29.2 \text{ pA}$ and (g)-(h) $U_{\text{bias}} = -1.49 \text{ V}$, $I_{\text{set}} = 30.9 \text{ pA}$.

3.3 Surface diffusion and molecular rotation of 2HTPP

3.3.1 Surface diffusion

Surface diffusion is defined as the movement of adparticles, such as atoms or molecules, over a surface and is involved in many important surface processes: film growth (island growth and self-assembly), chemical surface reactions or heterogeneous catalysis. In this thesis the surface diffusion of 2HTPP molecules on Cu(111) is investigated in great detail [P2]. In general, the diffusion process can be affected by different factors: intermolecular interactions (e.g. repulsion or attraction), interactions between diffusing molecules or between molecules and substrate or the presence of defects on the surface.

On the atomic scale the surface consists of a periodic lattice of potential adsorption sites, which corresponds to the positions of local minima energy (see Fig. 3.2). [78, 100, 101] Diffusion is the dominant process if the adsorption sites are separated by energy barriers being significantly smaller than the energy for desorption E_{des} . The minimum energy difference between adjacent adsorption sites is then referred to as the migration energy barrier E_{m} . Due to thermal excitations, molecules adsorbed on the surface can hop from one adsorption site to another adsorption site.

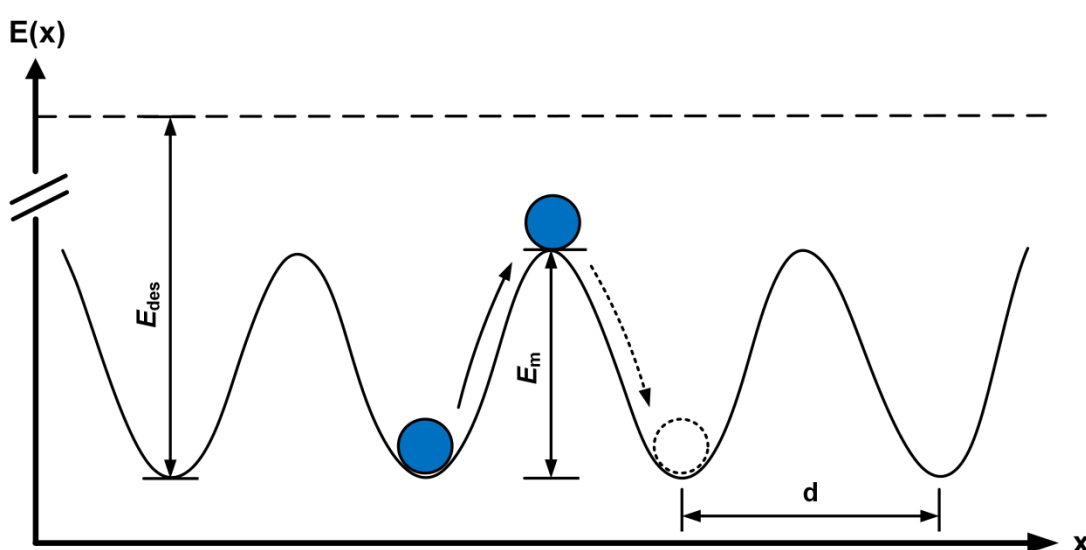


Figure 3.2: Schematic one-dimensional potential energy diagram for the movement of a molecule along a surface.

STM is an experimental technique to directly observe the hopping process of individual molecules on surfaces. Thereby a clear separation of time-scales between the short time-scale on which the actual transition between adsorption sites occurs (picoseconds) [102] and the long time-scale that the molecules resides in the adsorption well between transitions (seconds) is done. The movement of molecules along an isotropic surface can be regarded as a random site-to-site hopping process (random walk) for which the mean-square displacement $\langle(\Delta x)^2\rangle$ of the hopping molecule in time t is given by equation 3.4, with the mean-square jump length λ and the hopping rate $h(T)$.

$$\langle(x_t - x_0)^2\rangle \equiv \langle(\Delta x)^2\rangle = h(T)\lambda^2 t \quad (3.4)$$

Expression 3.4 shows a characteristic property of the surface diffusion, that is $\langle(\Delta x)^2\rangle$ varies linearly with time. Note that the determination of the hopping rate requires statistic averaging over many hopping events. The time-independent diffusion coefficient D is therefore given by equation 3.5:

$$D = \lim_{t \rightarrow \infty} \frac{\langle(\Delta x)^2\rangle}{zt} = \frac{h(T)\lambda^2}{z} \quad (3.5)$$

Where z is the number of adjacent adsorption sites the molecule can hop to. For one-dimensional diffusion (as shown in Fig. 3.5) $z = 2$, for surface diffusion on a square lattice yields $z = 4$ and $z = 6$ for surface diffusion on a hexagonal lattice.

2HTPP molecules on Cu(111) move predominantly along one of the three close-packed substrate directions [P2] and hence $z = 2$. For the analysis of the diffusion it was ensured by the experimental conditions (i.e. very low coverages) that 2HTPP molecules move independently of each other (i.e. they do not interact with each other) and therefore the diffusion coefficient equals to the tracer diffusion coefficient. The latter describes the movement of a single molecule. If the movement of many molecules N is analyzed, the tracer diffusion coefficient is determined by averaging the mean-square displacement over all molecules $i = 1 \dots n$ according to equation 3.6.

$$D = \frac{1}{zNt} \sum_{i=1}^n \langle (\Delta x)_i^2 \rangle \quad (3.6)$$

The hopping process is a thermally activated process (see Ch. 4.2.1, [P2]) and the pre-exponential factor A_m and the energy barrier for migration E_m can be determined by using the Arrhenius equation (equation 3.7) [P2]:

$$h(T) = A_m \cdot e^{\frac{-E_m}{k_B T}} \quad (3.7)$$

If the hopping process of the molecules is restricted to nearest neighbor hops (as is assumed for 2HTPP on Cu(111) [P2]), then λ is equal to the surface lattice constant d , and the diffusion constant is related to the migration energy barrier by equation 3.8:

$$D = \frac{A_m d^2}{z} \cdot e^{\frac{-E_m}{k_B T}} \quad (3.8)$$

3.3.2 Molecular rotation

The molecular rotation could be analyzed by following the methodologies established for the surface diffusion. Due to thermal excitations, molecules adsorbed on surfaces can not only overcome the energy barrier for migration E_m , but also the energy barrier for rotation E_r . This is the case for 2HTPP adsorbed on Cu(111) at elevated temperatures [P2]. As mentioned before 2HTPP molecules move predominantly along one of the three close-packed substrate directions around RT, but increasing of the temperature leads to an occasional rotation of the diffusion direction by $\pm 120^\circ$, that is, rotation to one of the other close-packed substrate directions. The rotation rate $r(T)$ is calculated at different constant temperatures by the number of rotations n_r in a certain time period t (equation 3.9).

$$r(T) = \frac{n_r}{t} \quad (3.9)$$

As the rotation process is also a thermally activated process (see Ch. 4.2.1, [P2]) the pre-exponential factor A_r and the energy barrier for rotation E_r can be determined by using the Arrhenius equation (equation 3.10) [P2]:

$$r(T) = A_r \cdot e^{\frac{-E_r}{k_B T}}. \quad (3.10)$$

3.3.3 Data acquisition

A direct insight into the surface diffusion and molecular rotation of 2HTPP molecules on Cu(111) is achieved by recording STM-Movies. In such STM-Movies the movement or rotation of the molecules becomes clearly visible from image to image. In order to obtain sufficient statistics, the analysis of 2500 diffusion and 30 rotation events, were analyzed. By determination and extraction of the position and the orientation of each molecule in each frame the mean-square displacement $\langle(\Delta x)^2\rangle$ and the number of rotations n_r is calculated, and with the time period t between two successively recorded images the hopping rate $h(T)$ and the rotation rate $r(T)$ is computed after equation 3.4 and 3.9 (Note in equation 3.4 the mean-square jump length λ corresponds to the lattice constant of Cu $d = 0.255$ nm).

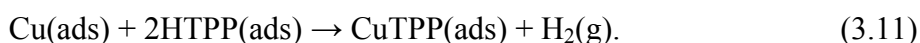
The hopping rate and the rotation rate are calculated for different temperatures, allowing for the determination of the activation energies and the pre-exponential factors for surface diffusion and molecular rotation from Arrhenius plots after equation 3.7 and 3.10, respectively.

3.4 Self-metalation reaction of 2HTPP

The metalation reaction of free-base porphyrins with metal atoms on solid surfaces is a very well investigated surface reaction. However, the determination of the fundamental kinetic parameters presents a great challenge. Up to now activation energies values of metalation reactions of large organic molecules adsorbed on surfaces were derived from temperature-programmed desorption (TPD) measurements

only. [72] Thereby, the Redhead equation was used to deduce the activation energy. A major weakness of this study is that the pre-exponential factor was not determined, but assumed to be 10^{13} s^{-1} .

In this thesis the first direct approach to study the kinetics and to determine the activation energy and the pre-exponential factor for the self-metalation reaction of 2HTPP with Cu substrate atoms on a Cu(111) surface by STM is presented [P3, P4]. The surface mediated reaction follows equation 3.11:



Different factors enable an investigation of the self-metalation reaction with STM. The first and most significant factor is the different adsorption behavior and appearance in STM of the reactant (2HTPP) and the product (CuTPP) on Cu(111) at RT. 2HTPP adsorbs individually and randomly distributed, whereas CuTPP forms an ordered structure above a critical coverage (see Ch. 4.1). This allows following the metalation reaction by determination of the molecular density ρ_t of 2HTPP after certain time intervals t . Two more factors are that the self-metalation reaction occurs at elevated temperatures (in this thesis analyzed between 390 and 410 K) and the reaction proceeds slowly at these temperatures (one to several hours for complete metalation). This allows the stepwise analysis of the progress of the self-metalation reaction under isothermal conditions, i.e. the metalation reaction is stopped after certain annealing time intervals t and after each annealing step the remaining 2HTPP density ρ_t is determined at RT. Note, the annealing and cooling procedure is already described in Chapter 2.2.1. For each annealing step more than 25 independent STM images with a size of $61 \times 61 \text{ nm}^2$ of different surface areas are analyzed to obtain sufficient statistics.

The self-metalation reaction is assumed to be a pseudo-first order reaction, since the concentration of one reaction partner, namely the Cu atoms, remains constant because of the infinite reservoir in the Cu(111) crystal. Thus, the reaction follows equation 3.12.

$$\frac{\rho_t}{\rho_0} = e^{(-k_T \cdot t)} \quad (3.12)$$

For each temperature the ratio of the densities of 2HTPP (ρ_t/ρ_0) depends on the annealing time t and the metalation rate k_T . With the metalation rates determined at different temperatures and by using the Arrhenius equation 3.13 the activation energy E_a and the pre-exponential factor A_S for the self-metalation reaction can be determined.

$$k_T = A_s \cdot e^{\frac{-E_s}{k_B T}} \quad (3.13)$$

Note that the self-metalation reaction strongly depends on the initial 2HTPP density ρ_0 [P3]. Therefore, the determination of the metalation rates at different temperatures and therewith the determination of the activation energy should be done for similar initial densities as in [P4].

3.5 Conformational changes of 2HTTBPP

The geometrical flexibility of tetraphenylporphyrins enables the formation of different intramolecular conformations upon adsorption on solid surfaces. The transition between the conformations is stated as conformational change. In this thesis the thermal induced reversible conformational change of 2HTTBPP on Cu(111) is investigated [P6]. Thereby the focus lies on the determination of the fundamental kinetic parameters.

2HTTBPP adsorbs on Cu(111) at RT with two different intramolecular conformations, arranged in rows as shown in Fig. 3.3 (a) by the high resolution STM image. The molecules with the bright center exhibit a convex conformation and the molecules with the central cavity a concave conformation. Further details of the intramolecular conformation of 2HTTBPP can be found in Chapter 4.3. Within the rows the molecules are able to change their conformation reversibly. This is shown exemplarily in Fig. 3.3 (a) for two subsequent recorded STM images.

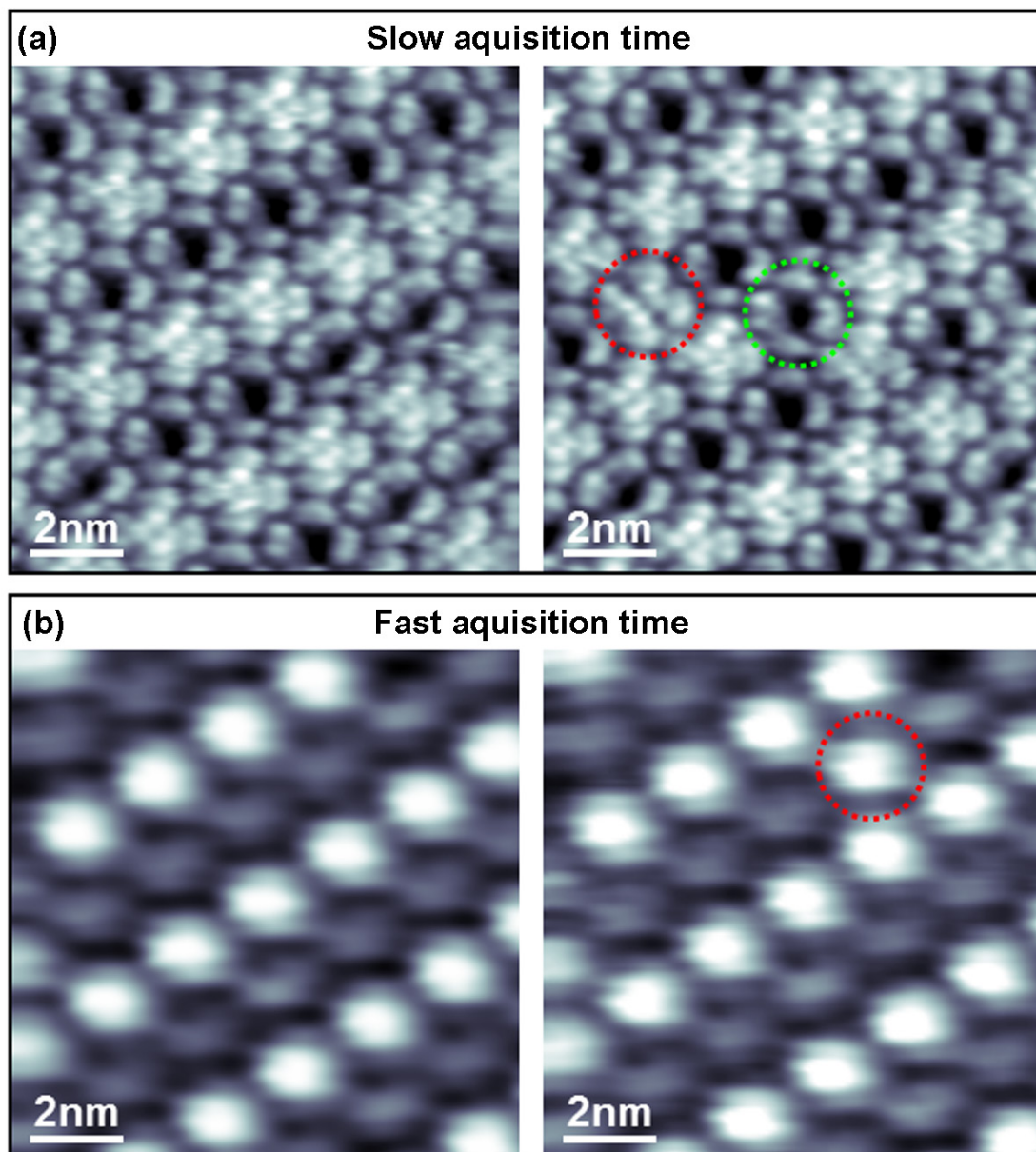


Figure 3.3: Subsequently recorded STM images of 2HTTBPP adsorbed on Cu(111) at RT for different acquisition times: (a) long image-to-image acquisition time of 15 s allows for submolecular resolution and (b) short image-to-image acquisition time of 1.8 s with reduced molecular resolution. In all STM images the arrangement in rows of the two different 2HTTBPP conformations, i.e. convex (bright molecules) and concave (dark molecules), is clearly visible. Conformational changes of convex (green circle) and concave (red circle) molecules are indicated. The tunneling parameters are: (a)-(d) $U_{\text{bias}} = 1.30 \text{ V}$ and $I_{\text{set}} = 29.9 \text{ pA}$.

The kinetic analysis of the conformational change is done by recording STM-Movies under isothermal conditions at different temperatures. The selected acquisition time for the STM-Movies is the result of a compromise between the possibility to distinguish the two conformations and the possibility to record as quickly as possible many molecules simultaneously (here about 24 molecules: 12 convex and 12 concave). Thus, the resolution was reduced to 128 x 128 pixels and the scan speed increased to 2.22 $\mu\text{m/s}$. As a result a short image-to-image acquisition time of 1.8 s is achieved for a scan area of 12 x 12 nm^2 . (In contrast, STM-Movies for the diffusion of 2HTPP are recorded at a resolution of 512 x 512 pixels with an acquisition time of around 15 s for a scan area of 12 x 12 nm^2 , i.e. with a scan speed of 0.99 $\mu\text{m/s}$). Such a fast acquisition time goes at the expense of the image quality. However, the different intramolecular conformations can still be distinguished, i.e. the convex molecules are observed as bright and the concave molecules as dark spots, as shown in Fig. 3.3 (b).

As $h(t)$ -profiles have a significant higher time-resolution (1 ms/point) this scan method is used to confirm the appropriate scanning speed for the STM-Movies. Thereby, the STM tip is placed directly over a molecule of interest and the height h is recorded versus time t (see scheme in Fig. 3.4 a). This allows following the conformational changes of one molecule and to determine the lifetimes in the two conformations. Recorded at different temperatures Fig. 3.5 shows $h(t)$ -profiles over a concave molecule in a concave row. The shortest lifetime of the convex state measured at 296 K (see Fig. 3.4 b) is about 5.57 s and at 320 K about 0.04 s (see Fig. 3.4 c). Analogue measurements were performed for convex molecules in convex rows, showing the same trend for the concave state. As a result investigations of temperatures in the range from 280 to 300 K are possible by using the STM-Movie method. Below 280 K conformational changes are too rare and above 300 K the lifetimes of the unfavored conformations are too short to be recorded, i.e. most events are missed.

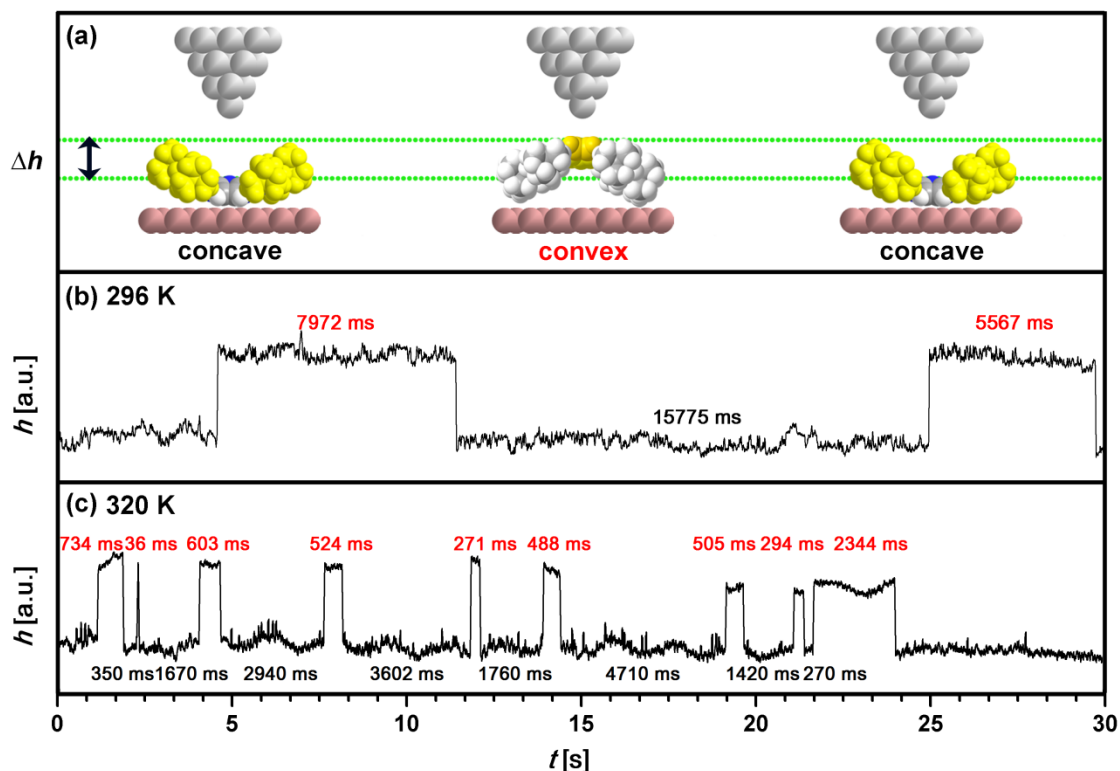


Figure 3.4: (a) Sketch of the conformational change of a concave molecule in a concave row, with the height difference Δh between the concave and the convex conformation indicated. If the STM tip is placed directly over this molecule the height h can be recorded versus the time t , allowing the acquisition of the conformational changes. $h(t)$ -profile at (b) 296 K and (c) 320 K. Height difference for both profiles is about $\Delta h \sim 0.08$ nm.

To obtain sufficient statistics for the analysis of the kinetic parameters many STM-Movies of different surface areas are gathered at a specific constant temperature. The analysis of the STM-Movies, i.e. the detection of the conformation of each molecule in each image, is done by a software-implemented evaluation tool from A. Aichert from the Chair of Pattern Recognition at the Friedrich-Alexander-Universität Erlangen-Nürnberg. With this information the transition rate $\nu(T)$ is calculated separately for the convex (cvx) and the concave (ccv) row and within the rows it is distinguished between the transition from convex to concave and vice versa. Thereby only complete transition events were considered, i.e. transition from the convex state into the concave state and back to the convex state and vice versa. This is necessary to evaluate the corresponding lifetime of the unfavored state and ensures

that the transition process of the molecule is intact. The transition rate is determined after equation 3.14 and 3.15 by dividing the number of transitions n through the corresponding lifetime t :

$$v(T) = \frac{n_{cvx \rightarrow ccv}}{t_{cvx}} \quad \text{or} \quad (3.14)$$

$$v(T) = \frac{n_{ccv \rightarrow cvx}}{t_{ccv}}. \quad (3.15)$$

To gain a deep fundamental understanding of the transition process, the Eyring equation (3.16) is used to determine the enthalpy and entropy contributions to the transition process for both rows from convex to concave and vice versa.

$$v(T) = \kappa \cdot \frac{k_B T}{h} \cdot e^{\frac{\Delta S^\ddagger}{k_B}} \cdot e^{\frac{-\Delta H^\ddagger}{k_B T}} \quad (3.16)$$

Note that at the specific tunneling conditions used for the STM-Movies (here: $U_{\text{bias}} = +1.30 \text{ V}$ and $I_{\text{set}} = 30.0 \text{ pA}$), the conformational change is not significantly caused or influenced by the scanning process. At higher bias voltages ($> +1.70 \text{ V}$) tip-induced transition occurs (see Ch. 4.3.3) and at bias voltages larger than $+2.30 \text{ V}$ the molecular arrangement is destroyed.

4 Results

4.1 Adsorption behavior of TPP on Cu(111)

In this chapter, the adsorption behavior of 2HTPP [part of P1, P2 and P3], metalated tetraphenylporphyrins MTPP (with M = Cu, Co) [P1] and mixtures of 2HTPP/MTPP [P1] on a Cu(111) surface at RT is discussed. Thereby, the role of the specific contributions of molecule-molecule (indicated by a blue arrow) and molecule-substrate interactions (indicated by a red arrow) is addressed. The corresponding knowledge is an important prerequisite for the design of tailored supramolecular networks. Valuable insight on the role of the substrate will be gained, by comparing results on Cu(111) with those on Ag(111). Furthermore, the coverage dependence of the molecular ordering process is investigated to obtain direct insights into the self-assembly process. Moreover, the internal conformation of the different TPP molecules is derived from STM images with submolecular resolution.

4.1.1 Unusual adsorption behavior of 2HTPP [part of P1, P2, P3]

Previous STM studies of 2HTPP on Ag(111) have shown that the molecules adsorb coplanar to the surface and form square ordered islands on the surface [81] already at submonolayer coverage [26] at RT. Figure 4.1 shows an STM image of a 2HTPP monolayer (i.e. the surface is entirely covered with 2HTPP); the lattice constants of the square arrangement are $a = b = 1.40 \pm 0.05$ nm as indicated, which results in a molecular density of $\rho = 0.510$ mol/nm². The specific appearance of an individual 2HTPP molecule within an island in STM is the result of the saddle-shape conformation [23, 93] explained in detail in Chapter 2.3.2. Each 2HTPP appears with four lobes and two longish protrusions close to the central cavity (see Fig. 4.1). The latter originates from the distortion of the macrocycle and the lobes are interpreted as twisted phenyl legs. The twist angle was derived by Buchner et al. in a combined experimental and theoretical work to be around $\theta = 60^\circ$. [103] In general, on Ag(111)

isolated 2HTPP molecules are highly mobile at RT, which allows for the formation of ordered islands above a critical coverage. The arrangement is dominated by molecule-molecule interactions, i.e. T-type interactions between the phenyl rings of adjacent porphyrins stabilize the 2HTPP molecules in a square lattice (see Fig. 1.2). The same square arrangement is reported for MTPP molecules ($M = \text{Co}, \text{Zn}, \text{Fe}$) on Ag(111). [23, 104, 105]

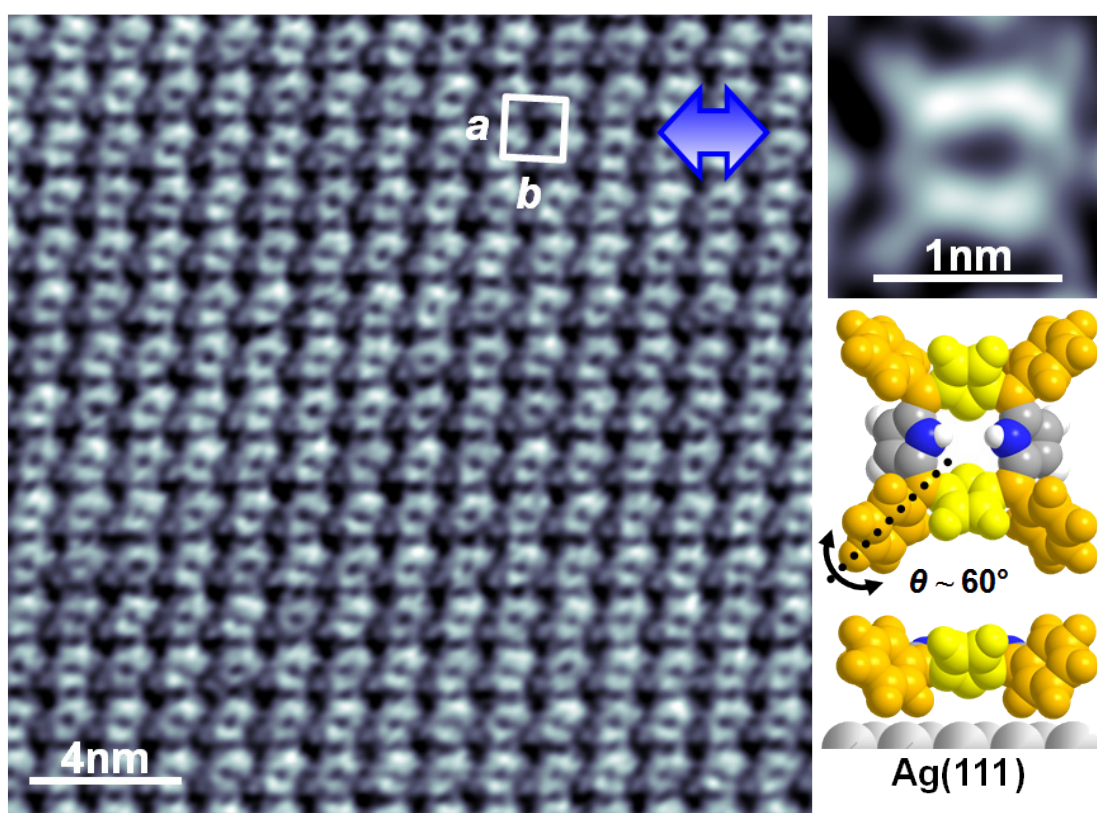


Figure 4.1: STM image with submolecular resolution of square ordered 2HTPP layer on Ag(111) at RT with a molecular density of $\rho = 0.510 \text{ mol/nm}^2$. Top and side view space filling model of 2HTPP illustrating the intramolecular conformation: the two bent up pyrrole rings (marked yellow) and the twisted phenyl rings (marked orange) determine the appearance in STM. The tunneling parameters are: $U_{\text{bias}} = +0.45 \text{ V}$ and $I_{\text{set}} = 25.0 \text{ pA}$.

In contrast, a different adsorption behavior is found for 2HTPP on Cu(111) at RT. Figure 4.2 shows isolated adsorbed 2HTPP molecules at low coverage with a molecular density of $\rho = 0.150 \text{ mol/nm}^2$. Each 2HTPP molecule appears as two

elevated parallel rods, and the central longish gap in between is denoted in the following as the molecular main axis. Interestingly, the analysis of large surface areas reveals three distinct azimuthal orientations of this molecular main axis, rotated by multiples of 120° (see Fig. 4.2). Furthermore, the azimuthal orientations of 2HTPP on the terraces coincide with the orientation of the monoatomic steps of the substrate. These findings are a strong indication for the alignment of the molecules along one of the three densely packed Cu substrate rows, as indicated in Fig. 4.2 by the white arrows representing the crystallographic directions of Cu(111).

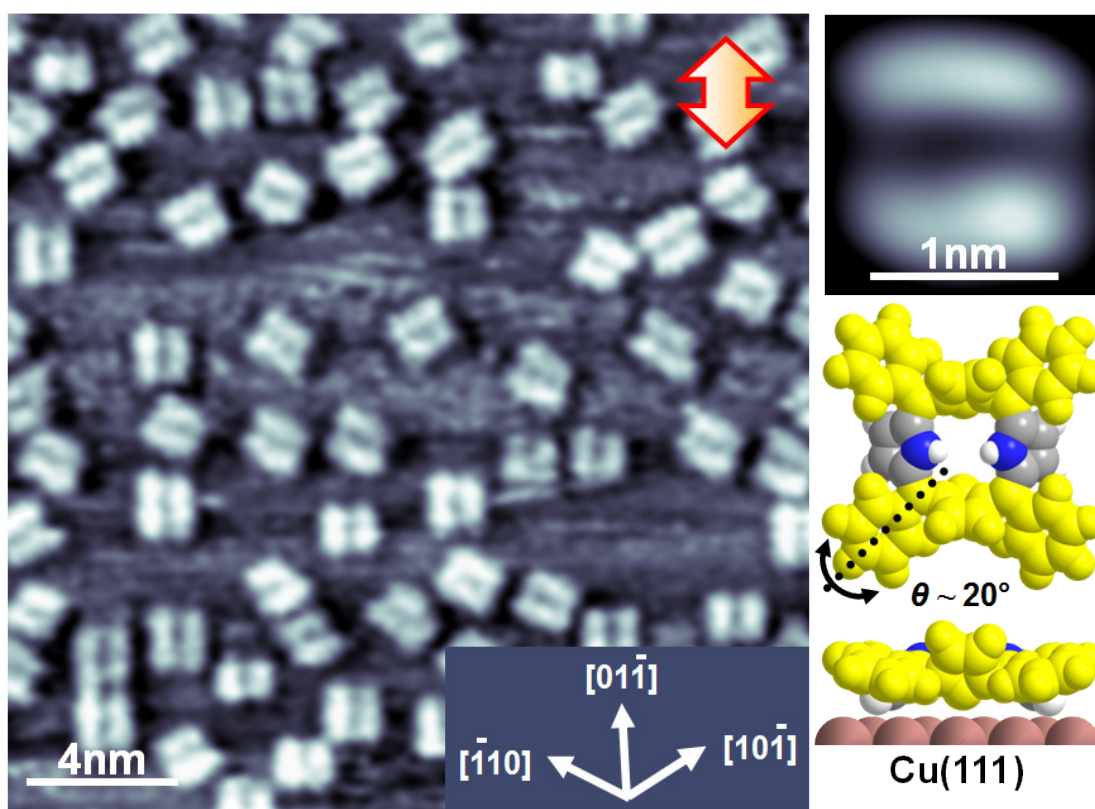


Figure 4.2: STM image of isolated 2HTPP molecules on Cu(111) at RT with a molecular density of $\rho = 0.150 \text{ mol/nm}^2$. The white arrows represent the crystallographic directions of Cu(111). Top and side view space filling model of 2HTPP illustrating the intramolecular conformation: the two bent up pyrrole rings and the twisted phenyl rings (marked yellow) determine the appearance in STM. The tunneling parameters are: $U_{\text{bias}} = -0.77 \text{ V}$ and $I_{\text{set}} = 26.4 \text{ pA}$.

In this regard, a statistical analysis of the orientation of the molecules reveals that the orientations of the molecules are equally distributed at least for small intermolecular distances (< 2.5 nm from molecule center to center), i.e. the molecules are statistically oriented at low coverages. The fact that 2HTPP can be imaged at RT as individual molecules indicates a highly site-specific molecule-substrate interaction. This interaction is attributed to a local coordination of the iminic nitrogen atoms of the porphyrin macrocycle with underlying copper substrate atoms, due to a high affinity of nitrogen and copper. As a consequence of this site-specific interaction the porphyrin macrocycle is pulled towards the surface, resulting in a nearly flat conformation with the phenyl rings oriented almost parallel to the Cu substrate (see Fig. 4.2). Recently, Diller et al. derived the intramolecular conformation for monolayer 2HTPP on Cu(111) from NEXAFS and DFT measurements [70], which confirms the proposed conformation. The iminic pyrrole rings are bent out of the porphyrin macrocycle plane by $\alpha_{\text{imin}} = 60^\circ$ pointing towards the surface and the aminic pyrrole rings are bent out of the plane by $\alpha_{\text{amin}} = 40^\circ$ pointing away from the surface. This strong deformation of the porphyrin macrocycle goes along with rather small twist angles of the phenyl rings of $\theta = 20^\circ$. This explains the specific appearance of 2HTPP on Cu(111) in the STM image: the elevated parallel rods are attributed to the four phenyl rings and the two opposite iminic pyrrole rings, as indicated in Fig. 4.2 by the corresponding space-filling model.

Moreover, STM-Movies reveal that the molecules diffuse comparably slow at RT. In Fig. 4.3 (a) a RT-STM image of the area at which the STM-Movie is recorded and the corresponding average image from the recorded STM-Movie (superposition of the image series, see Fig. 4.3 b) at RT is depicted. The molecules in the average frame appear as an elongated version of the two parallel rods of the single frame in Fig. 4.3 (a), reflecting a one-dimensional diffusion, i.e. they diffuse along one of the three densely packed Cu substrate rows and the diffusion direction is defined by the azimuthal orientation of the molecules. A detailed analysis of the diffusion of 2HTPP on Cu(111) in dependence of the temperature is presented in Chapter 4.2.1. The observed diffusion behavior is in good agreement to the strong site-specific interaction, i.e. the strong interaction between the molecules and the copper surface hinders the molecules to move freely over the surface. Summarizing the STM

observations for low coverages of 2HTPP on Cu(111), the adsorption behavior is dominated by site-specific molecule-substrate interactions.

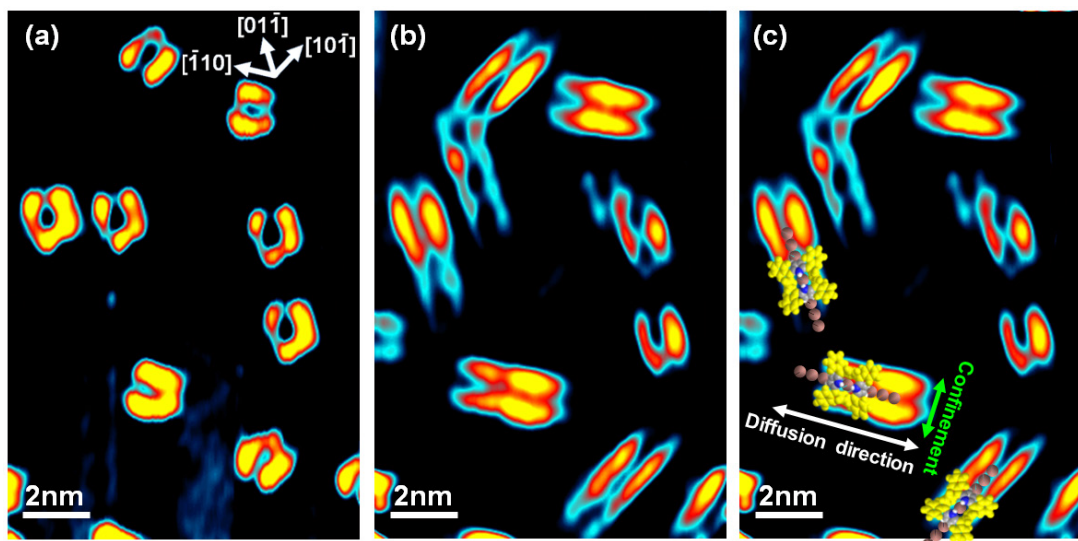


Figure 4.3: (a) Single STM image and (b) average image extracted from a STM-Movie consisting of 80 images (33 min) recorded at RT. The one-dimensional movement along one of the three densely packed Cu rows (axis indicated by white arrows) is visible in the average image as the elongated shape of the molecules. (c) Superimposed space filling models indicate the diffusion direction. The tunneling parameters are: (a)-(c) $U_{\text{bias}} = -1.18 \text{ V}$ and $I_{\text{set}} = 25.2 \text{ pA}$.

To support the STM observations and to obtain direct information about the bonding situation also XPS measurements in the N 1s region of 2HTPP on Au(111), Ag(111) and Cu(111) are performed by our cooperation partners J. Xiao, M. Chen and M. Gottfried from the Chair of Physical Chemistry II at the Friedrich-Alexander-Universität Erlangen-Nürnberg. [P2] The spectra in Fig. 4.4 show two distinct peaks, which are assigned to two different pairs of nitrogen atoms of 2HTPP: aminic nitrogen (at higher binding energies) and iminic nitrogen atoms (at lower binding energies). On Cu(111) a reduced peak separation of 1.5 eV is observed (compared to 2.0 eV on Au(111) and Ag(111)), because the peak related to the iminic nitrogen atoms shifts to higher binding energies. This result indicates a specifically strong interaction of the iminic nitrogen atoms with the Cu surface. Furthermore, the full width at half maximum (fwhm) of the individual peaks is also reduced on Cu(111).

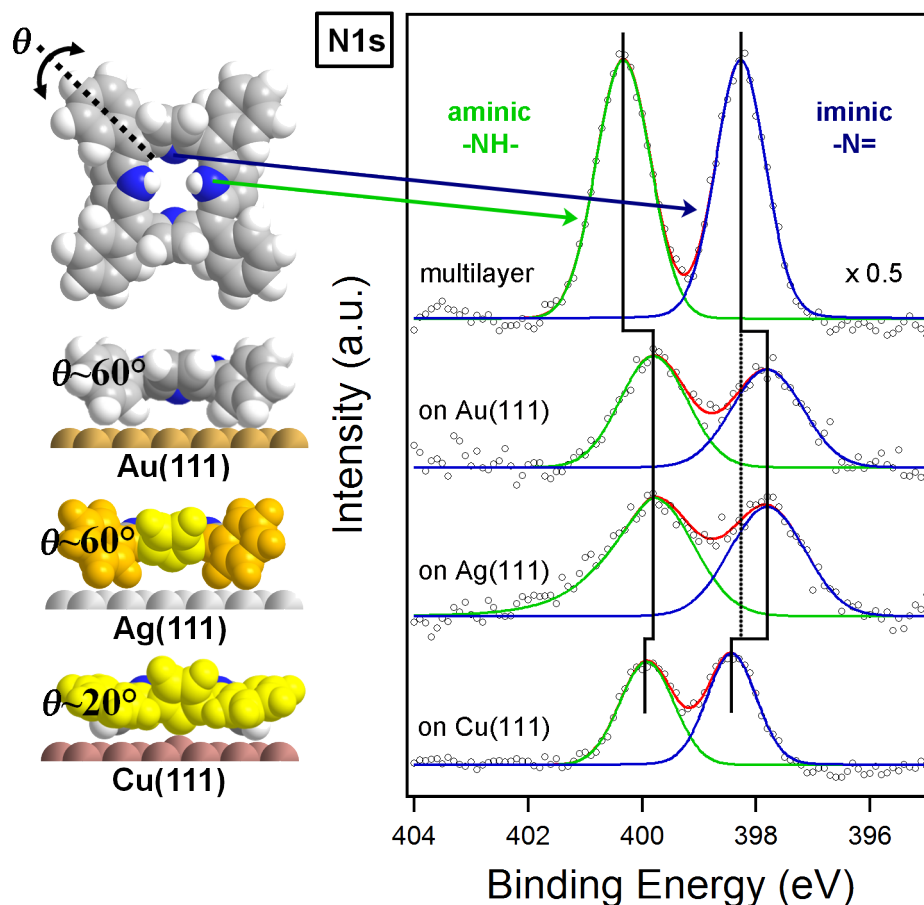


Figure 4.4: N 1s XPS spectra of 2HTPP multilayer, and 2HTPP layers (surface entirely covered with one layer) on Au(111), Ag(111) and Cu(111). The spectra are taken at RT with monochromatized Al-K α radiation at an electron collection angle of 70° relative to the surface normal.

On Au(111) and Ag(111) the fwhm is about 1.5 eV and on Cu(111) 1.0 eV. This result is also an indication for a highly site-specific adsorption behavior of 2HTPP on Cu(111). A strong molecule-substrate interaction ensures that the molecules bind to identical adsorption sites and therefore a smaller fwhm is achieved. In contrast, the larger fwhm on gold and silver results from the fact that the molecules are located at a variety of different adsorption sites, because the molecules form an ordered and incommensurate structure in which the location of an individual molecule is determined by the intermolecular interactions and not by the interactions with the substrate. [22, 23]

To further elucidate the role of the specific contributions of molecule-molecule and molecule-substrate interactions, the 2HTPP coverage on Cu(111) is increased. In Fig. 4.5 (a) a STM image with a molecular density of $\rho = 0.239 \text{ mol/nm}^2$ is shown and the molecular density in Fig. 4.5 (b) amounts to $\rho = 0.324 \text{ mol/nm}^2$. In both images the appearance of each molecule as two parallel rods and the three azimuthal orientations of the molecular axis is the same. Furthermore, the molecules still adsorb as individual molecules and no formation of a supramolecular ordered structure is found, although the free surface area is reduced. The absence of attractive T-type interactions and thus no formation of ordered structures can be explained by the specific intramolecular conformation of 2HTPP. The small twist angle of the phenyl rings does not allow the stabilization by T-type interactions between the phenyl rings of adjacent porphyrins. With increasing coverage, the path lengths of the one-dimensional diffusion of the molecules is reduced (see average frame in Fig. 4.5 d) and at even higher coverage the molecules are observed as roundish features instead of two elongated parallel rods (see average frame in Fig. 4.5 e). The latter is due to an affecting of the molecules, which induces rotation i.e. they change the diffusion direction from one densely packed Cu substrate row to another. Note that for low 2HTPP coverages rotation is only observed at higher temperatures, which is discussed in detail in Chapter 4.2.1.

If the 2HTPP coverage is further increased and exceeds a value of about $\rho \sim 0.36 \text{ mol/nm}^2$ a well-ordered checkerboard structure is observed (depicted in Fig. 4.5 (c) for a molecular density of $\rho = 0.435 \text{ mol/nm}^2$). Here, molecules with increased apparent height are visible in STM, which are denoted in the following as 2nd layer molecules. Each 2nd layer molecule appears in the STM image no longer with the typical rod like shape of the 1st layer molecules, but as four protrusions. Hence, a different intramolecular conformation of the 2nd layer molecules is assumed, i.e. larger twist angles of the phenyl rings. The four protrusions can be assigned to the four phenyl rings of one 2nd layer molecule. Indeed, Diller et al. reported a twist angle of $\theta = 55^\circ\text{-}60^\circ$ and an inclination angle for both iminic and aminic pyrrole rings of $\alpha = 40^\circ$ for multilayer 2HTPP molecules on Cu(111). [70] The superimposed scaled models with this intramolecular conformation agree very well with the STM image, as depicted in Fig. 4.5 (g).

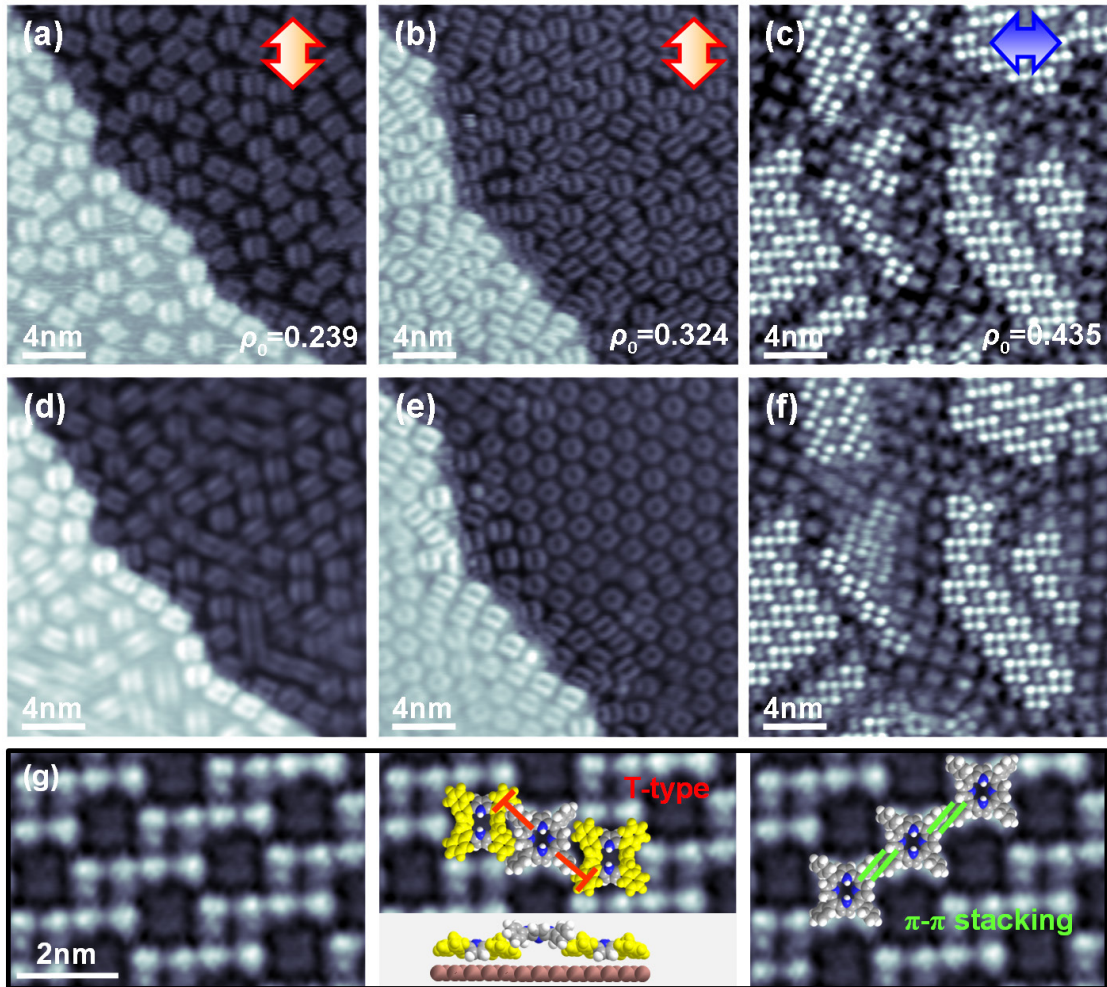


Figure 4.5: (a)-(c) Single STM images of 2HTPP on Cu(111) recorded at RT with increasing molecular densities. Below densities of $\rho \sim 0.36 \text{ mol/nm}^2$, a disordered adsorption behavior is observed and above densities of $\rho \sim 0.36 \text{ mol/nm}^2$ a well-ordered checkerboard structure is found. (d)-(f) Corresponding average images, highlighting the dynamic behavior (see text for details). (g) High resolution STM image of the checkerboard structure. Scaled space filling models are superimposed visualizing the stabilization of the checkerboard structure by T-type interactions between 1st (yellow) and 2nd layer (grey) molecules and π - π stacking between 2nd layer molecules. Tunneling parameters: (a), (d) $U_{\text{bias}} = -0.79 \text{ V}$, $I_{\text{set}} = 37.0 \text{ pA}$ (b), (e) $U_{\text{bias}} = -1.00 \text{ V}$, $I_{\text{set}} = 29.3 \text{ pA}$ (c), (f) $U_{\text{bias}} = -1.05 \text{ V}$, $I_{\text{set}} = 29.8 \text{ pA}$ and (g) $U_{\text{bias}} = -0.52 \text{ V}$, $I_{\text{set}} = 46.0 \text{ pA}$. Average images: (d) 61 STM images with an image-to-image time of 23 s, (e) 52 STM images with an image-to-image time of 26 s and (f) 60 STM images with an image-to-image time of 23 s.

The different intramolecular conformation of the 2nd layer molecules appears reasonable since the interaction with the substrate is weaker, compared to the strong interaction of the 1st layer molecules with the substrate. The analysis of the molecular structure revealed that the molecules in the 2nd layer are arranged together with the 1st layer molecules in a checkerboard structure, i.e. one 2nd layer molecule is bridging four 1st layer molecules (see side view model in Fig. 4.5 g). [106] By superimposing the corresponding scaled molecular models on an STM image, it becomes apparent that the checkerboard structure is stabilized by two different attractive molecule-molecule interactions. On the one hand “horizontal” π - π stacking between the phenyl rings of 2nd layer molecules and on the other hand “vertical” T-type interactions between the phenyl rings of 1st and 2nd layer molecules stabilize the ordered arrangement (see Fig. 4.5 g). Such a change of the ordering with increasing coverage was recently observed by Bischoff et al. for 2H-porphyrin on Ag(111) [107]: For submonolayer coverages the molecules adsorb randomly distributed on the surface due to the domination of molecule-substrate interactions and for higher coverages the molecules in the second layer form dense-packed islands due to the domination of molecule-molecule interactions. Summarizing the STM observations upon increasing the molecular density of 2HTPP on Cu(111), for low and medium molecular densities (between $\rho = 0.05 \text{ mol/nm}^2$ and $\rho = 0.36 \text{ mol/nm}^2$) the adsorption behavior is dominated by site-specific molecule-substrate interactions and for high molecular densities (above $\rho = 0.36 \text{ mol/nm}^2$) the adsorption behavior is dominated by molecule-molecule interactions, due to the formation of the well-ordered checkerboard structure.

4.1.2 Phase separation of two porphyrin derivatives [P1]

To further elucidate the influence of the iminic nitrogen atoms, mixtures of MTPP/2HTPP (with $M = \text{Co, Cu}$) are adsorbed on Cu(111) at RT. In MTPP all nitrogen atoms are coordinated to the corresponding metal center and therefore a weakening of the molecule-substrate interaction as compared to 2HTPP is expected.

The STM images in Fig. 4.6 (a) and (b) show the formation of ordered domains with a square or rhomboidal unit cell, which are assigned to CoTPP or CuTPP molecules, respectively. Note every protrusion in the domain corresponds to a MTPP

molecule. The 2HTPP molecules are observed in these images again as isolated molecules with the typical rod like shape.

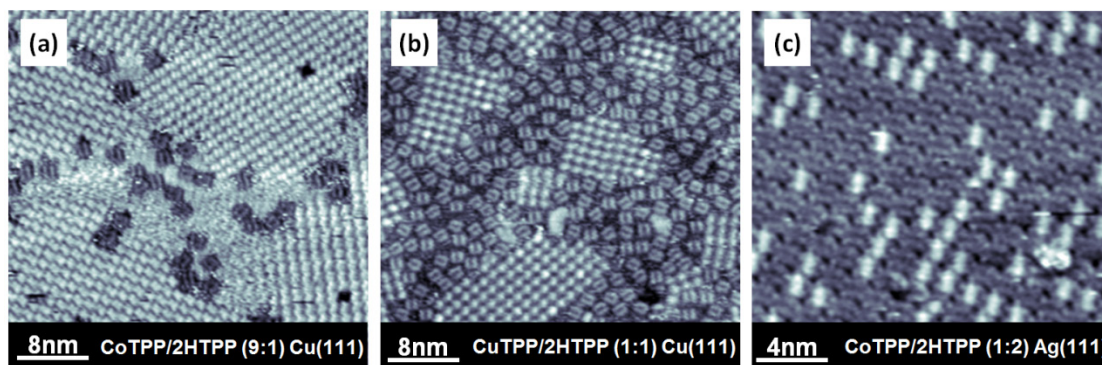


Figure 4.6: STM images obtained at RT on Cu(111) for mixtures of (a) CoTPP/2HTPP with a ratio of 9:1 and (b) CuTPP/2HTPP with a ratio of 1:1, demonstrating the effective phase separation of the two derivatives. (c) STM image of a intermixed layer for a mixture of CoTPP/2HTPP with a ratio of 1:2 on Ag(111) at RT. The tunneling parameters are: (a) $U_{\text{bias}} = +1.03 \text{ V}$, $I_{\text{set}} = 31.0 \text{ pA}$, (b) $U_{\text{bias}} = -1.22 \text{ V}$, $I_{\text{set}} = 24.3 \text{ pA}$ and (c) $U_{\text{bias}} = -1.35 \text{ V}$, $I_{\text{set}} = 35.0 \text{ pA}$.

Quite remarkably the analysis of large surface areas shows that not a single 2HTPP molecule is found inside the well-ordered MTPP domains. Even for the mixture CoTPP/2HTPP with a ratio of 9:1 the 2HTPP molecules are exclusively found between the ordered CoTPP domains, i.e. at the domain boundaries of the latter (see Fig. 4.6 a). This reveals that the two derivatives are effectively separated on Cu(111) at RT. In contrast, mixtures of CoTPP/2HTPP with a ratio of 1:2 form an intermixed layer on Ag(111) (see Fig. 4.6 c), stabilized by T-type interactions. [104], [P1]

High-resolution STM images of MTPP molecules are shown in Fig. 4.7, and highlight an anisotropic appearance of the individual MTPP molecules. CoTPP appears in STM with three aligned maxima along the molecular main axis (the outer two maxima appear brighter) surrounded by four dimmer protrusions (see Fig. 4.7 a). The latter correspond to the four phenyl groups (this assignment is confirmed by the molecular dimensions) and the central three protrusions are attributed on the one hand to the central metal ion and on the other hand to two opposite pyrrole rings, due to the distortion of the porphyrin macrocycle.

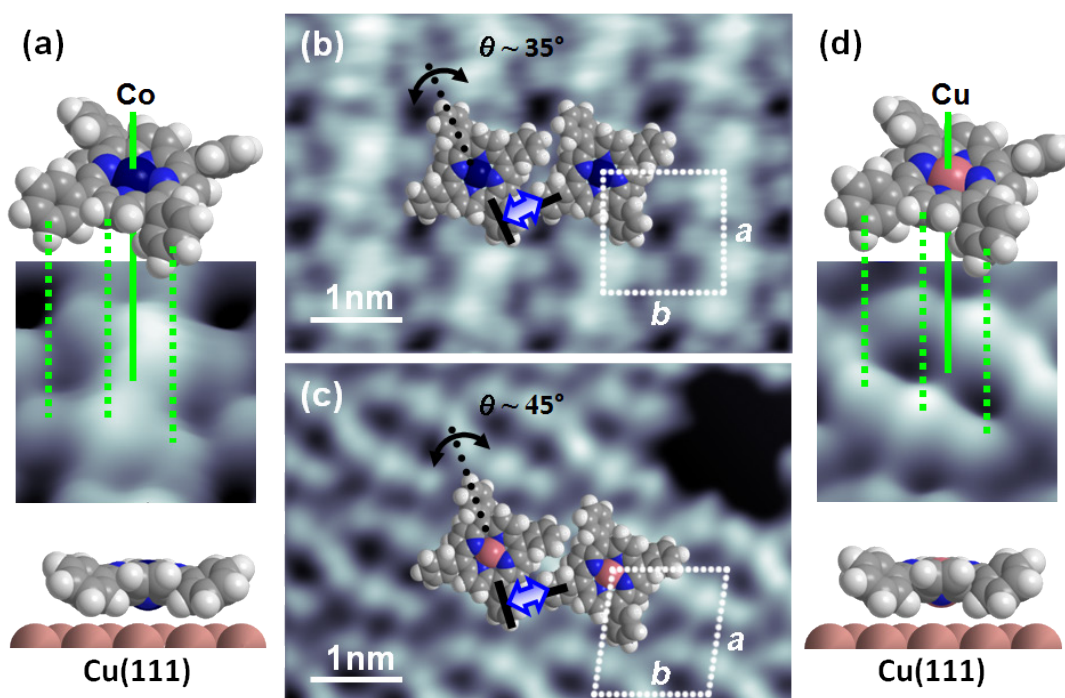


Figure 4.7: Pseudo-three-dimensional rendering of a high resolution STM image of (a) CoTPP and (d) CuTPP suggesting a saddle-shape macrocycle distortion and rotated phenyl rings for both molecules. The space filling models represent the intramolecular conformation as discussed in the text. STM image of (b) square ordered CoTPP ($a = b = 1.35 \pm 0.05$ nm, $\alpha = 90^\circ \pm 2^\circ$) and (c) rhomboidal ordered CuTPP ($a = 1.34 \pm 0.05$ nm, $b = 1.30 \pm 0.05$ nm, $\alpha = 85^\circ \pm 5^\circ$) with superimposed scaled models demonstrating the T-type motive. The tunneling parameters are: (a), (b) $U_{\text{bias}} = -1.48$ V, $I_{\text{set}} = 26.7$ pA and (c), (d) $U_{\text{bias}} = -1.45$ V, $I_{\text{set}} = 30.7$ pA.

In contrast CuTPP appears at a similar negative bias voltage with a central depression (see Fig. 4.7 c). The same characteristic appearance difference was observed by Brede et al. by comparing mixtures of CoTPP/CuTPP on Cu(111) at low temperatures and similar tunneling parameters to those applied here. [22] Thereby, the central protrusion of CoTPP originates from 3d states of the Co ion. [62, 93, 108] The intramolecular conformation of CoTPP and CuTPP on Cu(111) was derived in literature by combined NEXAFS and DFT studies. For CoTPP, a twist angle of the phenyl rings of $\theta = 35^\circ$ and an angle for the pyrrole rings of $\alpha = 20^\circ$ is reported. [93] Similar values are stated for CuTPP: the phenyl rings are twisted by $\theta = 40$ - 50° and the inclination angle of the pyrrole rings is about $\alpha = 10$ - 20° . [70] These

intramolecular conformations agree very well with the STM images, as shown in Fig. 4.7 by superposition of the corresponding scaled molecular models. Furthermore, inspection of the scaled models reveals that the molecules are arranged by a T-type motive. Thus, it is safe to say that MTPP domains are stabilized by attractive molecule-molecule interactions on Cu(111), as reported for MTPP on Ag(111).

The observed phase separation of free-base and MTPP molecules on Cu(111) requires sufficient mobility of both derivatives, as the deposition is realized by thermal evaporation of the corresponding porphyrin mixture and the molecules therefore statistically impinge on the surface. This means that the separation of the two derivatives is diffusion mediated. In Fig. 4.8 time sequences and average images of STM-Movies recorded at RT for a mixture of CoTPP/2HTPP with a ratio of 1:2 and for a mixture of CuTPP/2HTPP with a ratio of 1:1 are shown. The average images (Fig. 4.8 c and f) clearly show that 2HTPP carries out the aforementioned one-dimensional diffusion along one of the three densely packed Cu substrate rows. However, the time sequence of the ordered CoTPP (see Fig. 4.8 a, b) and CuTPP island (see Fig. 4.8 d, e) displays a changing shape of the islands contour, while the number of MTPP molecules in the domains roughly persist. These changes are highlighted by marking the contour of the island in the first image and superposition it in the subsequent recorded images. The gradual change of the islands contour reflects an adsorption-desorption equilibrium between detaching MTPP molecules from the solid phase and attaching molecules from the 2D gas phase. [109] By counting the molecules, exemplarily done for Fig. 4.8 (a), a CoTPP/2HTPP ratio of 1:2.2 is found, i.e. this is basically the composition of the raw powder mixture. This result indicates that only a minor portion of CoTPP is actually in the 2D gas phase. Beside the MTPP islands, no isolated MTPP molecules are observed in Fig. 4.8. However, in Fig. 4.8 (d) and (e) the background appears very bright. This is attributed to highly mobile CuTPP molecules, which permanently diffuse under the tip causing an increased apparent height in STM. The high mobility can be traced back to a weak molecule-substrate interaction and a weak surface corrugation, as in CuTPP all nitrogen atoms are equally coordinated to the metal center and there is no site-specific interaction to the substrate. In conclusion, the observed phase separation of the corresponding MTPP/2HTPP mixtures at RT is based on the different adsorption behaviors of the two derivatives.

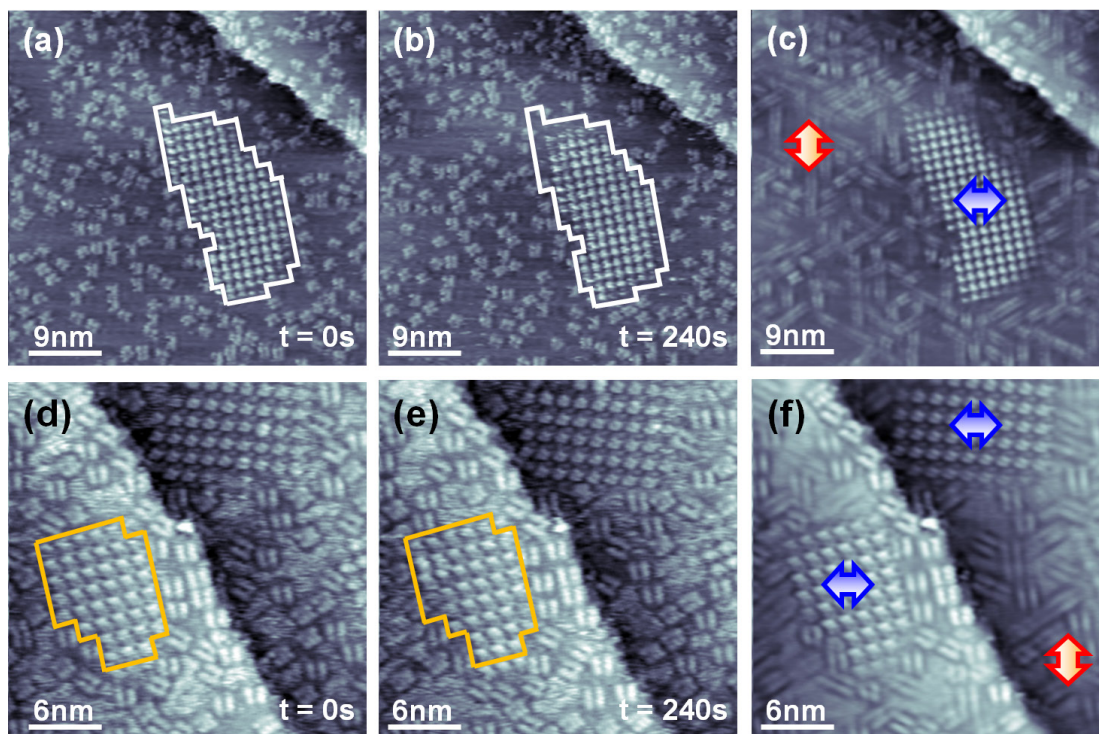


Figure 4.8: Time sequence STM images of (a), (b) CoTPP/2HTPP with a ratio of 1:2 and (d), (e) CuTPP/2HTPP with a ratio of 1:1 on Cu(111) with an increment of 240 s. (c) and (f) corresponding average images highlighting the dynamic behavior of MTPP and 2HTPP. Tunneling parameters: (a)-(c) $U_{\text{bias}} = -1.53 \text{ V}$, $I_{\text{set}} = 29.6 \text{ pA}$ and (d)-(f) $U_{\text{bias}} = -0.40 \text{ V}$, $I_{\text{set}} = 46.9 \text{ pA}$. Average images: (c) 26 STM images with an image-to-image time of 48 s and (f) 52 STM images with an image-to-image time of 27 s.

The adsorption of 2HTPP is dominated by the strong interaction of the iminic nitrogen atoms of 2HTPP with the Cu substrate atoms. As a result of this interaction, the molecule is pulled towards the surface; thus it exhibits a flat conformation, which does not allow for T-type interactions neither between 2HTPP molecules nor between MTPP and 2HTPP. Furthermore, the molecules are rather immobile at RT. In contrast, in MTPP all four nitrogen atoms are equally coordinated to the metal ion, resulting in a reduced interaction with the surface and a high mobility at RT. Furthermore, the weaker interactions with the substrate allow for larger twist angles of the phenyl rings of MTPP and thus stabilization by attractive T-type interactions is possible, leading to the formation of well-ordered domains. Thus, the two derivatives are effectively separated on Cu(111) at RT.

4.2 Temperature dependent behavior of 2HTPP on Cu(111)

In this chapter, the static and dynamic behavior of 2HTPP layers on Cu(111) is studied in dependence on the temperature. At temperatures in the range of 280-330 K one-dimensional diffusion and molecular rotation of 2HTPP is observed [P2]. Around 400 K, the self-metalation reaction of 2HTPP with Cu substrate atoms forming CuTPP occurs. Thereby, the self-metalation reaction for low coverages is studied under isothermal conditions at different temperatures, which allows the determination of the fundamental kinetic parameters [P4] and their dependence on the initial coverage [P3]. Upon annealing of 2HTPP layers to temperatures above 450 K, irreversible structural transformations of the in-situ metalated CuTPP are observed [P5].

4.2.1 Surface diffusion and molecular rotation [P2]

The surface diffusion and molecular rotation of individual 2HTPP molecules on Cu(111) around RT is studied in detail by STM-Movies recorded under isothermal conditions. For these measurements the 2HTPP coverage is selected intentionally very low ($\rho \sim 0.05$ mol/nm²) so that a significant contribution of intermolecular interactions can be ruled out, and the tunneling parameters are chosen to be $U \sim -1.5$ V, $I \sim 30$ pA to avoid tip-induced effects.

Figure 4.9 shows the average images for the STM-Movies at six different temperatures. The positions of the molecules are color-coded in each single STM image and then superimposed over the corresponding average images. This allows analyzing the diffusion behavior in dependence of the temperature qualitatively by comparing the resulting diffusion traces. At 280 K (see Fig. 4.9 a), the 2HTPP molecules are basically confined to their adsorption sites, i.e. they do not move during the acquisition of the STM-Movie, as evidenced by the circular dots. Upon increasing the temperature to 300 K (see Fig. 4.9 b) solely one-dimensional paths of the movement are observed along one of the three densely packed substrate rows. At 310 K (see Fig. 4.9 c) and at 315 K (see Fig. 4.9 d) the path lengths of the movement increases further and occasionally some molecules change their diffusion direction by $\pm 120^\circ$ from one densely packed Cu substrate direction to another (i.e. they rotate).

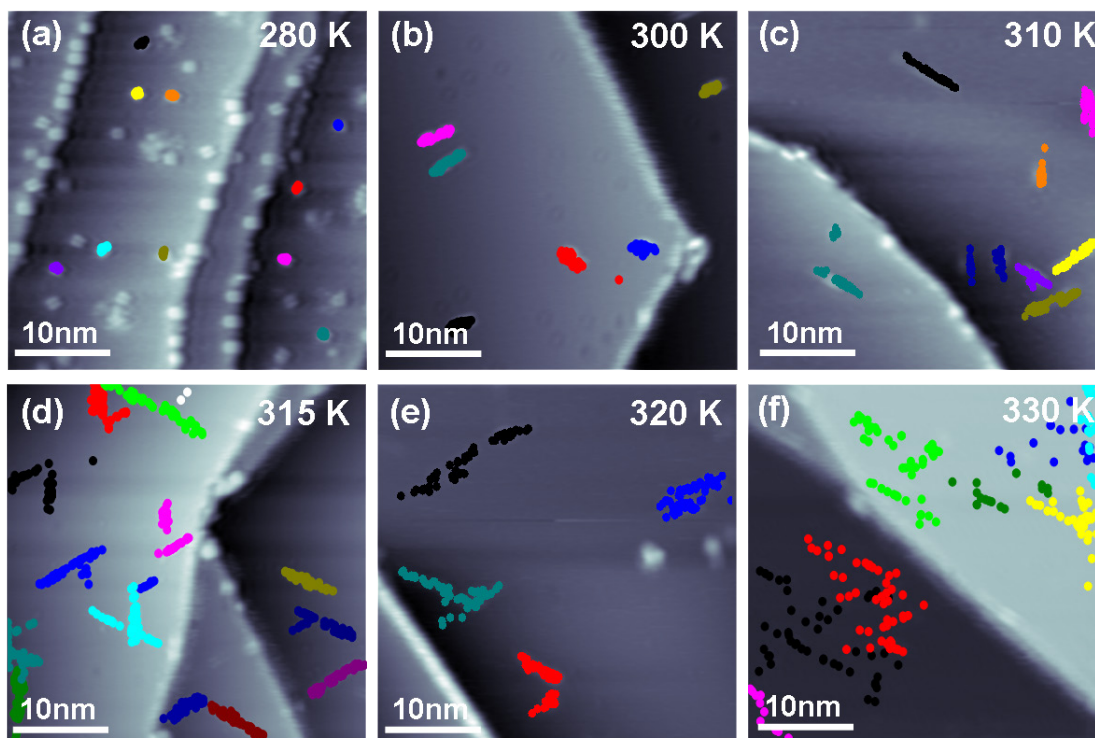


Figure 4.9: (a)-(f) Average images of STM-Movies of 2HTPP on Cu(111) between 280 and 330 K. The positions of the molecules are color-coded in each single STM image and then superimposed over the corresponding average images. Tunneling parameters are: (a) $U_{\text{bias}} = -1.51 \text{ V}$, $I_{\text{set}} = 29.0 \text{ pA}$ (b), (d)-(f) $U_{\text{bias}} = -1.49 \text{ V}$, $I_{\text{set}} = 30.0 \text{ pA}$ and (c) $U_{\text{bias}} = -1.54 \text{ V}$, $I_{\text{set}} = 29.0 \text{ pA}$. Average images: (a) 26 STM images with an image-to-image time of 30 s, (b) 72 STM images with an image-to-image time of 24 s, (c) 50 STM images with an image-to-image time of 24 s, (d) 50 STM images with an image-to-image time of 32 s, (e) 51 STM images with an image-to-image time of 34 s and (f) 48 STM images with an image-to-image time of 32 s.

At even higher temperatures, this trend intensifies and the path lengths (320 K in Fig. 4.9 e) and the number of rotations (330 K in Fig. 4.9 f) increase further. At 345 K, the movement and the rotational speed of the molecules are too fast on the STM time scale, and thus tracking of the molecules is difficult. This analysis points out that the 2HTPP molecules are able to overcome the energy barrier of migration E_{m} at temperatures around 300 K and the energy barrier for rotation E_{r} at temperatures around 310 K. Note that for a sufficient high coverage of 2HTPP the molecules can overcome the energy barrier for rotation even at RT (see Fig. 4.5 e).

Following the procedure described in Chapter 3.3, also a quantitative analysis of the STM-Movies is performed, resulting in the evaluation of the hopping rate $h(T)$ (after equation 3.4) and the rotation rate $r(T)$ (after equation 3.9) for each investigated temperature. Using the Arrhenius equation for surface diffusion (equation 3.7) and for molecular rotation (equation 3.10), the determination of the corresponding activation energies and pre-exponential factors is possible (see Fig. 4.10), which results in $E_m = 0.71 \pm 0.08$ eV and $A_m = 10^{10.9 \pm 1.4} \text{ s}^{-1}$ for the surface diffusion and $E_r = 1.28 \pm 0.12$ eV and $A_r = 10^{17.0 \pm 1.8} \text{ s}^{-1}$ for molecular rotation of 2HTPP on Cu(111). The much higher energy barrier for rotation than for migration is attributed to the very pronounced site-specific interactions between the iminic nitrogen atoms and the Cu substrate atoms in combination with a complex change of the intramolecular conformation during the rotation event. Furthermore, the pre-exponential factor for rotation is very high, whereas the corresponding pre-exponential factor for diffusion is in the range of molecular vibrations. Such a high pre-exponential factor could be explained by transition state theory where the pre-exponential factor reflects not directly a molecular vibration but rather an entropy gain of the transition state. Therefore, additional degrees of freedom (e.g. frustrated azimuthal rotation) could account for the gain. In literature, similar or even higher pre-exponential factors are reported for desorption of large organic molecules (see table 9.1). [27, 36, 37, 110-113]

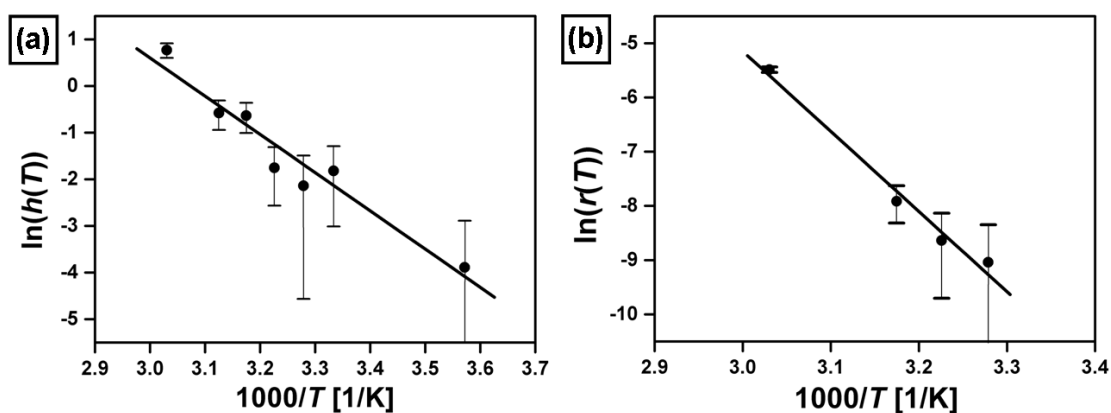


Figure 4.10: Arrhenius plot of (a) the hopping rate $h(T)$ and (b) the rotation rate $r(T)$ against the corresponding inverse temperature ($1/T$) for 2HTPP on Cu(111).

4.2.2 Self-metalation reaction [P3, P4, P5]

Monitoring the self-metalation reaction with STM [part of P5]

As mentioned in the literature review (see Ch. 1.3.3) Diller et al. reported the self-metalation reaction of 2HTPP on Cu(111) to occur at 420 K by combining NEXAFS and XPS measurements with DFT calculations. [70] Here, it is demonstrated that the progress of the self-metalation can be followed by STM measurements. Therefore, the sample is annealed to 400 K for the indicated times and afterwards cooled down to RT. Figure 4.11 (a) shows a 2HTPP layer as prepared at RT, with a molecular density of $\rho_0 = 0.30 \text{ mol/nm}^2$. Here, the typical adsorption behavior and appearance of 2HTPP in STM is observed. STM images acquired at RT after annealing to 400 K for 2 min and for 120 min show the formation of square ordered islands and additional in Fig. 4.11 (c) the background appears very bright and noisy.

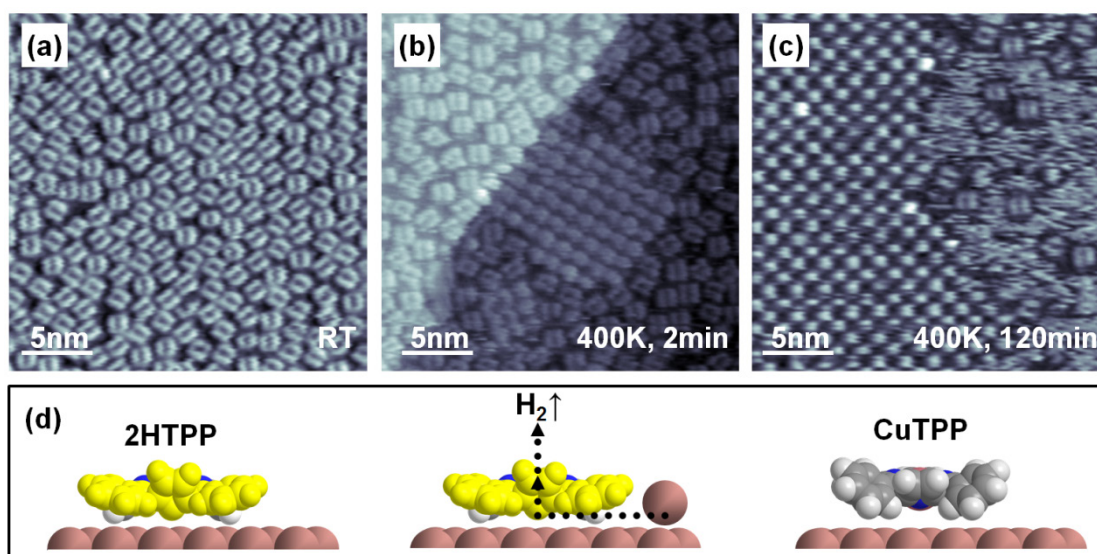


Figure 4.11: Room temperature STM images: (a) 2HTPP layer with a molecular density of $\rho_0 = 0.30 \text{ mol/nm}^2$ as prepared and after annealing to 400 K for (b) 2 min and (c) 120 min. (d) Illustration of one possible pathway of the self-metalation reaction. The tunneling parameters are: (a) $U_{\text{bias}} = -1.00 \text{ V}$, $I_{\text{set}} = 38.6 \text{ pA}$ (b) $U_{\text{bias}} = -1.02 \text{ V}$, $I_{\text{set}} = 39.2 \text{ pA}$ and (c) $U_{\text{bias}} = -1.00 \text{ V}$, $I_{\text{set}} = 29.2 \text{ pA}$.

Furthermore, the density of the 2HTPP molecules is decreasing with increasing annealing time, as becomes obvious from Fig. 4.11. Moreover, a phase separation

between the 2HTPP molecules and the formed islands occurs. These findings can be interpreted with the formation of CuTPP molecules, i.e. 2HTPP molecules can pick up Cu atoms from the Cu(111) substrate and oxidize them at elevated temperatures (see illustration in Fig. 4.11 d). Furthermore, they are in accordance with STM results observed for a CuTPP/2HTPP mixture on Cu(111) at RT (see Ch. 4.1.2). Additional XPS measurements in the N 1s and C 1s region with the same annealing/cooling procedure are performed by our cooperation partners J. Xiao, M. Chen and M. Gottfried from the Chair of Physical Chemistry II at the Friedrich-Alexander-Universität Erlangen-Nürnberg. [P5] The observed changes in the XP spectra are attributed to the formation of CuTPP and are consistent to the STM data.

Determination of activation energy for self-metalation reaction [P4]

The possibility to follow the self-metalation reaction with STM enables the determination of the fundamental kinetic parameters, such as activation energy and pre-exponential factor by following the procedure described in Chapter 3.3. The self-metalation reaction is investigated under isothermal conditions at temperatures between 390 and 410 K for submonolayer coverages of 2HTPP (between $\rho_0 = 0.135$ and 0.174 mol/nm²). The progress of the self-metalation reaction is shown in Fig. 4.12 for 390 and 410 K. From these two image series of the self-metalation reaction it is evident that individual 2HTPP molecules can be clearly distinguished and thus it is possible to determine the molecular density ρ_t as a function of annealing time t . Note that for these low starting coverages the reaction product CuTPP is observed in STM as noisy streaks or bright areas, due to the high mobility of CuTPP on Cu(111) at RT and thus cannot be quantified. The comparison of the two series reveals that the self-metalation reaction occurs faster at higher temperatures, as expected. In Fig. 4.13 (a) the decrease of the normalized densities (ρ_t/ρ_0) of 2HTPP with increasing annealing time is depicted for the four investigated temperatures. For each temperature an exponential decrease is found.

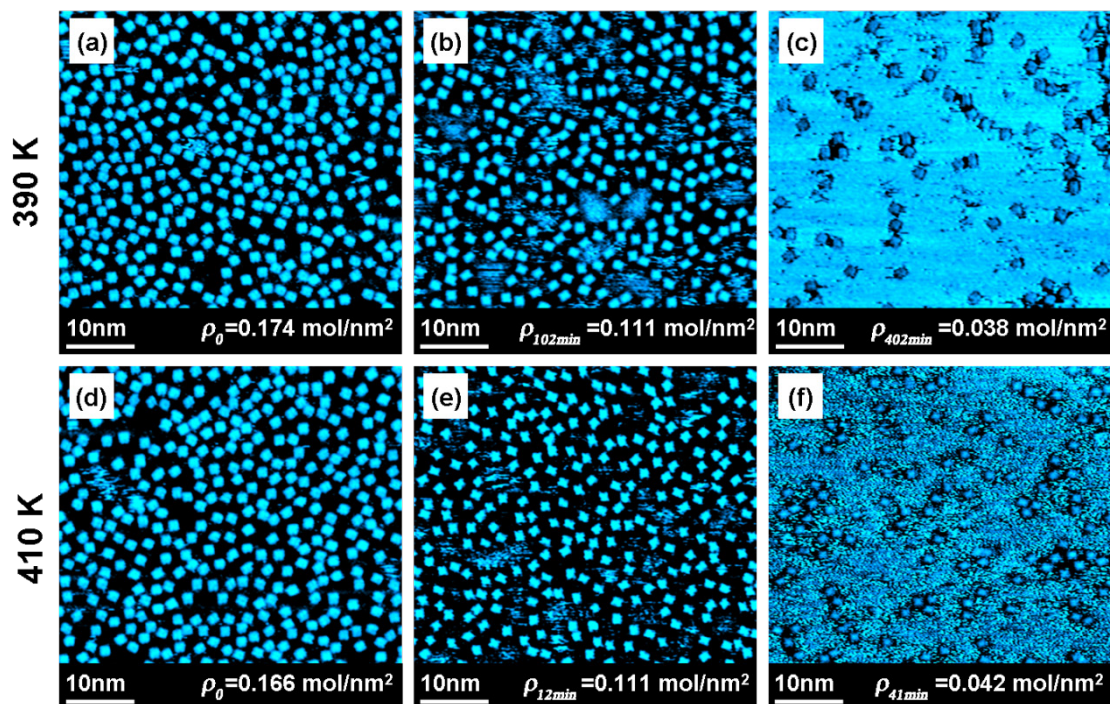


Figure 4.12: (a) and (d) STM images of 2HTPP on Cu(111) as prepared at RT. The STM images (b), (c) and (e), (f) demonstrate the progress of the self-metalation reaction after annealing to 390 K or 410 K for the indicated times. The tunneling parameters are: (a) $U_{\text{bias}} = -1.00$ V, $I_{\text{set}} = 20.7$ pA (b) $U_{\text{bias}} = -1.00$ V, $I_{\text{set}} = 29.1$ pA (c) $U_{\text{bias}} = -1.00$ V, $I_{\text{set}} = 30.3$ pA (d), (e) $U_{\text{bias}} = -1.00$ V, $I_{\text{set}} = 29.9$ pA and (f) $U_{\text{bias}} = -1.02$ V, $I_{\text{set}} = 40.9$ pA.

Plotting $\ln(\rho_t/\rho_0)$ versus time yields a linear behavior for all four temperatures, which confirms the assumption of a pseudo-first order reaction made in Chapter 3.3. The metalation rates k_T for the different temperatures are derived from the slopes of the linear regressions in Fig.4.13 (b). Using the Arrhenius equation for the self-metalation reaction (equation 3.13) allows to determine the activation energy and pre-exponential factor, yielding $E_s = 1.48 \pm 0.12$ eV and $A_s = 10^{15 \pm 1.6} \text{ s}^{-1}$. DFT calculations of the activation energy for the metalation of 2H-porphyrin (i.e. without phenyl rings at the meso-position) with Cu in the gas phase resulted in values ranging from 1.03 to 1.60 eV, depending on the level of theory and applied basis sets (see table 9.1). [72] Thus, the determined experimental values are in very good agreement with the DFT calculations.

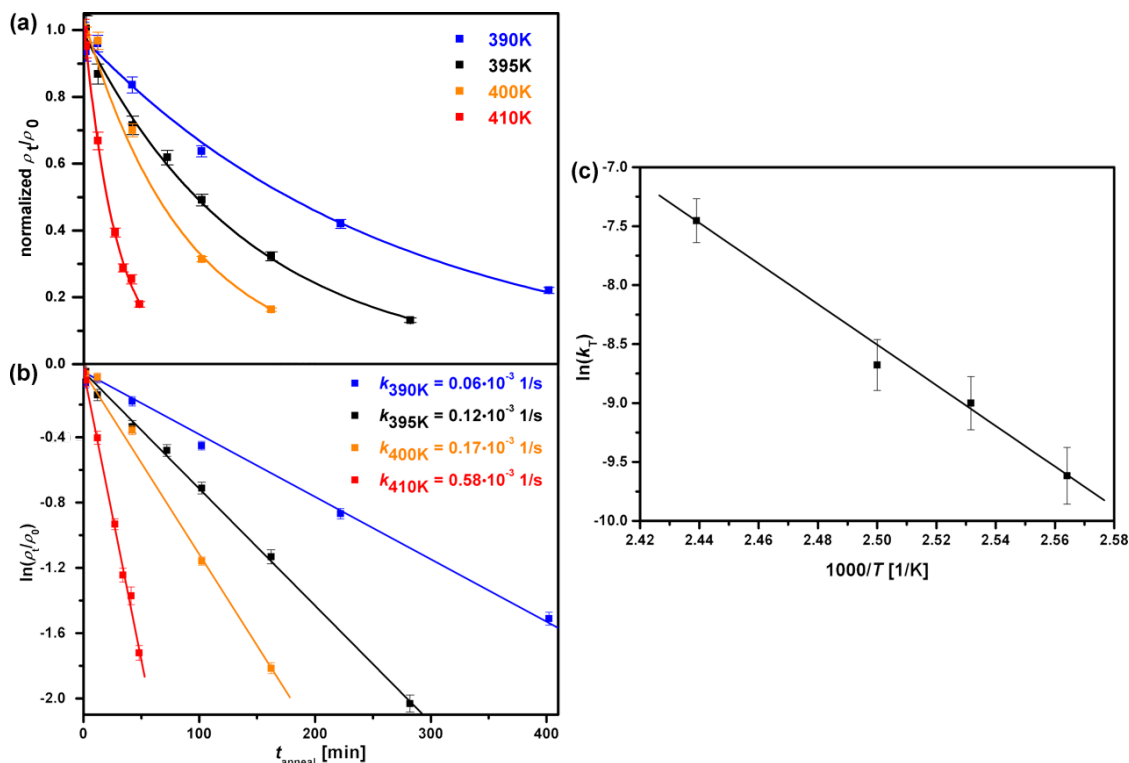


Figure 4.13: (a) Plot of the normalized molecular density (ρ/ρ_0) of 2HTPP on Cu(111) versus the annealing time t at the indicated constant temperatures. (b) Logarithmic plot of the data in (a). (c) Arrhenius plot of the metalation rates k_T , derived from the corresponding line slopes in (b).

Coverage induced enhancement of self-metalation reaction [P3]

While the fundamental kinetic parameters are determined for 2HTPP submonolayers, this paragraph deals with the coverage dependence of the self-metalation reaction. Therefore, 2HTPP layers with different coverages are prepared and afterwards the self-metalation reaction is induced by annealing the sample to 400 K for 10 min and subsequently cooling down to RT. Before and after the self-metalation has occurred the molecular density of 2HTPP is determined both by STM- and XPS-measurements. In Fig. 4.14 the STM images before and after annealing to 400 K for different initial 2HTPP coverages (between $\rho_0 = 0.231$ and $\rho_0 = 0.573$ mol/nm²) are presented. The corresponding XPS measurements, performed by our cooperation partners M. Röckert, J. Xiao and O. Lytken from the Chair of Physical Chemistry II at the Friedrich-Alexander-Universität Erlangen-Nürnberg can be found in [P3].

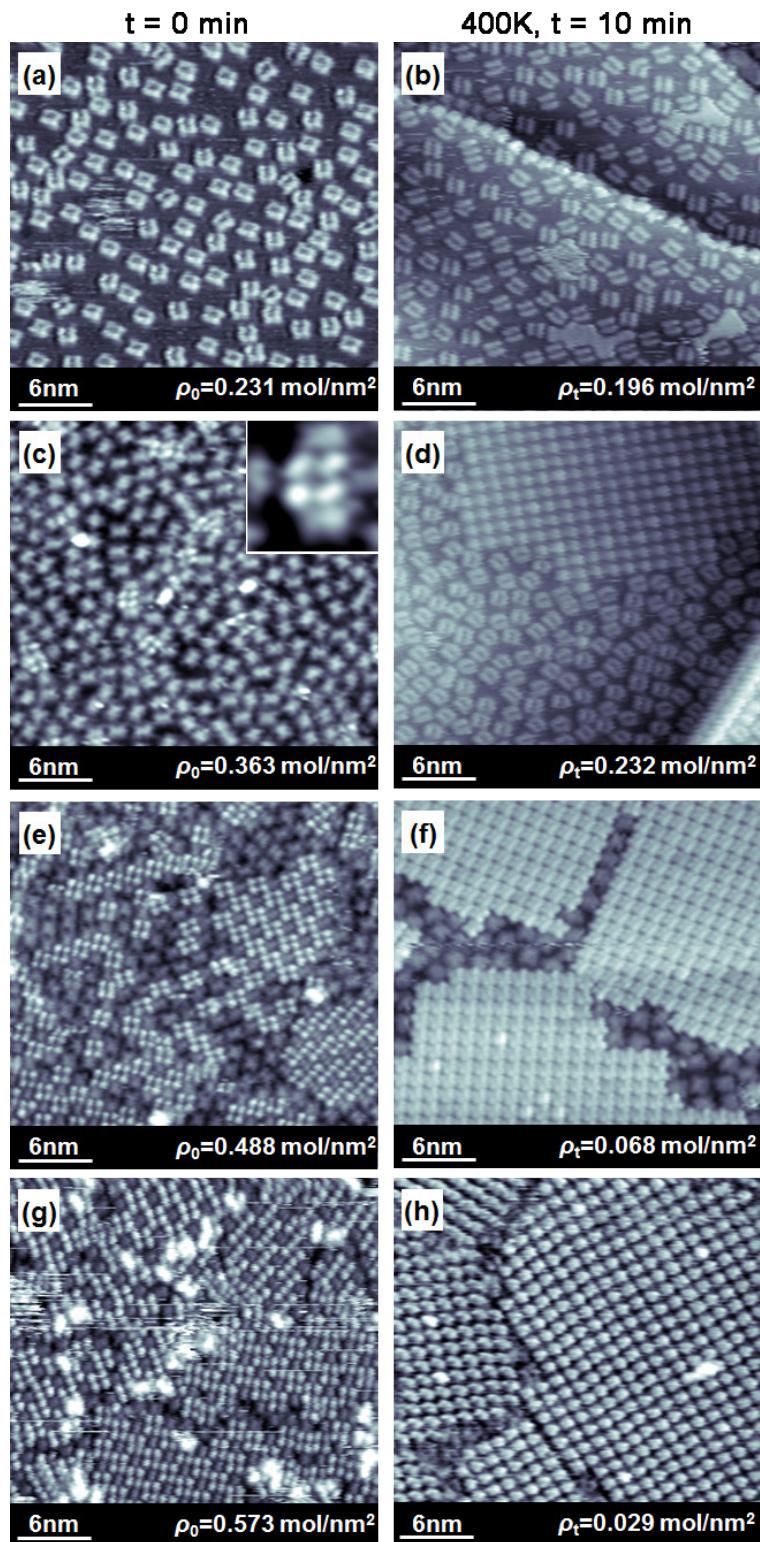


Figure 4.14: STM images of 2HTPP as prepared on Cu(111) (left side) and after the self-metalation reaction (right side) with variation of the initial coverage. For details see text. The tunneling parameters are: (a) $U_{\text{bias}} = -1.00 \text{ V}$, $I_{\text{set}} = 20.8 \text{ pA}$ (b)-(g) $U_{\text{bias}} = -1.00 \text{ V}$, $I_{\text{set}} = 30.0 \text{ pA}$ and (h) $U_{\text{bias}} = -1.56 \text{ V}$, $I_{\text{set}} = 29.4 \text{ pA}$.

The STM images for a submonolayer coverage ($\rho_0 = 0.321$ mol/nm) reveal that only a very few 2HTPP molecules are metalated to CuTPP (see Fig. 4.14 a, b) in comparison with the results shown above. The in-situ generated CuTPP molecules are again visible on the substrate terraces as bright areas and additional as single dots (medium resolution of CuTPP) on the previously featureless substrate steps. Energetically favorable adsorption sites and/or the Ehrlich-Schwoebel barrier are proposed to favor the observed step decoration. [114, 115] At a 2HTPP coverage of $\rho_0 = 0.363$ mol/nm² a few isolated molecules are observed in the 2nd layer upon deposition on Cu(111) (see Fig. 4.15 c). After metalation large CuTPP islands are found (see Fig. 4.14 d). Prepared 2HTPP layers of $\rho_0 = 0.488$ mol/nm² show the well-ordered checkerboard structure (see Fig. 4.14 e), and for layers with coverages of $\rho_0 = 0.573$ mol/nm² even molecules in a higher layer are found (see Fig. 4.14 g). After annealing of these two layers, the formation of CuTPP islands is observed, covering almost the entire surface (see Fig. 4.14 f, h). These findings indicate that the metalation rate dramatically increases with increasing initial 2HTPP coverage.

The corresponding XPS measurements are consistent to the STM data, which is shown in Fig. 4.15 by plotting the density ratios (ρ_t/ρ_0) as a function of the initial density ρ_0 . For a better understanding, the coverage range of the randomly distributed 2HTPP layer is shaded in white, the ordered checkerboard structure in orange, and the multilayer regime in blue. For low initial coverages a metalation degree of 10-20 % is achieved and for the checkerboard structure an increasing metalation degree up to 95 % is found. From this data, it is obvious that the increase of the metalation rate coincides with the formation of the checkerboard structure. Different mechanisms, which could be responsible for the dramatic increase of the metalation rate, seem possible. One explanation could be that copper adatoms can diffuse more simply beneath the 2nd layer 2HTPP molecules of the checkerboard structure and thus an easier access to the porphyrin macrocycle is possible. Furthermore, a weakening of the strong coordinative bond between the iminic nitrogen atoms and the copper substrate atoms of 1st layer 2HTPP molecules in the checkerboard structure is conceivable. The weakening could be the result of the “vertical” T-type interactions between the molecules in the 1st and 2nd layer and as a consequence the metalation rate increases. Another explanation is based on an entropic argument. The entropy of 2HTPP

molecules in the disordered layer could be higher than for 2HTPP molecules in the checkerboard structure, due to a higher degree of freedom (i.e. one-dimensional diffusion, molecular rotation).

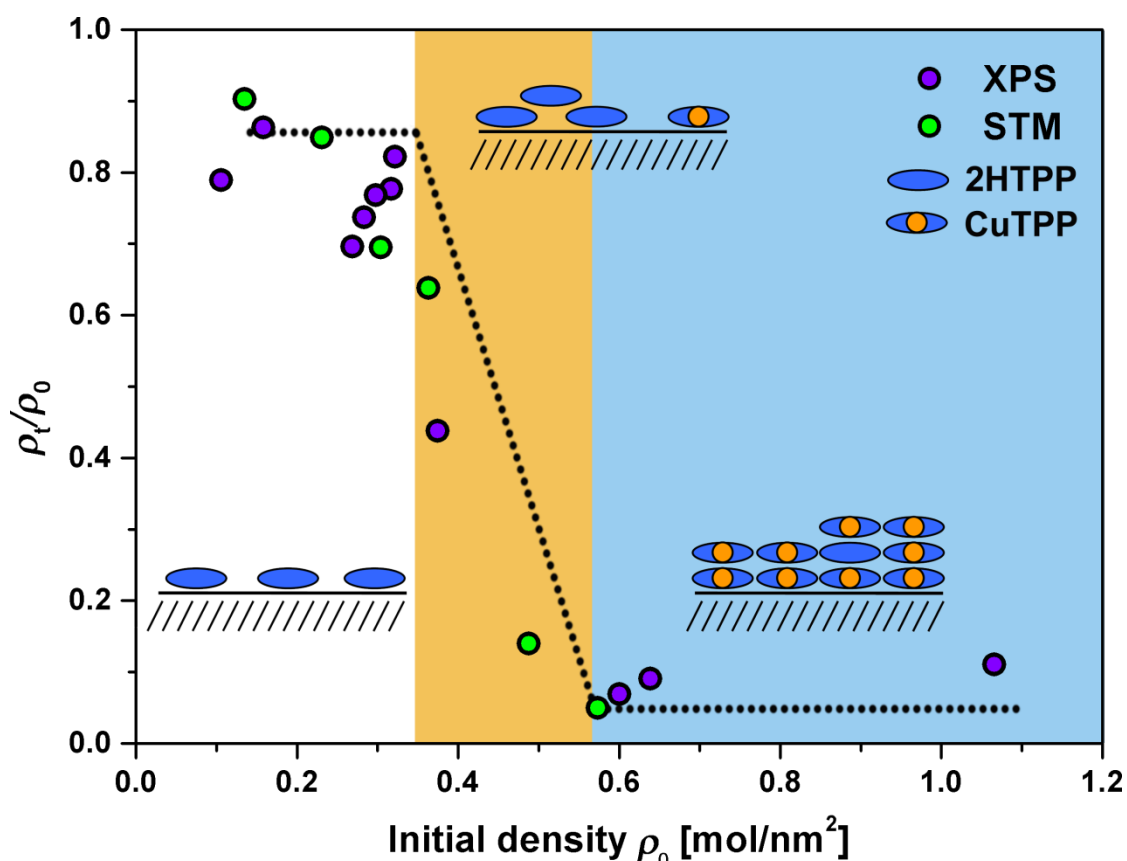


Figure 4.15: Plot of the ratio of the molecular density (ρ_f/ρ_0) obtained after annealing to 400 K for 10 min versus the initial coverage ρ_0 . For low initial coverages the metalation rate is small, but for high coverages (above $\rho_0 = 0.363 \text{ mol/nm}^2$) the metalation rate increases dramatically.

4.2.3 Chemical and structural transformations [P5]

In the previous analyses, 2HTPP layers were studied upon annealing up to temperatures of 410 K. For submonolayer 2HTPP coverages, the one-dimensional diffusion was analyzed at temperatures between 280 and 330 K, the molecular rotation between 305 and 330 K and the self-metalation reaction of 2HTPP with Cu substrate atoms to form CuTPP between 390 and 410 K. In the following, 2HTPP submonolayers ($\rho_0 = 0.25 \text{ mol/nm}^2$) are investigated by STM and XPS upon annealing

to higher temperatures. The prepared layers are first annealed to 450 K for 2 min and subsequently cooled down to RT. STM images acquired at RT after the thermal treatment show no individual molecules on the copper terraces, but streaky features and step decoration (not shown here; a corresponding STM image can be found in [P5]). This could be explained by a complete self-metalation reaction. All 2HTPP molecules are metalated to form the reaction product CuTPP, which cannot be imaged at RT due to its high mobility. To confirm this statement the sample is cooled down to 200 K, which suppresses the lateral movement of the molecules sufficiently and thus they are directly visible in the STM images.

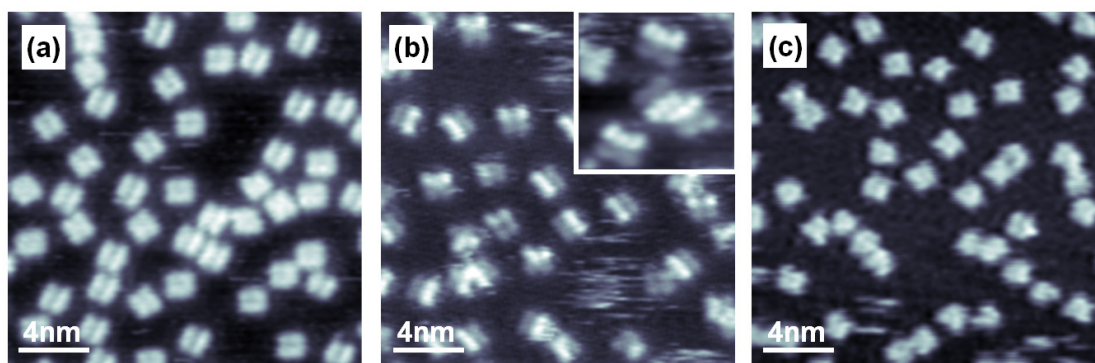


Figure 4.16: STM images of 2HTPP on Cu(111) after (a) deposition of $\rho_0 = 0.25 \text{ mol/nm}^2$ and after annealing for 2 min to (b) 450 K and (c) 500 K. Image (a) is recorded at RT, the images (b) and (c) at 200 K. The tunneling parameters are: (a) $U_{\text{bias}} = -0.87 \text{ V}$, $I_{\text{set}} = 17.0 \text{ pA}$ (b) $U_{\text{bias}} = -1.43 \text{ V}$, $I_{\text{set}} = 21.0 \text{ pA}$ and (c) $U_{\text{bias}} = -0.89 \text{ V}$, $I_{\text{set}} = 24.0 \text{ pA}$.

However, at low temperatures isolated molecules are observed, which appear with a brighter and a darker side in STM (see Fig. 4.16 b). This suggests that the molecules adopt a tilted orientation relative to the substrate surface. Interestingly, some molecules interact with each other through their brighter sides and form dimers, trimers and tetramers (see inset in Fig. 4.16 b). Note that STM images with submolecular resolution of CuTPP on Cu(111) indicate an adsorption geometry where the porphyrin plane is oriented parallel to the surface plane (see Fig. 4.7). In a second step, the layer is annealed to 500 K for 2 min and afterwards subsequently cooled down to RT. As the molecules are still too mobile to be imaged at RT, the sample is

again cooled down to 200 K. At this temperature the molecules appear as isolated molecules with four protrusions of the same brightness (see Fig. 4.16 c). This indicates, that the porphyrin plane is again oriented parallel to the substrate. The observed structures after annealing to 450 and 500 K show a different appearance than 2HTPP (see Fig. 4.2 for comparison) or CuTPP (see Fig. 4.7 for comparison), which indicates that “secondary” reactions after self-metalation have occurred, leading first to a tilted and then again to a flat configuration.

Additional XPS measurements in the N 1s and C 1s regime with the same annealing/cooling process are performed by our cooperation partners J. Xiao, M. Chen and M. Gottfried from the Chair of Physical Chemistry II at the Friedrich-Alexander-Universität Erlangen-Nürnberg. [P5] The observed changes in the XP spectra after annealing to 450 and 500 K indicate on the one hand a complete metalation to CuTPP and on the other hand a successive decrease of the molecule-substrate distance. [P5] By analyzing the apparent heights of 2HTPP, CuTPP (adsorbed at RT or after metalation at 400 K) and CuTPP after annealing to 450 and 500 K in STM images, a similar change of the molecule-substrate distance is observed (see Fig. 4.17). Note that for this comparison of the apparent heights different preparations are used (i.e. high initial coverages, or additional deposition of 2HTPP after the thermal treatment), where at least two different species are visible at the same time in the STM images. Furthermore, as the distance between the porphyrin plane and the substrate is mainly determined by the orientation of the peripheral phenyl rings (i.e. the twist angle), the height profiles are extracted at the periphery of the molecule.

CuTPP exhibits larger twist angles of the phenyl rings compared to 2HTPP and thus CuTPP appears with a significant larger apparent height, i.e. the molecule-substrate distance is increased. The brighter side of the tilted CuTPP molecules annealed to 450 K exhibits almost the same apparent height as the CuTPP molecules, whereas the darker side exhibits an apparent height similar to that of the CuTPP molecules annealed to 500 K. This means that, after annealing to 450 K, one side of the CuTPP molecule is brought closer to the surface, and after annealing to 500 K, the whole molecule appears with a reduced height, presumably realized by a lowering of the other side of the molecule.

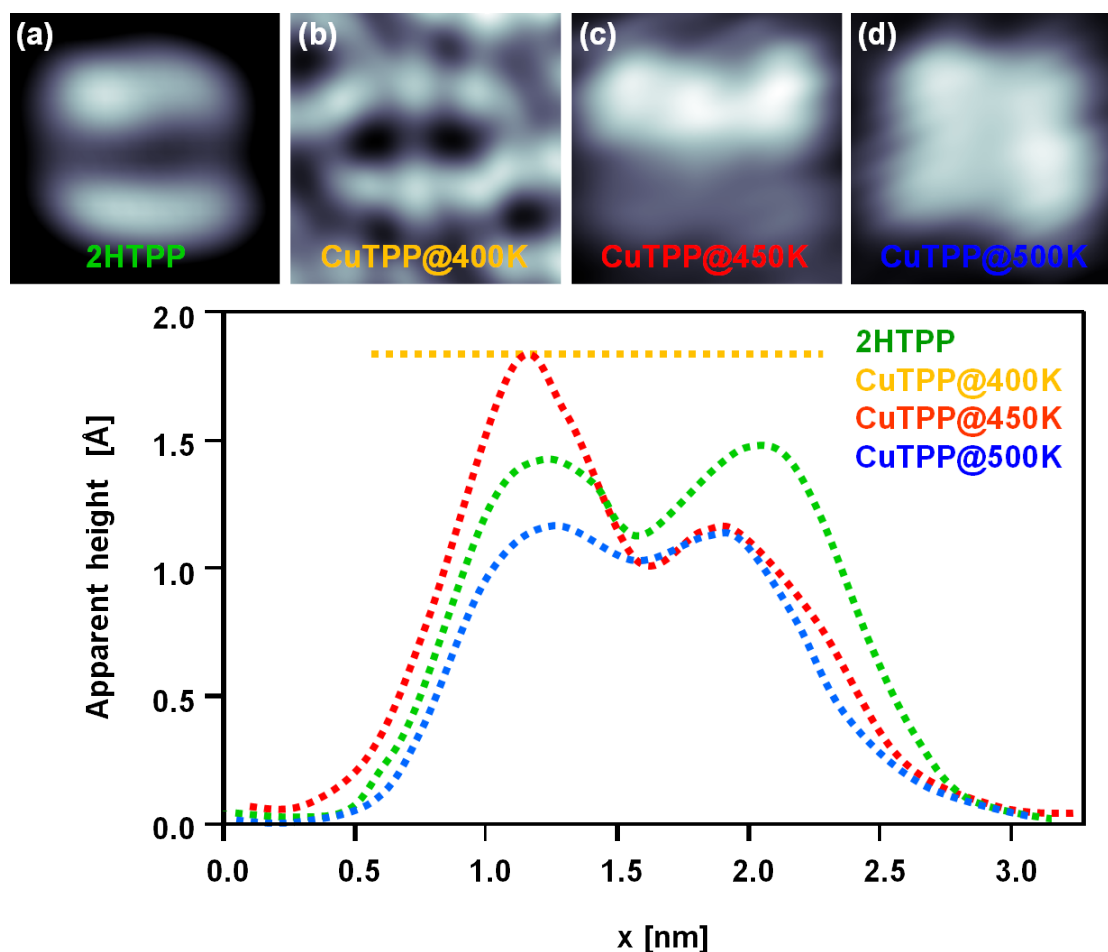


Figure 4.17: STM images of individual molecules after deposition and after sample annealing to 400 K, 450 K and 500 K and the corresponding extracted apparent height profiles. The tunneling parameters are: (a) $U_{\text{bias}} = -0.77 \text{ V}$, $I_{\text{set}} = 26.0 \text{ pA}$ (b) $U_{\text{bias}} = -0.87 \text{ V}$, $I_{\text{set}} = 17.0 \text{ pA}$ (c) $U_{\text{bias}} = -1.43 \text{ V}$, $I_{\text{set}} = 21.0 \text{ pA}$ and (d) $U_{\text{bias}} = -0.89 \text{ V}$, $I_{\text{set}} = 24.0 \text{ pA}$.

The observed effects can be interpreted as the result of a successive dehydrogenation reaction of β - and/or ortho-hydrogen atoms at the porphyrin macrocycle and the phenyl rings. First, at 450 K one side of the porphyrin molecule is dehydrogenated, which leads to a reduced steric hindrance of the two neighboring phenyl rings and thus smaller twist angles, i.e. the phenyl rings are nearly parallel to the substrate. As a result the distance to the substrate of the dehydrogenated side is reduced. The other two phenyl rings (bright side) still exhibit a larger twist angle. Consequently, T-type interactions can be established between the bright sides of neighboring molecules,

leading to the observed dimers, trimers and tetramers. After annealing to 500 K, dehydrogenation occurs on the other side and as a result the whole molecule is lowered towards the surface and all phenyl rings are almost parallel to the surface.

Dehydrogenation reactions were previously reported in literature by Haq et al. for diphenylporphyrin, 2H-porphyrin and Cu-porphyrin on Cu(110) in a combined STM and TPD study. [69] They found that annealing leads to a C-H bond scission at the outer porphyrin core under release of hydrogen. C-H bond breaking was observed for diphenylporphyrin at temperatures between 420 and 590 K and for 2H-porphyrin and Cu-porphyrin between 600 and 670 K.

4.3 Different aspects of 2HTTBPP on Cu(111) [P6]

In the following chapter, the adsorption behavior of 2HTTBPP on Cu(111) around RT is discussed in detail. 2HTTBPP is a more voluminous molecule than the previous studied 2HTPP, i.e. two di-tert-butyl groups are attached to the 3 and 5 positions of the phenyl rings. The investigation of these molecules is extremely interesting, as the corresponding metalated TTBPP molecules are well known for their conformational flexibility on metal surfaces, i.e. CoTTBPP on Ag(111) simultaneously forms three different supramolecular arrangements at RT [48]. Furthermore, the influence of the Cu(111) surface on the adsorption behavior is particularly interesting, since Cu(111) strongly interacts with 2HTPP, as shown before [P1, P2].

4.3.1 Adsorption behavior of 2HTTBPP on Cu(111)

The large-scale image in Fig. 4.18 (a) shows a submonolayer of 2HTTBPP on Cu(111) at RT. Interestingly, the molecules are arranged in domains of alternating bright and dark rows surrounded by noisy and bright areas. The latter can be attributed to highly mobile 2HTTBPP molecules, resulting in a 2D gas phase. Neglecting the different appearance of the rows, the molecules form a hexagonal arrangement with lattice constants of $a = 1.90 \pm 0.10$ nm, $b = 2.00 \pm 0.10$ nm and $\alpha = 60^\circ \pm 5^\circ$. The high resolution STM image in Fig. 4.18 (b) allows for conclusions on the intramolecular conformation. Two types of appearance can be clearly distinguished and assigned to the corresponding rows: the bright rows consist of molecules with a central protrusion and the dark rows of molecules with a central depression.

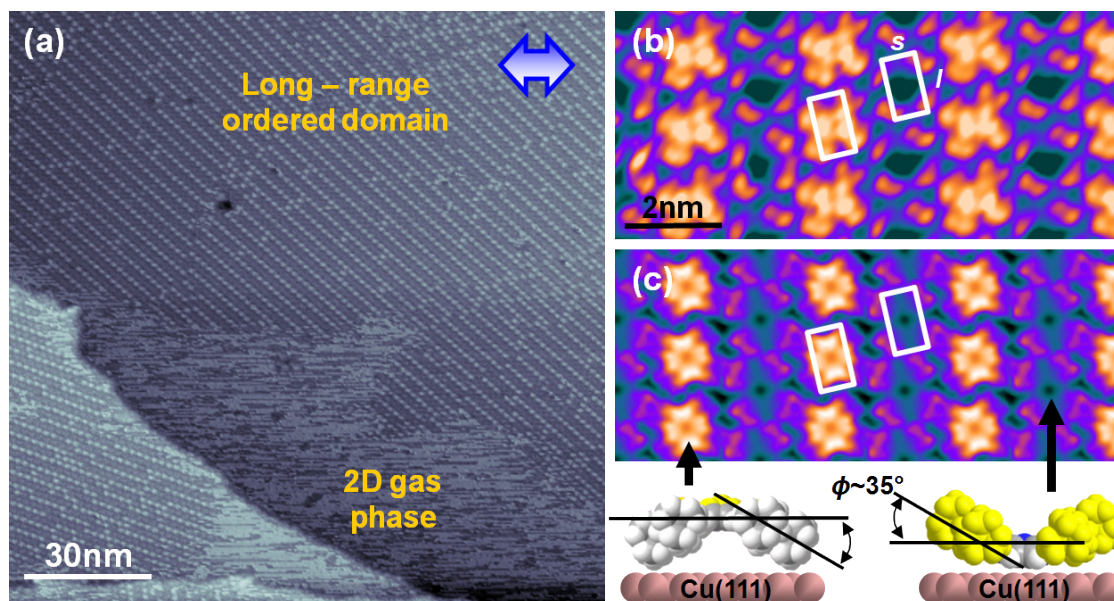


Figure 4.18: (a) Large-scale STM image of 2HTTBPP adsorbed on Cu(111) at RT. The molecules are arranged in domains of alternating bright and dark rows surrounded by a 2D gas phase. (b) High resolution STM image demonstrating the two different appearances of the molecules assigned to concave (central cavity) and convex (central protrusion) conformation. (c) Corresponding simulated STM image. The tunneling parameters are: (a) $U_{\text{bias}} = +1.51 \text{ V}$, $I_{\text{set}} = 28.9 \text{ pA}$ and (b) $U_{\text{bias}} = +1.76 \text{ V}$, $I_{\text{set}} = 25.0 \text{ pA}$.

The periphery of the molecules appears as eight bright spots, which can be attributed to the eight di-tert-butyl groups arranged in four groups around the molecular center corresponding to the four phenyl rings. As indicated in Fig. 4.18 (b) the four peripheral groups form a rectangle, which is basically identical for the two different molecular appearances. Generally, the aspect ratio, l/s , and the perimeter, $2(l+s)$, of the long and short sides of the rectangle formed by the peripheral groups can be used to extract the intramolecular conformation, i.e. to estimate twist and tilt angle. This method was applied for CoTTBPP on Ag(111), thus the reader is referred to [48] for details.

For 2HTTBPP on Cu(111) a twist angle of $\theta = 5 \pm 5^\circ$ and a tilt angle of $\phi = 35 \pm 5^\circ$ is determined for both conformations. The corresponding molecular models are sketched in Fig. 4.18. Indeed, the visibility of all eight di-tert-butyl groups with a similar apparent height indicates that the twist angle is close to zero and thus is

in good agreement with the estimated values. Note that in a recent DFT study of the energy surface of CoTTBPP in the gas phase, a local minimum was located at very similar twist and tilt angles ($\theta = 10^\circ$ and $\phi = 30^\circ$), albeit at relatively high energy. [116] In this conformation the molecule adopts a concave, bowl-like shape. Such a conformation is energetically unfavorable in the gas phase, but could be stabilized by molecule-substrate as well as lateral molecule-molecule interactions within a surface monolayer. Overall, the STM images suggest a bowl-like shape of the molecules with a bimodal appearance in STM. In the dark rows the molecules exhibit a concave conformation, while the molecules in the bright rows exhibit a convex conformation.

Furthermore, STM images are simulated on a three layer Cu slab, based on the experimentally determined conformations, by our cooperation partners N. Luckas, W. Hieringer and A. Görling from the Chair of Theoretical Chemistry at the Friedrich-Alexander-Universität Erlangen-Nürnberg. The simulated STM image, depicted in Fig. 4.18 (c), resembles the main features of the experimental data very well and thus confirms the proposed intramolecular conformations.

This type of bimodal appearance of a porphyrin molecule was not observed before. The concave conformation is in line with the previously reported strong attractive interactions of the iminic nitrogen atoms of 2HTPP with Cu(111).

4.3.2 Thermal activated conformational change

Detailed inspection of large-scale STM images reveals that the order within the rows is not perfect, i.e. in a convex row individual 2HTTBPPs exhibit a concave shape and vice versa. STM-Movies recorded at RT provide the explanation for this behavior: In both rows individual molecules occasionally change their conformation reversibly from convex to concave and vice versa (see Fig. 3.3). This demonstrates the metastable nature of the intramolecular conformation.

To visualize the conformational changes at RT, time profiles are extracted from “high speed” STM-Movies (see Ch. 3.5), for a concave and a convex row as indicated by the orange and blue line in Fig. 4.19 (a), such that four molecules per row can be traced. The profiles in Fig. 4.19 (b) show the apparent height as a function of time and

every change in the contrast in the vertical direction corresponds to one conformational change.

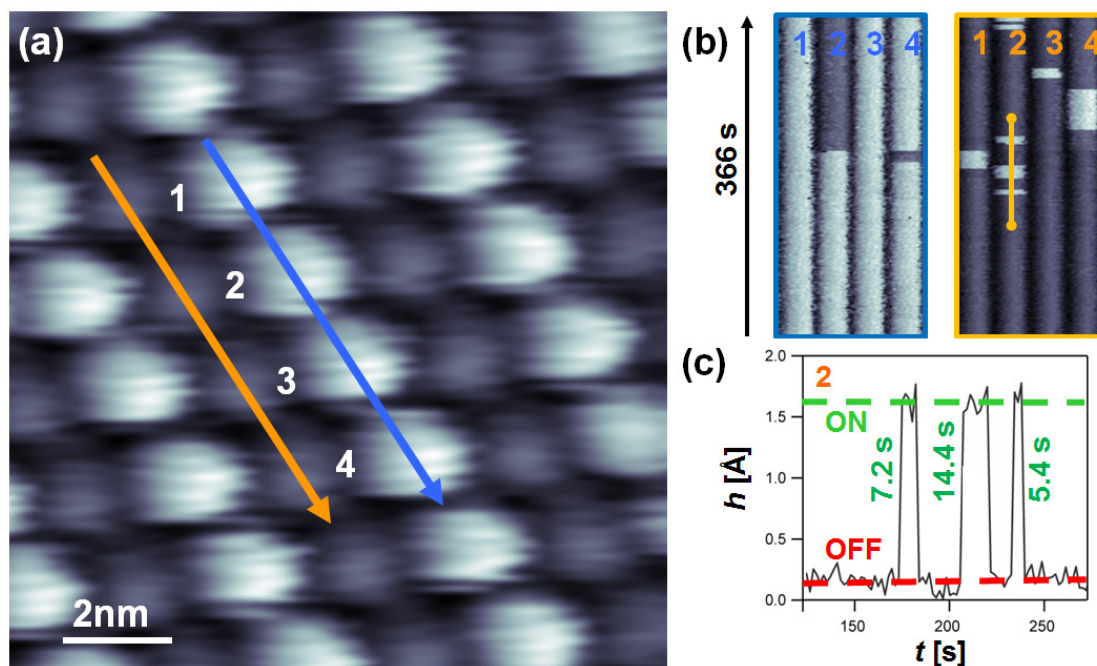


Figure 4.19: (a) STM image and (b) time profiles for a convex (blue) and concave (orange) row extracted from a STM-Movie at RT recorded with 200 images and an image-to-image acquisition time of 1.83 s. Each contrast change in the profiles corresponds to one conformational change. (c) Close-up on the time dependent conformational change of molecules 2 in the concave row. The tunneling parameters are: (a) $U_{\text{bias}} = +1.30$ V and $I_{\text{set}} = 30.0$ pA.

A close-up on the time dependent conformational change of molecules 2 in the concave row is given in Fig. 4.19 (c), where the apparent height in STM is plotted against the time. Here, two height levels can be distinguished which are correlated to the corresponding intramolecular conformation. Practically, the molecules constitute a two state system in which the two states could be assigned to arbitrary values like “on” and “off” as indicated in Fig. 4.19 (c), or correspondingly to “1” and “0” as used in information storage. Moreover, the close-up demonstrates that the corresponding lifetimes of the convex state are in the range of 5.2 s to 14.4 s and are thus well above the time resolution of 1.8 s for the “high speed” STM-Movie.

In order to address the temperature dependent behavior of the conformational change, “high speed” STM-Movies are recorded at different temperatures. In Fig. 4.20 time profiles extracted from these STM-Movies are shown. In both rows the number of transitions between the two conformations increases with increasing temperature and at the same time the lifetimes of the constrained state within the rows decreases. Interestingly, the transition rate in the concave row is much higher than in the convex row. This seems to be unexpected; if a similar strong interaction of the iminic nitrogen atoms with the Cu substrate atoms for the concave molecules is assumed, as it is the case for 2HTPP. Thus, the molecules in the concave rows should have the higher energy barrier for the transition than the molecules in the convex row.

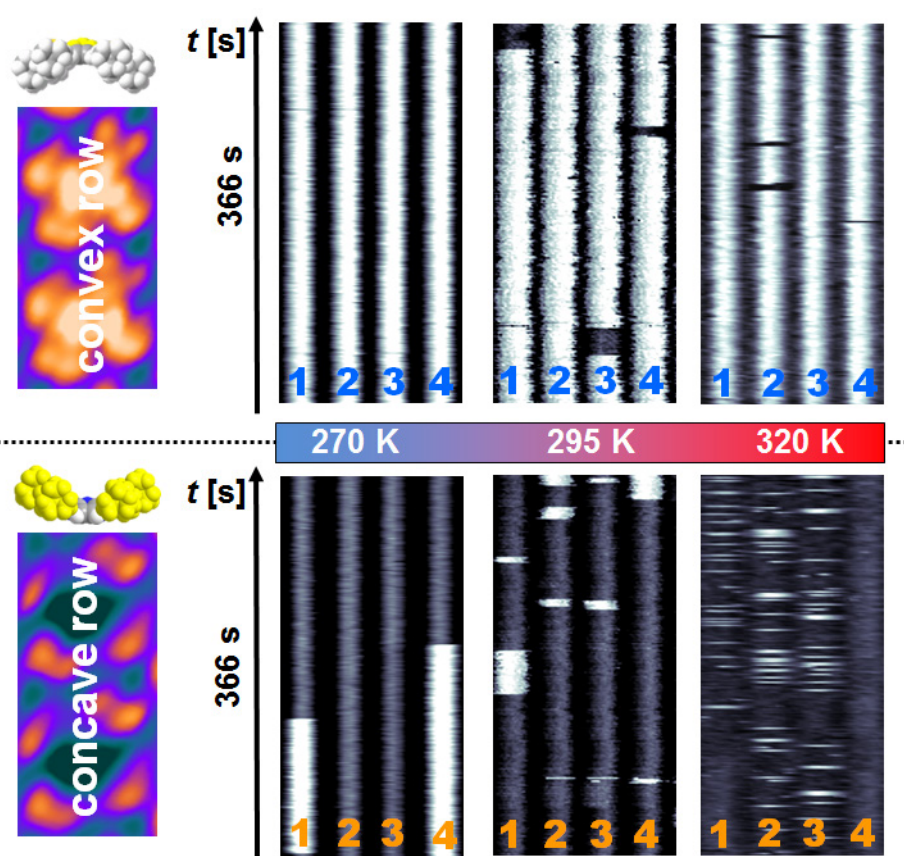


Figure 4.20: Time profiles for four molecules within a convex and concave row extracted from “high speed” STM-Movies recorded at the indicated temperatures. Each movie consist of 200 images with an image-to-image acquisition time of 1.83 s and tunneling parameters of $U_{\text{bias}} = +1.30 \text{ V}$ and $I_{\text{set}} = 30.0 \text{ pA}$.

Following the procedure described in Ch. 3.5, also a quantitative analysis of the “high speed” STM-Movies is performed, resulting in the evaluation of the transition rate $v(T)$ from convex to concave and vice versa (after equations 3.14 and 3.15) for both rows and for each investigated temperature. This means four different transition events are analyzed separately. When plotting the logarithm of $(v(T)/T)$ against the corresponding inverse temperature ($1/T$) a linear dependence is found (see Fig. 4.21). The derived values for the enthalpy ΔH^\ddagger and the entropy ΔS^\ddagger are denoted in Fig. 4.21. The comparison of the ΔH^\ddagger values for both rows shows that the barriers to overcome for the transition from concave to convex are the same within the margin of errors (0.92 ± 0.10 vs. 0.99 ± 0.04 eV; in red). The same holds for the other switching direction (0.76 ± 0.11 vs. 0.72 ± 0.04 eV; in blue).

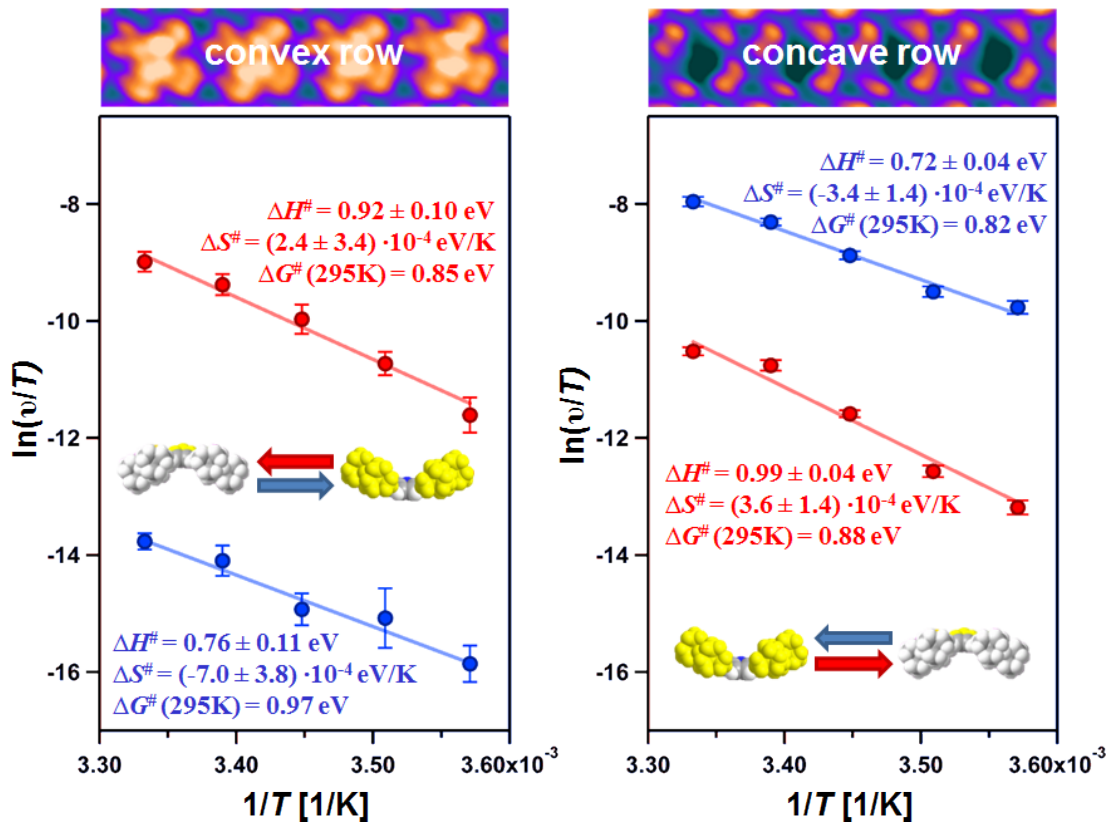


Figure 4.21: Plots of $\ln(v/T)$ versus $1/T$ for the two transition events concave to convex (red) and convex to concave (blue) in the convex row (left-hand side) and concave row (right-hand side). The corresponding ΔH^\ddagger and ΔS^\ddagger values determined from linear regression and calculated ΔG^\ddagger values for 295 K are given in the same color code.

Remarkably, the enthalpic barrier for the transition from concave to convex (red) is about 30% higher than for the opposite direction (blue). This is in line with the assumed strong interaction of the iminic nitrogen of the concave molecule with the Cu substrate. Despite the stronger interaction, the transition rate is larger in the concave row and in the convex row the concave conformation is not the favorable state. Following the Gibbs-Helmholtz equation, $\Delta G^\ddagger = \Delta H^\ddagger - T \cdot \Delta S^\ddagger$, not only the enthalpic contribution ΔH^\ddagger must be considered, but also the entropic contribution $-T \Delta S^\ddagger$. Therefore the convex state in the convex row becomes energetically favorable at 295 K (see ΔG^\ddagger values in Fig. 4.21). This means that the convex molecules in the convex rows and thus the whole supramolecular arrangement are entropically stabilized at 295 K. The concave state in the concave row is still the energetically favorable one at 295 K, even if the entropic contributions are considered (see ΔG^\ddagger values in Fig. 4.21).

4.3.3 Tip-induced conformational change at reduced temperature

At a temperature of 200 K, the thermally induced transition between the two conformations is effectively suppressed. Such a static layer enables the demonstration of a controlled manipulation with the STM tip, i.e. tip-induced conformational change. In Fig. 4.22 (b) a sequence of STM images is displayed, illustrating that individual convex molecules in a convex row change their conformation to concave by using comparably high bias voltages and local electron doses. To induce the conformational change, the tip is positioned directly above a convex molecule and the bias voltage is increased from $U_{\text{bias}} = +1.30$ to $+1.75$ V for 5 s while the feedback loop is closed and the tunneling current constant (see illustration in Fig. 4.22 a). Note that for lower bias voltages, between $+1.40$ and $+1.60$ V for 5-30 s, no conformational change from convex to concave is observed. By studying the tip-induced transition process systematically, it is found that a consecutive conformational change of directly neighboring molecules in a convex row leads to the destruction of the local supramolecular order. However, changing the conformation of every second molecule in the convex row, as shown in Fig. 4.22, leaves the supramolecular arrangement intact. Thus this system is suitable for information storage with a high information storage density of $4.9 \cdot 10^{13}$ bit/inch².

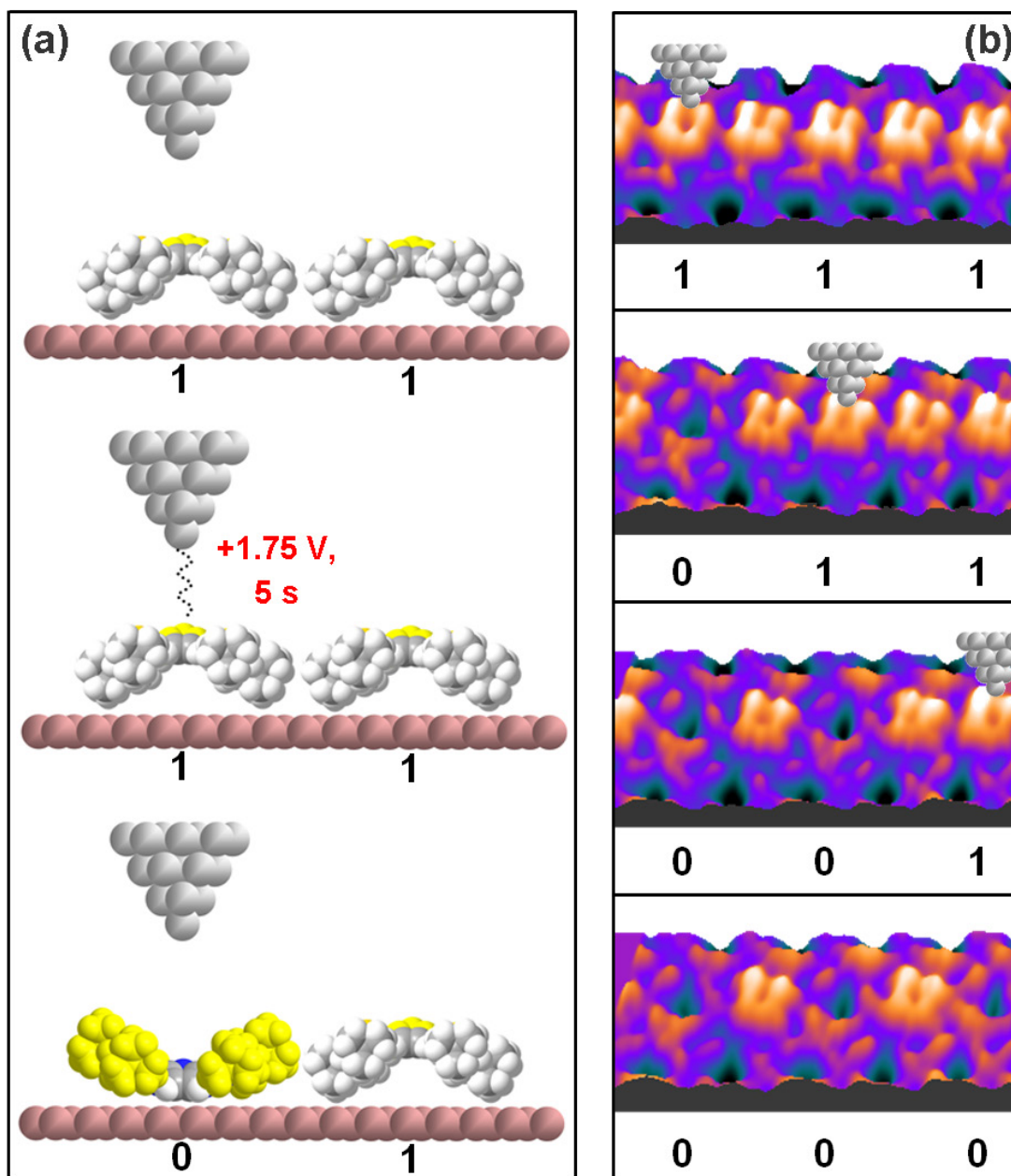


Figure 4.22: (a) Illustration of the tip-induced conformational change in the convex row. The STM tip is placed directly above a convex molecule for 5 s with $U_{\text{bias}} = +1.75 \text{ V}$ to induce the transition from convex to concave. (b) Series of STM images recorded at 200 K and $U_{\text{bias}} = +1.30 \text{ V}$ and $I_{\text{set}} = 30.0 \text{ pA}$. The tip positions before applying the voltage pulse are indicated by a schematic STM tip. In the subsequent images (from top to bottom) the tip-induced conformational change is visible.

Interestingly, the transition in the other direction, i.e. from concave to convex, in both rows, is not possible. One explanation for this behavior is that with decreasing temperature the entropic contributions to the free energy barrier decreases and thus the concave conformation becomes increasingly favorable also in the convex row. Apart from this thermodynamic consideration, the tip-induced conformational change is based on the impact of the tunneling electron and therefore also other processes like cross section for inelastic electron excitations or relaxation channels for excited states in the molecule play an important role. Furthermore the discussed strong coupling of the concave molecule with the copper substrate provides an effective decay channel for tip-induced excitations, which hinders the transition from concave to the convex.

4.3.4 Self-metalation reaction (unpublished data)

Since the self-metalation reaction was observed around 400 K for 2HTPP layers on Cu(111) [P3, P4], it seems to be very likely that at higher temperatures the self-metalation reaction of 2HTTBPP with Cu substrate atoms to CuTTBPP occurs.

Figure 4.23 (a) displays a 2HTTBPP layer with a coverage slightly below one monolayer at RT. Here, the typical bimodal appearance is clearly visible. STM images acquired at RT after annealing the layer to 360 K (see Fig. 4.23 b, c) and to 400 K show significant changes (see Fig. 4.23 d). Figure 4.23 (b) and (c) show two coexisting clearly distinguishable ordered phases after sample annealing to 360 K, namely a hexagonal (hex A) and a herringbone phase. The bimodal phase has completely vanished. Annealing to 400 K leads to the formation of a new hexagonal phase (hex B), and the hex A and herringbone phases have disappeared.

In the following, the properties of the observed molecular arrangements are described and elucidated in detail. For the estimation of the intramolecular conformation, i.e. twist and tilt angle, the dimension of the long and short sides of the rectangle formed by the peripheral groups of the molecular model are compared with the experimental data, as described before (see Ch. 4.3.1). The phase denoted as hex A (see Fig. 4.23 b) can be characterized by the two lattice constants $a = 1.66 \pm 0.1$ nm and $b = 1.90 \pm 0.1$ nm with an enclosed angle of $\alpha = 68 \pm 5^\circ$, resulting in a molecular density of $\rho = 0.32$ mol/nm². Thus the phase hex A is a slightly distorted hexagonal structure.

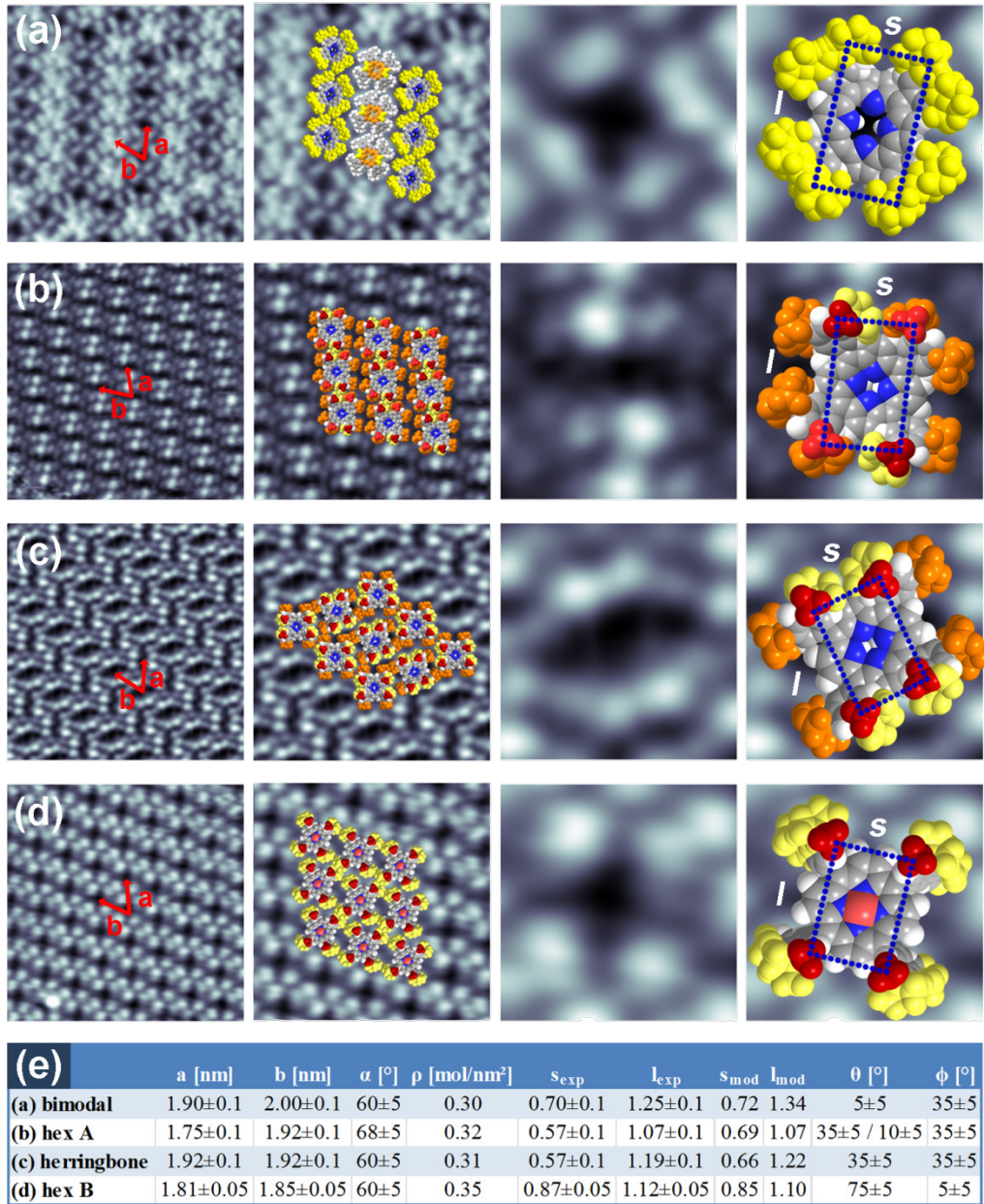


Figure 4.23: Overview of STM images of four different phases of 2HTTBPP and CuTTBPP with and without corresponding molecular models superimposed: (a) bimodal phase at RT, (b) and (c) hex A and herringbone phase after annealing to 360 K and (d) hex B phase after annealing to 400 K. (e) Overview of the values extracted from STM data and the corresponding model values. The size of the STM images is (13.5×13.5) nm² for the first column, (10×10) nm² for the second column and (2.5×2.5) nm² for the other columns. The tunneling parameters are (a) $U_{\text{bias}} = +1.76$ V, $I_{\text{set}} = 25.0$ pA (b), (c) $U_{\text{bias}} = +1.79$ V, $I_{\text{set}} = 31.2$ pA and (d) $U_{\text{bias}} = +1.81$ V, $I_{\text{set}} = 29.8$ pA.

The periphery of each molecule within the hex A phase appears as eight protrusions with different brightness. Two opposite protrusions close to the center appear brightest, whereas the protrusions furthest from the center appear dimmer. This results in two pairs of one very bright and one dim protrusion and another two pairs of one slightly bright and one dim protrusion arranged in four groups around the center corresponding to the four phenyl rings. Therefore, a geometry is suggested where two opposite phenyl groups are rotated to larger twist angles. The comparison between molecular model and experimental values yields a twist angle of the two stronger rotated opposite phenyl groups of $\theta = 35 \pm 5^\circ$ and the other two phenyl rings of $\theta = 10 \pm 5^\circ$ and a tilt angle of $\phi = 35 \pm 5^\circ$ (see scaled molecular model in Fig. 4.23 b). Compared with the values for 2HTTBPP in the bimodal phase (see Fig. 4.23 e), the twist angle of two phenyl groups is strongly increased.

Figure 4.23 (c) shows clearly that the structure of the herringbone phase consist of rows of parallel molecules where the molecules in adjacent rows are rotated by 90° to each other. If the azimuthal orientation of the molecules is neglected, a hexagonal arrangement is found, with lattice parameters of $a = b = 1.92 \pm 0.1$ nm and $\alpha = 60 \pm 5^\circ$, resulting in a molecular density of $\rho = 0.31$ mol/nm². Each molecule within the herringbone phase appears in STM with four bright protrusions close to the center and four dimmer protrusions. The comparison between molecular model and experimental values yields a twist angle of the phenyl groups of $\theta = 35 \pm 5^\circ$ and a tilt angle of $\phi = 35 \pm 5^\circ$ (see scaled molecular model in Fig. 4.23 c). Comparing the intramolecular conformation of the hex A and the herringbone phase, it seems that the hex A phase is a precursor to the herringbone structure. Since the molecular density of both phases is similar, a transition from hex A to the herringbone structure could be realized by an intramolecular transformation, i.e. increasing of the twist angle of two opposite phenyl groups, accompanied by a change of the azimuthal angle of the molecule. The herringbone structure was observed previously for CoTTBPP on Ag(111) after multilayer desorption at 550 K for 45 s. This indicates that the formation of the herringbone phase is an activated process.

Figure 4.23 (d) shows the molecular arrangement after annealing the sample to 400 K. The lattice constants of the hex B phase are $a = 1.81 \pm 0.05$ nm and $b = 1.85 \pm 0.05$ nm, which results in a molecular density of $\rho = 0.35$ mol/nm² (see

Fig. 4.23 d). Thus, this arrangement exhibits the highest molecular density. Individual molecules are identified by four bright spots, which can be assigned to four upper tert-butyl groups forming a rectangle. By comparing the values of the molecular model and experimental data, the twist angle is determined to $\theta = 75 \pm 5^\circ$ and the tilt angle to $\phi = 5 \pm 5^\circ$. The corresponding molecular model is sketched in Fig. 4.23 (d). The visibility of only four tert-butyl groups with similar apparent height also indicates a conformation with large twist angles. Note that in the DFT study of the energy surface of CoTTBPP in the gas phase, a broad energy minimum is found, located at very similar twist and tilt angles (around $\theta \sim 90\text{-}60^\circ$ and $\phi \sim 5^\circ$) at relatively low energy. [116]

Corresponding XPS measurements in the N 1s region of a 2HTTBPP layer before and after annealing to 400 K reveal also significant changes: Before annealing two distinct peaks are observed, belonging to the different pairs of iminic and aminic nitrogen atoms of 2HTTBPP, and after annealing one single peak is found. This indicates that 2HTTBPP molecules can also react with Cu atoms from the substrate to form CuTTBPP. As observed for 2HTPP, the inclusion of a metal atom into the porphyrin macrocycle leads to a significant change of the intramolecular conformation. Thus, the molecules within the hex B phase are regarded as CuTTBPP molecules.

4.4 Porphyrins on model-templates [P7]

In this chapter, the knowledge about the influence of molecule-substrate and molecule-molecule interactions on adsorption behavior, self-assembly and dynamic processes is expanded to generate templates for the adsorption of porphyrins to realize patterning via local anchoring or functionalization. In this regard, Cu(111) surfaces pre-covered with a submonolayer of copper oxide or metallic nickel are studied as model-templates for the selective adsorption and/or localized functionalization of functional molecules, such as 2HTPP, CoTPP or 2HOEP. The characterization as well as the preparation of the model-templates is described in Chapter 2.3.1 and 2.4.

4.4.1 Tetraphenylporphyrins on model-templates

First, the adsorption behavior of submonolayers of 2HTPP and CoTPP on a Cu(111) surface partly covered with a disordered surface copper oxide is shown at RT. In Fig. 4.24 (a), (b) STM images representative for the situation after the deposition are presented. Quite remarkably, the analysis of the STM image in Fig. 4.24 (a) reveals that 2HTPP molecules are mainly observed on the bare copper substrate (a single 2HTPP is green encircled), whereas only very few 2HTPP molecules can be found on top of the surface copper oxide (red encircled). A similar behavior is observed for CoTPP: the step edges of the copper oxide islands are completely decorated and small disordered agglomerates of CoTPP molecules are visible on the bare copper substrate, whereas no molecules are found on top of the copper oxide islands (see Fig. 4.24 b). These findings evidence a selective adsorption of the porphyrins on the free copper surface area, and the CoTPP molecules are additionally pinned at the rim of the copper oxide islands. The observed behavior requires sufficient mobility of 2HTPP and CoTPP on the copper oxide areas, as the deposition is realized by thermal evaporation and the molecules therefore statistically impinge on the surface (assuming a comparable sticking coefficient on the bare copper and the copper oxide). This indicates that the adsorption sites on top of the surface copper oxide structures are energetically unfavorable. The few 2HTPP molecules found on top of the copper oxide are probably located at defect sites. A detailed analysis of the CoTPP molecules located at the rim of the copper oxide structures (i.e. apparent height analysis) reveals that the molecules are adsorbed on the Cu surface and closely surrounded by oxygen, presumably similar to the NO-CoTPP phase observed on Ag(111) [117].

Next, the adsorption behavior of submonolayers of 2HTPP and CoTPP on a Cu(111) surface partly covered with metallic nickel is shown at RT. Extracted average images from STM-Movies illustrate the dynamic behavior. In Fig. 4.24 (c) 2HTPP molecules are adsorbed both on the Ni island and on the bare copper surface. On the latter the typical one-dimensional movement is observed, while on the Ni island isolated 2HTPP molecules are visible, which are completely confined to their adsorption sites, i.e. they do not move or rotate. Furthermore, the 2HTPP molecules on the Ni island exhibit the same appearance as 2HTPP on Cu(111) and three distinct azimuthal orientations of the molecules are found, rotated by multiples of 120° .

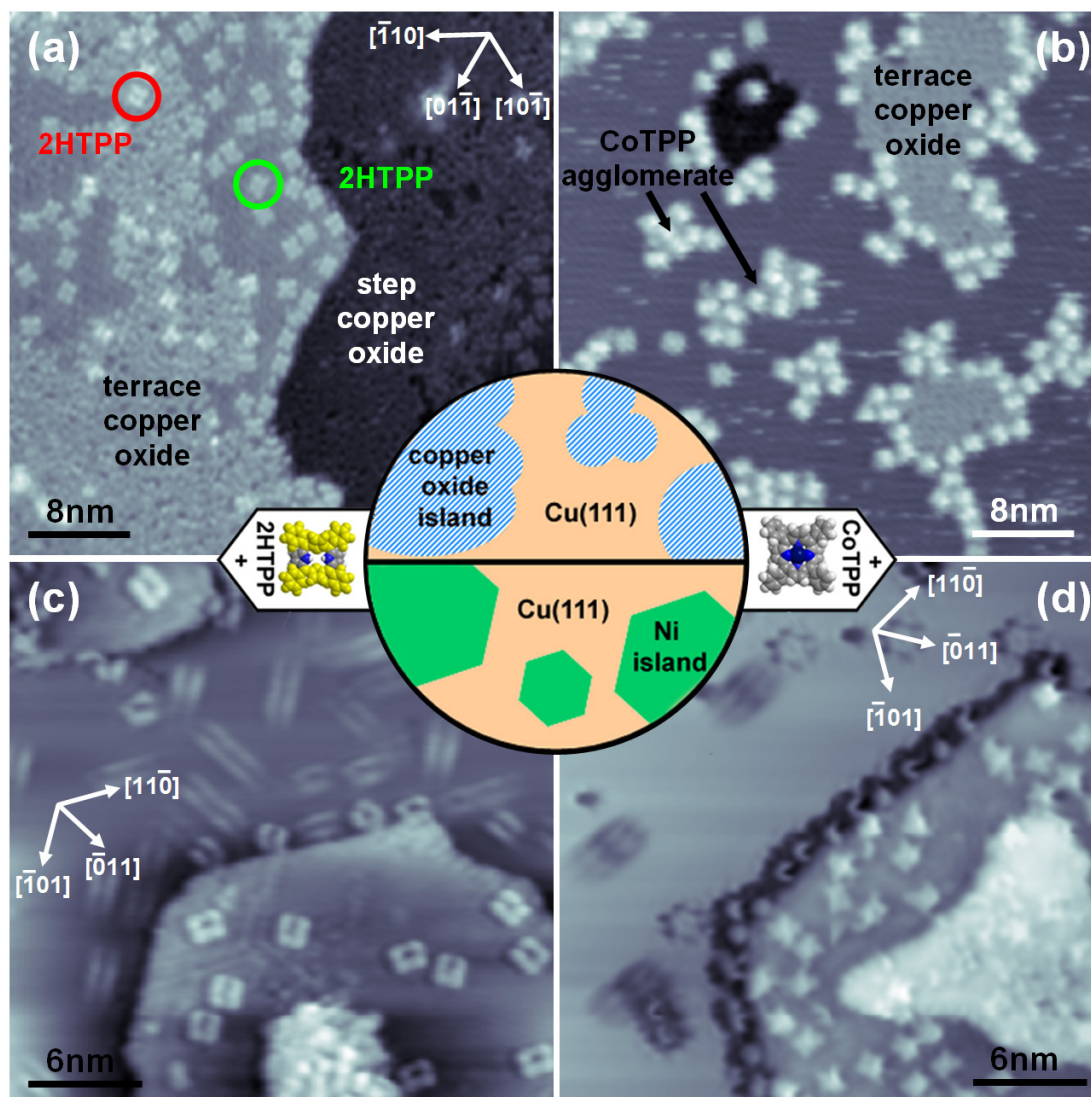


Figure 4.24: (a) and (b) STM images of 2HTPP and CoTPP adsorbed on the O/Cu(111) model-template at RT. (c) and (d) extracted average images from STM-Movies recorded at RT for 2HTPP and CoTPP deposited on the Ni/Cu(111) model-template. Tunneling parameters: (a) $U_{\text{bias}} = 1.00 \text{ V}$, $I_{\text{set}} = 97.9 \text{ pA}$ (b) $U_{\text{bias}} = -1.14 \text{ V}$, $I_{\text{set}} = 30.4 \text{ pA}$ (c) $U_{\text{bias}} = -1.18 \text{ V}$, $I_{\text{set}} = 25.2 \text{ pA}$ and (d) $U_{\text{bias}} = -0.88 \text{ V}$, $I_{\text{set}} = 34.3 \text{ pA}$. Average images: (c) 80 STM images with an image-to-image time of 25 s and (d) 51 STM images with an image-to-image time of 62 s.

These findings demonstrate a highly site-specific adsorption behavior and a similar adsorption geometry of 2HTPP on both metals. The reduced mobility of 2HTPP on the Ni island can be caused by a higher surface corrugation on the islands, probably due to a stronger molecule-substrate interaction at the preferred sites. Figure 4.24 (d)

presents an average image after deposition of CoTPP onto the model-template. On top of the Ni island, isolated molecules are observed with a well-defined orientation, i.e. oriented along one of the three densely packed Ni rows. Furthermore, CoTPP molecules decorate the rim of the Cu/Ni step-edges. Both at the rim and on the Ni island, the CoTPP molecules are completely confined to their adsorption sites. On the bare copper substrate no individual molecules are visible, but the background appears very bright in the average image, due to highly mobile CoTPP molecules. These findings demonstrate a highly site-specific adsorption behavior of CoTPP on the Ni island, which also can be the reason for its immobility. The detailed analysis of the CoTPP molecules at the rim of the Cu/Ni step-edge reveals that the molecules are located at the lower edge on the Cu(111) surface. The immobility at the Cu/Ni step-edges could be due to energetically favorable adsorption sites at the step-edges, and also lateral stabilization between the CoTPP molecules might contribute to the observed step decoration.

In summary, the observations indicate the possibility to pattern a surface with porphyrins by a given template. The model-template consisting of a Cu(111) surface pre-covered with a submonolayer of copper oxide is able to steer the adsorption behavior of TPP submonolayers: 2HTPP adsorbs selectively on the bare copper surface areas, and CoTPP is anchored at the rim of the copper oxide islands. In contrast, the model-template consisting of a Cu(111) surface pre-covered with metallic nickel strongly influences the dynamic behavior of 2HTPP and CoTPP. The two derivatives are practically pinned to a certain position on the Ni island, while they are mobile on the bare Cu surface.

4.4.2 Octaethylporphyrin on Ni/Cu(111)

In the following the investigation on the Ni/Cu(111) model-template is expanded to 2HOEP, which exhibits a different functionality than 2HTPP, i.e. different peripheral substituents are attached to the porphyrin macrocycle. Different studies of OEP on metal surfaces (e.g. 2HOEP and CoOEP on Ag(111) [118] and NiOEP on Ag(111) [119]) concluded a specific internal conformation with the macrocycle lying flat on the surface; thus the macrocycle is expected to be significantly closer to the surface, compared to TPP.

First, the adsorption behavior of 2HOEP on the bare Cu(111) surface at RT is discussed. 2HOEP molecules form well-ordered islands at RT, with a rhomboidal unit cell ($a = 1.45 \pm 0.10$ nm, $b = 1.31 \pm 0.10$ nm, $\alpha = 54^\circ \pm 4^\circ$) as shown in Fig. 4.25 (a). The high-resolution STM image reveals that each 2HOEP molecule appears with eight protrusions of similar apparent height close to the central cavity. This appearance on Cu(111) in STM is identical to that found for 2HOEP on Ag(111) at RT [118]. Thus, each protrusion can be attributed to one terminal ethyl group, pointing away from the surface.

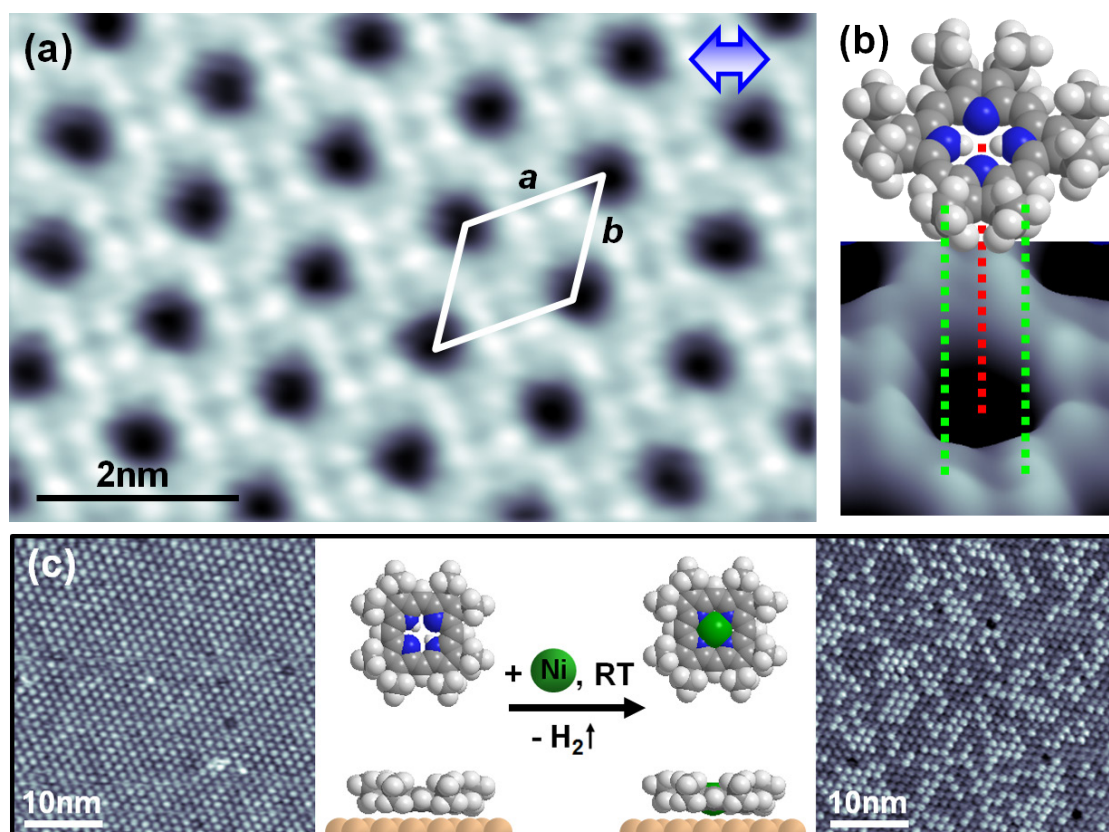


Figure 4.25: (a) STM image with submolecular resolution of 2HOEP Cu(111) at RT. (b) Top view model of 2HOEP illustrating the intramolecular conformation. (c) Direct metalation of a 2HOEP monolayer with post-deposited Ni atoms at RT. The appearance of individual molecules changes significantly after deposition of Ni and can be interpreted as the formation of NiOEP. The tunneling parameters are: (a) $U_{\text{bias}} = -0.14$ V, $I_{\text{set}} = 29.4$ pA and (c) left $U_{\text{bias}} = -0.86$ V, $I_{\text{set}} = 30.1$ pA and right $U_{\text{bias}} = -1.53$ V, $I_{\text{set}} = 27.1$ pA.

Next, the direct metalation of a 2HOEP monolayer on Cu(111) with post-deposited Ni atoms at RT is investigated. This reaction is of particular interest since it was observed that both 2HOEP and 2HTPP molecules adsorbed on Ag(111) react in the same way with post-deposited Fe atoms at RT [59, 61, 120], and furthermore the direct metalation of 2HTPP on Au(111) with post-deposited Ni atoms occurs already at RT [66]. Figure 4.25 (c) shows STM images with medium resolution of a 2HOEP monolayer before and after deposition of a specific amount of Ni at RT. The amount of deposited Ni atoms equals to the amount needed to complex one third of the 2HOEP monolayer, which should lead to a 2HOEP/NiOEP ratio of 2:1. Indeed, after deposition of Ni brighter and darker protrusions are observed in the STM at RT. Counting the different protrusions yields a ratio of 2:1 of darker and brighter spots, indicative of a successful metalation reaction. Thus, the brighter spots are identified as NiOEP and the darker spots as 2HOEP. The STM image after deposition of Ni resembles previously reported STM images of mixed monolayers of 2HOEP/CoOEP [81, 118], in which CoOEP is the species with the increased apparent height, due to the central Co ion.

Figure 4.26 represents the situation after deposition of submonolayers of 2HOEP on the Ni/Cu(111) model-template at RT. On the large hexagonal nickel island and on the 2nd story copper layer isolated molecules are observed. Remarkably, the molecules on the nickel island exhibit a central protrusion (see Fig. 4.26 b), whereas the molecules on the 2nd story copper exhibit a central cavity (see Fig. 4.26 c). On the bare copper surface only streaky features are visible, indicative for a highly mobile species, here 2HOEP. Note that for higher 2HOEP coverages the formation of well-ordered domains on the bare Cu(111) surface is observed (not shown here). Considering the above described metalation experiment it can be concluded that 2HOEP molecules are metalated to NiOEP on the Ni island, whereas on the 2nd story copper layer no metalation occurs.

These findings demonstrate that the Ni/Cu(111) model-template can act as a template for the localized metalation of 2HOEP. On the nickel islands metalation to NiOEP occurs at RT, whereas on the bare copper layer and on the 2nd story copper layer the 2HOEP molecules remain non-metalated.

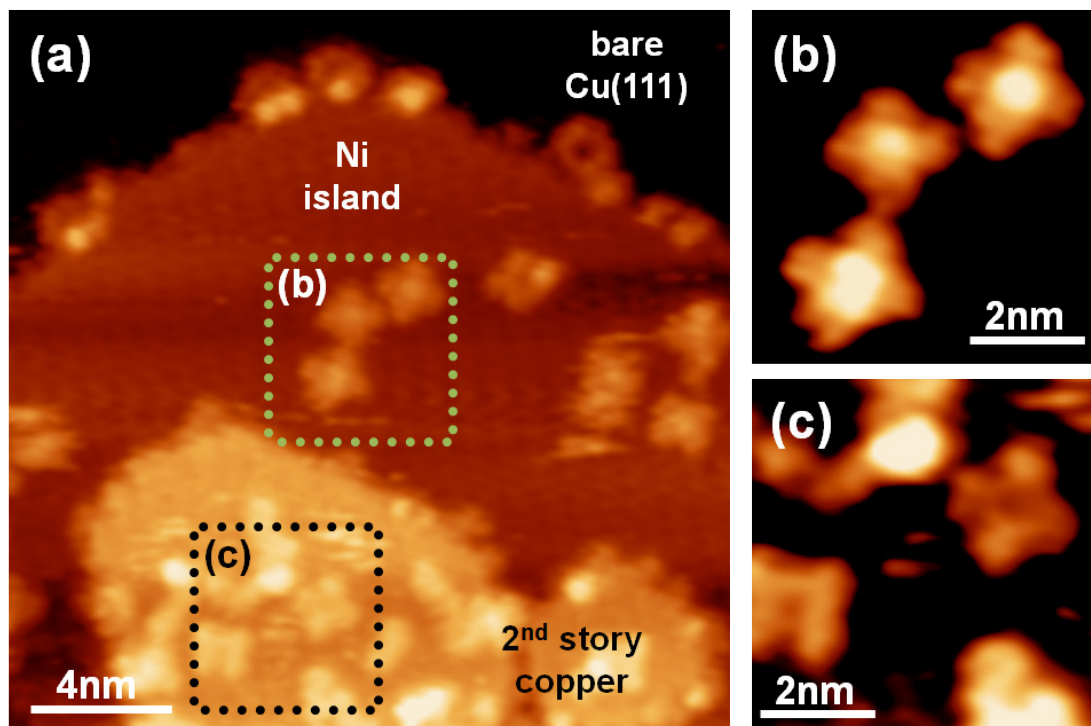


Figure 4.26: (a) Adsorption behavior of 2HOEP on the Ni/Cu(111) model-template at RT: (b) porphyrins on the Ni island exhibit a central protrusion, indicating the metalation of 2HOEP to NiOEP, (c) whereas porphyrins on the 2nd story copper layer exhibit a central cavity, indicative of free-base 2HOEP. The tunneling parameters are: (a)-(c) $U_{\text{bias}} = -0.11 \text{ V}$ and $I_{\text{set}} = 24.0 \text{ pA}$.

5 Summary

This thesis allows to gain a deeper fundamental understanding of porphyrins on surfaces. In particular, free-base and metalated tetraphenylporphyrins (TPP), tetrakisdi-*tert*-butylphenyl-porphyrins (TTBPP) and octaethylporphyrins (OEP) adsorbed on a Cu(111) surface were investigated with scanning tunneling microscopy (STM) around room temperature under ultra-high vacuum conditions. The detailed analysis of the ST micrographs revealed fundamental aspects of the ordering mechanism and identified the role of molecule-molecule and molecule-substrate interactions. Temperature dependent STM measurements allowed detailed insights into dynamic processes, such as surface diffusion, molecular rotation, conformational changes, and chemical reactions. The results are presented in a cumulative form; the full papers are attached in the Appendix.

For submonolayer coverages of 2HTPP adsorbed on Cu(111) at room temperature, the molecules are randomly distributed and form no supramolecular arrangement. From a combined STM and XPS study, the formation of a strong coordinative chemical bond to the Cu(111) surface via the iminic nitrogen atoms is deduced. As a result of this interaction the molecule is pulled towards the surface; thus it exhibits a flat intramolecular conformation, and is rather immobile at room temperature. Furthermore, coverage dependent STM studies revealed the formation of a checkerboard structure for higher 2HTPP coverages, which is stabilized by attractive molecule-molecule interactions.

To further elucidate the role of the iminic nitrogen atoms, also MTPP molecules (with $M = \text{Co}, \text{Cu}$) were investigated at RT. In MTPP, all nitrogen atoms are coordinated equally to the metal center. Thus the interaction with the substrate is reduced and the molecules are highly mobile. Due to attractive molecule-molecule interactions the formation of well-ordered islands is observed.

Moreover, upon deposition of mixtures of MTPP/2HTPP (with $M = \text{Co}, \text{Cu}$) on Cu(111) at RT an effective phase separation is observed, based on the different adsorption behaviors of the two derivatives.

As a result of the strong, site specific molecule-substrate interactions with the Cu substrate, 2HTPP molecules show a one dimensional diffusion along one of the three densely packed Cu substrate rows. Time-resolved STM measurements at different temperatures (between 280 and 330 K) enabled a detailed investigation of this dynamic process. The energy barrier for migration was determined to $E_m = 0.71 \pm 0.08$ eV and a pre-exponential factor of $A_m = 10^{10.9 \pm 1.4} \text{ s}^{-1}$, by performing an Arrhenius analysis. At temperatures above 305 K, the molecules occasionally change their diffusion direction by $\pm 120^\circ$ from one densely packed Cu substrate row to another (i.e. rotation). The analysis of these rotation events in the temperature range from 305 to 330 K enabled the determination of the energy barrier for rotation to $E_r = 1.28 \pm 0.12$ eV and the corresponding pre-exponential factor to $A_r = 10^{17.0 \pm 1.8} \text{ s}^{-1}$.

In a next step, the adsorption behavior of 2HTPP on Cu(111) was investigated for higher temperatures. Around 400 K the molecules undergo a self-metalation reaction with the Cu substrate atoms to form CuTPP. Annealing to 450 and 500 K leads to irreversible intramolecular changes of the in-situ generated CuTPP molecules, due to successive dehydrogenation reactions of β - and/or ortho- hydrogen atoms.

For very low 2HTPP coverages, the reaction kinetics of the self-metalation was determined. The different appearance in STM and the different adsorption behavior of 2HTPP and CuTPP allowed to investigate the progress of the metalation under isothermal conditions, by determination of the molecular density of 2HTPP as a function of annealing time. The Arrhenius analysis resulted in an activation energy of $E_s = 1.48 \pm 0.12$ eV and a pre-exponential factor of $A_s = 10^{15 \pm 1.6} \text{ s}^{-1}$. The experimental values are found to agree very well with values obtained from DFT calculations in the gas phase.

The coverage dependence of the self-metalation reaction shows an abrupt increase of the metalation rate, which coincides with the formation of the checkerboard structure.

2HTTBPP molecules adsorbed on Cu(111) form a peculiar supramolecular ordered phase, in which the molecules are arranged in alternating rows with two distinct appearances in STM due to convex and concave conformations. Around room temperature, frequent reversible conformational changes of individual molecules were observed. The detailed temperature dependent analysis of the transition process revealed that the arrangement was entropically stabilized at room temperature. At 200 K, a controlled STM tip-induced unidirectional transition from convex to concave is possible, which yields an information storage density of $4.9 \cdot 10^{13}$ bit/inch².

The acquired knowledge about the influence of molecule-substrate and molecule-molecule interactions on the adsorption behavior and the detailed investigation of dynamic processes was expanded to generate defined functional molecular structures. The functionality of templated self-assembly was demonstrated on the basis of two model-templates, i.e. Cu(111) surfaces pre-covered with submonolayers of copper oxide or metallic nickel, on which the selective adsorption and/or localized functionalization of TPP and OEP molecules were investigated. The copper oxide model-template is able to direct the adsorption behavior of 2HTPP and CoTPP: 2HTPP adsorbs selectively on the bare copper surface areas, while CoTPP is found to anchor at the rim of the copper oxide islands. In contrast, the Ni/Cu(111) model-template strongly influences the dynamic behavior of the two TPP derivatives. They are practically pinned to certain positions on the Ni islands, while they are mobile on the bare Cu surface. Furthermore, the Ni/Cu(111) model-template can also act as a template for the localized metalation of 2HOEP. On the nickel islands metalation to NiOEP occurs at room temperature, whereas on the bare copper layer the 2HOEP molecules remain non-metalated.

Overall, the findings presented in this thesis contain valuable insights for the generation of functional molecular devices.

6 Zusammenfassung

Die vorliegende Arbeit erlaubt einen tiefgehenden und grundlegenden Einblick auf das Verhalten von Porphyrinen auf Oberflächen. Im Besonderen wurden unmetallierte und metallierte Tetraphenylporphyrine (TPP), Tetrakisdi-tert-butylphenylporphyrine (TTBPP) und Octaethylporphyrine (OEP) auf einer Cu(111)-Oberfläche mittels Rastertunnelmikroskopie (engl. scanning tunneling microscopy, STM) bei Raumtemperatur und im Ultrahochvakuum untersucht. Durch eine ausführliche Analyse der Rastertunnelmikroskopie-Bilder konnten grundlegende Aspekte aufgezeigt werden, welche die Molekülanordnung bestimmen. Dies geschah basierend auf der Untersuchung von Molekül-Molekül- und Molekül-Substrat-Wechselwirkungen. Des Weiteren gewährten temperaturabhängige STM-Messungen einen detaillierten Einblick in dynamische Prozesse, wie zum Beispiel Diffusion auf Oberflächen, Molekülrotation, Konformationsänderungen und chemische Reaktionen. Die Ergebnisse sind in einer kumulativen Form dargestellt; die Veröffentlichungen befinden sich im Anhang.

Die Adsorption einer Submonolage von 2HTPP-Molekülen auf einer Cu(111)-Oberfläche bei Raumtemperatur führt zu einer zufälligen Verteilung der Moleküle auf der Oberfläche. Dieses Adsorptionsverhalten konnte durch eine gemeinsame STM- und XPS-Studie auf die Ausbildung einer starken koordinativen chemischen Bindung zwischen den iminischen Stickstoffatomen des 2HTPP-Moleküls und Kupfersubstratomen zurückgeführt werden. Durch diese Wechselwirkung wird das Molekül an die Kupferoberfläche herangezogen, wodurch es eine flache intramolekulare Konformation einnimmt und daher bei Raumtemperatur auf der Oberfläche relativ unbeweglich ist. STM-Untersuchungen zur Bedeckungsabhängigkeit zeigten, dass 2HTPP-Moleküle bei einer höheren Bedeckung eine Schachbrettstruktur ausbilden, welche durch attraktive Molekül-Molekül-Wechselwirkungen stabilisiert wird.

Der Einfluss der iminischen Stickstoffatome auf das Adsorptionsverhalten wurde genauer untersucht, in dem MTPP-Moleküle (mit $M = \text{Co}, \text{Cu}$) auf eine Cu(111)-Oberfläche bei Raumtemperatur aufgebracht wurden. In MTPP-Molekülen sind alle vier Stickstoffatome gleichmäßig an das Metallzentrum koordiniert, wodurch die Wechselwirkung mit der Oberfläche vermindert ist und die Moleküle dadurch äußerst mobil sind. Die Anordnung der Moleküle in wohlgeordneten Inseln wird deshalb auf attraktive Molekül-Molekül-Wechselwirkungen zurückgeführt.

Darüber hinaus wurde beim Aufbringen einer Mischung aus 2HTPP/MTPP (mit $M = \text{Co}, \text{Cu}$) auf eine Cu(111)-Oberfläche bei Raumtemperatur eine effektive Phasentrennung beobachtet, welche auf das unterschiedliche Adsorptionsverhalten der beiden Derivate zurückzuführen ist.

Als Folge der starken, spezifischen Molekül-Substrat-Wechselwirkungen bewegen sich 2HTPP-Moleküle jeweils entlang einer der drei Vorzugsrichtungen des Kupfersubstrates. Dieser dynamische Prozess wurde mittels zeitaufgelöster STM-Messungen bei verschiedenen Temperaturen (zwischen 280 und 330 K) detailliert untersucht. Mit Hilfe einer Arrhenius-Analyse wurde die Energiebarriere für die Oberflächendiffusion zu $E_m = 0.71 \pm 0.08 \text{ eV}$ und der präexponentielle Faktor zu $A_m = 10^{10.9 \pm 1.4} \text{ s}^{-1}$ bestimmt. Zusätzlich wurde ab einer Temperatur von 305 K eine gelegentliche Änderung der Diffusionsrichtung der Moleküle um $\pm 120^\circ$ (d.h. Rotation) beobachtet. Die Auswertung dieser Rotationsereignisse im Temperaturbereich von 305 bis 330 K ermöglichte die Bestimmung der Energiebarriere für die Rotation zu $E_r = 1.28 \pm 0.12 \text{ eV}$ und des präexponentiellen Faktors zu $A_r = 10^{17.0 \pm 1.8} \text{ s}^{-1}$.

Weitere Untersuchungen betrachteten das Adsorptionsverhalten von 2HTPP auf einer Cu(111)-Oberfläche bei höheren Temperaturen. Der Beginn der Selbstmetallierung mit Kupfersubstratomen und damit die Ausbildung des Reaktionsproduktes CuTPP wurde ab 400 K beobachtet. Eine weitere Temperaturerhöhung auf 450 und 500 K führte zu einer irreversiblen intramolekularen Veränderung der in-situ erzeugten CuTPP-Moleküle, hervorgerufen durch eine schrittweise Dehydrierung von β - und/oder ortho-Wasserstoffatomen.

Die Reaktionskinetik der Selbstmetallierung wurde für sehr niedrige 2HTPP-Bedeckungen bestimmt. Dabei ermöglichten die verschiedenen Erscheinungsbilder des Eduktes 2HTPP und des Reaktionsproduktes CuTPP im STM sowie das unterschiedliche Adsorptionsverhalten die Beobachtung der Metallierungsreaktion unter isothermen Bedingungen, indem die molekulare Dichte von 2HTPP in Abhängigkeit der Heizdauer ermittelt wurde. Über die entsprechende Arrhenius-Analyse wurde die Aktivierungsenergie zu $E_s = 1.48 \pm 0.12$ eV und der präexponentielle Faktor zu $A_s = 10^{15 \pm 1.6} \text{ s}^{-1}$ bestimmt. Die experimentell bestimmte Energiebarriere stimmt dabei gut mit DFT-Berechnungen in der Gasphase überein.

Bei der Untersuchung der bedeckungsabhängigen Selbstmetallierung wurde ein unerwarteter Anstieg der Metallierungsrate gefunden, welcher mit der Ausbildung der Schachbrettstruktur zusammenfällt.

2HTTBPP-Moleküle bilden auf einer Cu(111)-Oberfläche bei Raumtemperatur eine charakteristische, supramolekular geordnete Phase aus. Die Moleküle in dieser Phase nehmen eine von zwei im STM deutlich voneinander unterscheidbaren Konformationen ein, eine konkave oder eine konvexe, welche in abwechselnden Reihen angeordnet sind. Bei Raumtemperatur wurden wiederholte reversible Konformationsänderungen einzelner Moleküle beobachtet. Die detaillierte Analyse dieses Prozesses in Abhängigkeit von der Temperatur zeigte, dass die supra-molekulare Anordnung bei Raumtemperatur entropisch stabilisiert ist.

Bei einer Temperatur von 200 K wurde das kontrollierte unidirektionale Schalten von der konvexen zur konkaven Konformation mit Hilfe der STM-Spitze gezeigt, wodurch ein Informationsspeicher mit einer Speicherdichte von $4.9 \cdot 10^{13}$ bit/inch² erreicht werden konnte.

Mit dem gewonnenen Wissen über den Einfluss von Molekül-Substrat- und Molekül-Molekül-Wechselwirkungen auf das Adsorptionsverhalten von Molekülen und der detaillierten Untersuchung von dynamischen Prozessen können definierte funktionelle molekulare Strukturen erzeugt werden. Anhand von Modell-Templaten, bestehend aus einer, mit Submonolagen Kupferoxid bzw. metallischem Nickel vorstrukturierten Cu(111)-Oberfläche, wurde die Funktionsweise einer substratgesteuerten Selbst-

anordnung demonstriert. Auf diesen Templaten wurden die selektive Adsorption und/oder die lokale Funktionalisierung von TPP und OEP Molekülen untersucht. Kupferoxid-Template beeinflussen das Adsorptionsverhalten von 2HTPP und CoTPP derart, dass 2HTPP selektiv auf den reinen Kupferbereichen adsorbiert, während CoTPP am Rand der Kupferoxid-Inseln verankert ist. Im Gegensatz dazu beeinflusst das Ni/Cu(111)-Templat sehr stark das dynamische Verhalten der beiden TPP Derivate. Auf den Ni-Inseln sind die Moleküle an bestimmten Positionen fest verankert und unbeweglich, während die Moleküle auf den freien Kupferoberflächen beweglich sind. Darüber hinaus fungiert das Ni/Cu(111) –Templat für die lokalisierte Metallierung von 2HOEP Molekülen: Bei Raumtemperatur werden die Moleküle auf den Ni-Inseln zu NiOEP metalliert, während die 2HOEP Moleküle auf dem freien Kupfersubstrat unmetalliert bleiben.

Abschließend kann festgestellt werden, dass die Ergebnisse dieser Arbeit einen wertvollen Einblick im Hinblick auf die Erzeugung von funktionellen Baugruppen ermöglichen.

7 Literature

- [1] D. Monti *et al.*, *J. Sens.* 2009 (2009) 856053-856063.
- [2] G. M. Whitesides, *Small* 1 (2005) 172-179.
- [3] Intel, *Intel 22 nm 3-D Tri-Gate Transistor Technology*, 5/2013, <http://www.intel.com>
- [4] G. E. Moore, *Electronics* 38 (1965) 114-117.
- [5] B. D. Gates *et al.*, *Chem. Rev.* 105 (2005) 1171-1196.
- [6] T. A. Jung *et al.*, *Science* 271 (1996) 181-184.
- [7] G. Binnig, H. Rohrer, *Surf. Sci.* 126 (1983) 236-244.
- [8] G. Binnig, H. Rohrer, C. Gerber, E. Weibel, *Phys. Rev. Lett.* 49 (1982) 57-61.
- [9] F. Moresco, C. Joachim, K. H. Rieder, *Surf. Interface Anal.* 36 (2004) 109-113.
- [10] J. A. Stroschio, D. M. Eigler, *Science* 254 (1991) 1319-1326.
- [11] K. H. Rieder *et al.*, *Europhys. News* 34 (2003) 95-98.
- [12] K. H. Rieder *et al.*, *Philos. Trans. R. Soc. London* 362 (2004) 1207-1216.
- [13] W. Ho, *J. Chem. Phys.* 117 (2002) 11033-11061.
- [14] L. R. Milgrom, *The colour of Life*, Oxford University Press, Oxford, (1997).
- [15] H. Marbach, *Habilitation treatise*, FAU Erlangen-Nürnberg, Erlangen (2010).
- [16] P. B. Messersmith, M. Textor, *Nat. Nanotechnol.* 2 (2007) 138-139.
- [17] F. Davis, S. P. J. Higson, *J. Biosens. Bioelectron.* 21 (2005) 1-20.
- [18] F. Rosei *et al.*, *Prog. Surf. Sci.* 71 (2003) 95-146.
- [19] C. J. Baddeley, *Top. Catal.* 25 (2003) 17-28.
- [20] G. M. Whitesides, J. P. Mathias, C. T. Seto, *Science* 254 (1991) 1312-1319.
- [21] J. M. Gottfried, H. Marbach, *Z. Phys. Chem.* 223 (2009) 53-74.
- [22] J. Brede *et al.*, *Nanotechnology* 20 (2009) 275602-275612.
- [23] F. Buchner *et al.*, *Phys. Chem. Chem. Phys.* 12 (2010) 13082-13090.
- [24] W. Auwärter *et al.*, *J. Chem. Phys.* 124 (2006) 194708.
- [25] W. Auwärter *et al.*, *J. Am. Chem. Soc.* 129 (2007) 11279-11285.
- [26] G. Rojas *et al.*, *J. Phys. Chem. C* 114 (2010) 9408-9415.
- [27] M. Eichberger *et al.*, *Nano Lett.* 8 (2008) 4608-4613.
- [28] H. Spillmann *et al.*, *Adv. Mat.* 18 (2006) 275-279.
- [29] D. Bonifazi *et al.*, *Angew. Chem., Int. Ed.* 43 (2004) 4759-4763.
- [30] F. Cicoira *et al.*, *Small* 2 (2006) 1366-1371.
- [31] F. Cicoira, J. A. Miwa, D. F. Perepichka, F. Rosei, *J. Phys Chem. A* 111 (2007) 12674-12678.
- [32] R. Otero *et al.*, *Angew. Chem., Int. Ed.* 43 (2004) 2092-2095.
- [33] P. Jiang *et al.*, *J. Am. Chem. Soc.* 130 (2008) 7790-7791.
- [34] J. C. Dunphy *et al.*, *Phys. Rev. B* 57 (1998) 12705-12708.
- [35] L. J. Lauhon, W. Ho, *J. Chem. Phys.* 111 (1999) 5633-5636.
- [36] J. Weckesser, J. V. Barth, K. Kern, *J. Chem. Phys.* 110 (1999) 5351-5354.
- [37] M. Schunack *et al.*, *Phys. Rev. Lett.* 88 (2002) 156102-156106.

- [38] R. Otero *et al.*, *Nat. Mater.* 3 (2004) 779-782.
- [39] Y. Shirai *et al.*, *Nano Lett.* 5 (2005) 2330-2334.
- [40] T. Kudernac *et al.*, *Nature* 479 (2011) 208-211.
- [41] K. Y. Kwon *et al.*, *Phys. Rev. Lett.* 95 (2005) 166101-166105.
- [42] J. K. Gimzewski *et al.*, *Science* 281 (1998) 531-533.
- [43] M. Stöhr *et al.*, *Phys. Rev. B* 65 (2001) 33404-33408.
- [44] M. Fendrich, T. Wagner, M. Stöhr, R. Möller, *Phys. Rev. B* 73 (2006) 115433-115440.
- [45] M. Wahl *et al.*, *Chem. Commun.* (2007) 1349-1351.
- [46] A. E. Baber, H. L. Tierney, E. C. H. Sykes, *ACS Nano* 2 (2008) 2385-2391.
- [47] T. A. Jung, R. R. Schlittler, J. K. Gimzewski, *Nature* 386 (1997) 696-698.
- [48] F. Buchner *et al.*, *J. Phys. Chem. C* 111 (2007) 13531-13538.
- [49] Y. F. Wang, J. Kroger, R. Berndt, W. A. Hofer, *J. Am. Chem. Soc.* 131 (2009) 3639-3643.
- [50] X. H. Qiu, G. V. Nazin, W. Ho, *Phys. Rev. Lett.* 93 (2004).
- [51] S. Weigelt *et al.*, *Nat. Mater.* 5 (2006) 112-117.
- [52] N. A. Rakow, K. S. Suslick, *Nature* 406 (2000) 710-713.
- [53] B. R. Takulapalli *et al.*, *J. Am. Chem. Soc.* 130 (2008) 2226-2233.
- [54] A. Yella *et al.*, *Science* 334 (2011) 1203-1203.
- [55] L. Schmidt-Mende *et al.*, *Chemphyschem* 6 (2005) 1253-1258.
- [56] I. Mochida, K. Suetsugu, H. Fujitsu, K. Takeshita, *J. Chem. Soc., Chem. Commun.* (1982) 166-167.
- [57] J. Nowakowski *et al.*, *Chem. Commun.* 49 (2013) 2347-2349.
- [58] J. M. Gottfried *et al.*, *J. Am. Chem. Soc.* 128 (2006) 5644-5645.
- [59] F. Buchner *et al.*, *Chemphyschem* 8 (2007) 241-243.
- [60] G. Di Santo *et al.*, *J. Phys. Chem. C* 115 (2011) 4155-4162.
- [61] F. Buchner *et al.*, *J. Phys. Chem. C* 112 (2008) 15458-15465.
- [62] W. Auwärter *et al.*, *Chemphyschem* 8 (2007) 250-254.
- [63] K. Flechtner *et al.*, *J. Phys. Chem. C* 111 (2007) 5821-5824.
- [64] A. Weber-Bargioni *et al.*, *J. Phys. Chem. C* 112 (2008) 3453-3455.
- [65] D. Écija *et al.*, *Angew. Chem., Int. Ed.* 50 (2011) 3872-3877.
- [66] M. Chen *et al.*, *J. Phys. Chem. C* 114 (2010) 9908-9916.
- [67] R. González-Moreno *et al.*, *J. Phys. Chem. C* 115 (2011) 6849-6854.
- [68] C. M. Doyle *et al.*, *Chem. Commun.* 47 (2011) 12134-12136.
- [69] S. Haq *et al.*, *J. Am. Chem. Soc.* 133 (2011) 12031-12039.
- [70] K. Diller *et al.*, *J. Chem. Phys.* 136 (2012) 014705-014713.
- [71] A. Goldoni *et al.*, *ACS Nano* 6 (2012) 10800-10807.
- [72] T. E. Shubina *et al.*, *J. Am. Chem. Soc.* 129 (2007) 9476-9483.
- [73] Y. Li *et al.*, *J. Am. Chem. Soc.* 134 (2012) 6401-6408.
- [74] R. Young, J. Ward, S. Fredric, *Rev. Sci. Instrum.* 43 (1972) 999-1011.
- [75] G. Binnig, H. Rohrer, *Helv. Phys. Acta* 55 (1982) 726-735.
- [76] N. Yao, Z. L. Wang, *Handbook of Microscopy for Nanotechnology*, Springer, New York, (2005).
- [77] R. Wiesendanger, *Scanning Probe Microscopy and Spectroscopy*, Cambridge University Press, Cambridge, (1994).
- [78] K. Oura *et al.*, *Surface Science - An Introduction*, Springer, New York, (2003).
- [79] I. Horcas *et al.*, *Rev. Sci. Instrum.* 78 (2007) 013705-013713.
- [80] R. Lindner, *PhD thesis*, FAU Erlangen-Nürnberg, Nürnberg (2004).

- [81] F. Buchner, *PhD thesis*, FAU Erlangen-Nürnberg, Erlangen (2010).
- [82] S. Pons, P. Mallet, L. Magaud, J. Y. Veuille, *Surf. Sci.* 511 (2002) 449-458.
- [83] S. Pons, P. Mallet, J. Y. Veuille, *Phys. Rev. B* 64 (2001) 193408.
- [84] H. L. Skriver, N. M. Rosengaard, *Phys. Rev. B* 45 (1992) 9410-9412.
- [85] L. Vitos, A. V. Ruban, H. L. Skriver, J. Kollar, *Surf. Sci.* 411 (1998) 186-202.
- [86] K. F. Wojciechowski, *Surf. Sci.* 437 (1999) 285-288.
- [87] T. Matsumoto *et al.*, *Surf. Sci.* 471 (2001) 225-245.
- [88] F. Wiame, V. Maurice, P. Marcus, *Surf. Sci.* 601 (2007) 1193-1204.
- [89] J. W. Steed, J. L. Atwood, *Supramolecular Chemistry*, Wiley & Sons, Chichester, (2009).
- [90] G. P. Moss, *Pure & Appl. Chem.* 59 (1987) 779-832.
- [91] F. Moresco *et al.*, *Surf. Sci.* 499 (2002) 94-102.
- [92] F. Moresco *et al.*, *Phys. Rev. Lett.* 86 (2001) 672-675.
- [93] A. Weber-Bargioni *et al.*, *Chemphyschem* 9 (2008) 89-94.
- [94] S. Arrhenius, *Z. Phys. Chem.* 4 (1889) 226-248.
- [95] H. Eyring, *J. Phys. Chem.* 3 (1935) 107-115.
- [96] D. J. Winzor, C. M. Jackson, *J. Mol. Recognit.* 19 (2006) 389-407.
- [97] K. Morgenstern, *Phys. Status Solidi B* 242 (2005) 773-796.
- [98] K. Morgenstern, G. Rosenfeld, B. Poelsema, G. Comsa, *Surf. Sci.* 352 (1996) 956-959.
- [99] J. J. Schulz, R. Koch, K. H. Rieder, *Phys. Rev. Lett.* 84 (2000) 4597-4600.
- [100] J. V. Barth, *Surf. Sci. Rep.* 40 (2000) 75-149.
- [101] G. Antczak, G. Ehrlich, *Surface Diffusion - Metals, Metal Atoms, and Clusters*, Cambridge University Press, Cambridge, (2010).
- [102] K. D. Dobbs, D. J. Doren, *J. Chem. Phys.* 97 (1992) 3722-3735.
- [103] F. Buchner *et al.*, *J. Phys. Chem. C* 113 (2009) 16450-16457.
- [104] K. Comanici *et al.*, *Langmuir* 24 (2008) 1897-1901.
- [105] K. Comanici, *PhD thesis*, FAU Erlangen-Nürnberg, Erlangen (2007).
- [106] M. Stark *et al.*, *Langmuir* 29 (2013) 4104-4110.
- [107] F. Bischoff *et al.*, *ACS Nano* 7 (2013) 3139-3149.
- [108] M. S. Liao, S. Scheiner, *J. Chem. Phys.* 117 (2002) 205-219.
- [109] H. Yanagi *et al.*, *Nano Lett.* 2 (2002) 601-604.
- [110] J. Ikonov, P. Bach, R. Merkel, M. Sokolowski, *Phys. Rev. B* 81 (2010) 161412-161416.
- [111] T. Yokoyama, T. Takahashi, K. Shinozaki, *Phys. Rev. B* 82 (2010) 155414-155419.
- [112] J. Weckesser, J. V. Barth, K. Kern, *Phys. Rev. B* 64 (2001) 161403-161407.
- [113] R. Zacharia, H. Ulbricht, T. Hertel, *Phys. Rev. B* 69 (2004) 155406-155413.
- [114] J. J. de Miguel, R. Miranda, *J. Phys.: Condens. Matter* 14 (2002) 1063-1097.
- [115] F. Besenbacher, *Rep. Prog. Phys.* 59 (1996) 1737-1802.
- [116] T. Wölfle, A. Görling, W. Hieringer, *Phys. Chem. Chem. Phys.* 10 (2008) 5739-5742.
- [117] F. Buchner *et al.*, *ACS Nano* 3 (2009) 1789-1794.
- [118] Y. Bai *et al.*, *New J. Phys.* 11 (2009) 125004-125019.
- [119] L. Scudiero, D. E. Barlow, K. W. Hipps, *J. Phys. Chem. B* 106 (2002) 996-1003.
- [120] P. Borghetti *et al.*, *J. Chem. Phys.* 138 (2013) 144702-144711.

8 Abbreviations and symbols

8.1 Abbreviations

2HTPP	2H-5,10,15,20-Tetraphenylporphyrin
2HTPyP	2H-5,10,15,20-Tetra-(4-pyridyl)-porphyrin
2HTTBPP	2H-5,10,15,20-Tetrakis-(3,5-ditertbutyl-phenylporphyrin
DFT	Density Functional Theory
LEED	Low Energy Electron Diffraction
MTPP	M-5,10,15,20-Tetraphenylporphyrin (M = Co, Cu)
NEXAFS	Near Edge X-ray Adsorption Fine structure Spectroscopy
OEP	Octaethylporphyrin
QCM	Quartz Crystal Microbalance
QMS	Quadrupole Mass Spectrometer
RT	Room Temperature
STM	Scanning Tunneling Microscopy
STS	Scanning Tunneling Spectroscopy
TPD	Temperature Programmed Desorption
UHV	Ultra-High Vacuum
XPS	X-ray Photoelectron Spectroscopy

8.2 Symbols

$\langle(\Delta x)^2\rangle$	Mean-square Displacement
ΔH^\ddagger	Enthalpy
ΔS^\ddagger	Entropy
$2(l+s)$	Perimeter
A	Pre-exponential Factor

A_S	Pre-exponential Factor for Self-Metalation Reaction
A_m	Pre-exponential Factor for Migration
A_r	Pre-exponential Factor for Rotation
E_a	Energy Barrier for Activation
E_{des}	Desorption Energy
E_m	Energy Barrier for Migration
E_r	Energy Barrier for Rotation
E_s	Energy Barrier for Self-Metalation Reaction
h	Planck Constant
$h(t)$	Apparent Height at Time t
$h(T)$	Hopping Rate
I_{set}	Tunneling Current
k	Rate Constant
k_B	Boltzmann Constant
k_T	Metalation Rate
l/s	Aspect Ratio
n_r	Number of Rotations
n	Number of Transitions
$r(T)$	Rotation Rate
T	Temperature
t	Time
U_{bias}	Bias Voltage
α_{amin}	Inclination of aminic pyrrole ring
α_{imin}	Inclination of iminic pyrrole ring
θ	Twist Angle
κ	Transmission Factor
λ	Mean-square Jump Length
$v(T)$	Transition Rate
ρ	Molecular Density
ρ_0	Initial Molecular Density
ρ_t	Molecular Density at Time t
ϕ	Tilt Angle

9 Comparison of kinetic parameters

System	Method	Temperature [K]	Process	E [eV]	A [s^{-1}]	Reference
2HTPP/Cu(111)	STM	280-330	Diffusion	0.71±0.08	$10^{10.9±1.4}$	[P2]
2HTPyP/Cu(111)	STM	300-360	Diffusion			[27]
			Monomer	0.96±0.09	$1.4 \times 10^{12.±1.4}$	
			Dimer	0.94±0.03	$1.9 \times 10^{14±0.5}$	
CuPc/Ag(100)	STM	140-230	Diffusion	0.08±0.01	-	[110]
Ir(ppy) ₃ /Cu(111)	STM	65-94	Diffusion	0.20±0.01	$10^{11.3±0.6}$	[111]
PTCDA/Ag(100)	STM	235-310	Diffusion	0.15±0.04	-	[110]
PVBA/Pd(110)	STM	335-370	Diffusion	0.83±0.03	$10^{10.3±0.4}$	[36]
C ₆₀ /Pd(110)	STM	435-485	Diffusion	1.40±0.2	$10^{14.4±0.4}$	[112]
HtBDC/Cu(110)	STM		Diffusion	0.57±0.02	$10^{13.5±0.4}$	[37]
2HTPP/Cu(111)	STM	305-330	Rotation	1.28±0.12	$10^{17.0±1.8}$	[P2]
Dibutylsulfide/Au(111)	STM	8.3-12.5	Rotation	1.20±0.01	$7 \times 10^7 \pm 10^{0.3}$	[46]
2HTPP/Cu(111)	STM	390-410	Self-metalation/ Cu atoms	1.48±0.12	$10^{15.0±1.6}$	[P4]
D ₂ TPP/Ag(111)	TPD*	510	Metalation/ Zn atoms	1.39	-	[72]
2H-Porphyrin/Gas phase	DFT [#]	-	Metalation/ Cu atoms	1.03; 1.60	-	[72]
Benzene/HOPG	TPD*	151	Desorption	0.50±0.08	$1 \times 10^{16±3}$	[113]
Napthalene/HOPG	TPD*	235	Desorption	0.8±0.1	$5 \times 10^{16±2}$	
Coronene/HOPG	TPD*	390	Desorption	1.30±0.2	$2 \times 10^{16±2}$	
Ovalene/HOPG	TPD*	490	Desorption	22±0.2	$5 \times 10^{21±3}$	

Table 9.1: Compared values of activation energy E and pre-exponential factor A for organic molecules on well-defined surfaces. The yellow marked values are determined in this thesis.

* Analysis after Redhead equation.

[#] Values depending on the level of theory and applied basis sets: B3LYP/6-31G(d) and B3LYP/6-31-G(d,p)+LANL2DZ. [72]

System	Process	ΔH^\ddagger [eV]	ΔS^\ddagger [eV/K]	E [eV]	A [s ⁻¹]	
2HTPP/Cu(111)	Diffusion	0.68	$(-3.75) \cdot 10^{-4}$	0.71 ± 0.08	$10^{10.9 \pm 1.4}$	
2HTPP/Cu(111)	Rotation	1.25	$8.36 \cdot 10^{-4}$	1.28 ± 0.12	$10^{17.0 \pm 1.8}$	
2HTPP/Cu(111)	Self-Metalation	1.45	$4.39 \cdot 10^{-4}$	1.48 ± 0.12	$10^{15.0 \pm 1.6}$	
2HTTBPP/Cu(111)	Convex Row	Transition cvx→ccv	0.76 ± 0.11	$(-7.0 \pm 3.8) \cdot 10^{-4}$	0.79	$10^{9.3}$
		Transition ccv→cvx	0.92 ± 0.10	$(2.4 \pm 3.4) \cdot 10^{-4}$	0.95	$10^{14.0}$
		Transition cvx→ccv	0.72 ± 0.04	$(-3.4 \pm 1.4) \cdot 10^{-4}$	0.75	$10^{11.1}$
		Transition ccv→cvx	0.99 ± 0.04	$(3.6 \pm 1.4) \cdot 10^{-4}$	1.02	$10^{14.6}$

Table 9.2: Compared values for the kinetic parameters for the different dynamic processes analyzed in this thesis. For the diffusion, rotation and self-metalation the enthalpy and entropy values and for the transition the activation energies and pre-exponential factors are calculated after equation 3.3 with $T = 295$ K and $\kappa = 0$.

10 List of raw data

Figures	STM File	Figures	STM File	Figures	STM File
2.3 (a)	100118_02	4.7 (a), (b)	090729_29	4.14 (g)	121220_26
2.3 (b)	091027_03	4.7 (c), (d)	110603_79	4.14 (h)	121220_77
2.3 (c)	091104_17	4.8 (a)	090724_33	4.16 (a)	110509_23
2.7 (a)	090403_19	4.8 (b)	090724_25	4.16 (b)	110510_26
2.7 (b)	090403_21	4.8 (c)	090724_8-33	4.16 (c)	110510_86
3.1 (b)	090717_265-315	4.8 (d)	111021_158	4.17 (a)	110509_23
3.1 (c)	090717_78	4.8 (e)	111021_191	4.17 (b)	110603_79
3.1 (d)	090717_79	4.8 (f)	111021_157-208	4.17 (c)	110510_26
3.1 (f)	111216_169	4.9 (a)	090709_170-292	4.17 (d)	110510_86
3.1 (g)	090717_212-261	4.9 (b)	090717_85-156	4.18 (a)	101103_02
3.1 (h)	090717_212-261	4.9 (c)	090805_46-95	4.18 (b)	100129_162
3.4 (a) left	101223_276	4.9 (d)	090717_159-209	4.19 (a)	101117_1618
3.4 (a) right	101223_280	4.9 (e)	090717_211-261	4.22 (a) 1st	110120_86
3.4 (b) left	101207_2796	4.9 (f)	090717_265-315	4.22 (a) 2nd	110120_87
3.4 (b) right	101207_2797	4.11 (a)	110811_03	4.22 (a) 3rd	110120_88
4.1	071204_58	4.11 (b)	110808_11	4.22 (a) 4th	110120_89
4.2	090618_56	4.11 (c)	111216_112	4.23 (a)	100129_164
4.3 (a)	090903_63	4.12 (a)	111122_16	4.23 (b)	100303_60
4.3 (b)-(c)	090903_52-131	4.12 (b)	111122_133	4.23 (c)	100303_51
4.5 (a)	111214_205	4.12 (c)	111123_82	4.23 (d)	100219_47
4.5 (d)	111214_143-205	4.12 (d)	111128_15	4.24 (a)	090819_84
4.5 (b)	111216_170	4.12 (e)	111129_17	4.24 (b)	091104_117
4.5 (e)	111216_119-170	4.12 (f)	111201_21	4.24 (c)	090903_52-131
4.5 (c)	111222_28	4.14 (a)	121214_13	4.24 (d)	091030_7-57
4.5 (f)	111222_6-65	4.14 (b)	121214_50	4.25 (a), (b)	090420_60
4.5 (g)	110616_484	4.14 (c)	110603_06	4.25 (c) left	090609_21
4.6 (a)	091201_78	4.14 (d)	121215_83	4.25 (c) right	090615_15
4.6 (b)	111027_45	4.14 (e)	121217_44	4.26 (a)-(c)	090506_22
4.6 (c)	080131_20	4.14 (f)	121217_72		

Nomenclature of STM files according to yymmddxxxx (yy: year, mm: month, dd: day and xxxx: number)

11 Acknowledgment

Hereby, I would like to thank and acknowledge the following persons for supporting me throughout my thesis and for contributing to the results of this work.

In particular, I am grateful to my supervisors *Prof. Dr. Hans-Peter Steinrück*, for giving me the opportunity to work at his chair, for the numerous fruitful discussions and the great support and *PD Dr. Hubertus Marbach*, for interesting, valuable discussions and for always taking the time to support me with helpful ideas and input. For second assessment I thank *Prof. Dr. Alexander Schneider*.

Thanks to the *STM-Team*, *Dr. Florian Buchner*, *Michael Stark* and *Martin Drost*, for creating such a creative working atmosphere.

For good and fruitful collaborations, I would like to thank our *cooperation partners*:
The “Scienta-Team”, *Prof. Dr. Michael Gottfried*, *Dr. Ole Lytken*, *Dr. Jie Xiao*, *Michael Röckert* and *Min Chen* (Chair of Physical Chemistry II at the Friedrich-Alexander-Universität Erlangen-Nürnberg);
Prof. Dr. Görling, *PD Dr. Wolfgang Hieringer* and *Nicola Luckas* (Chair of Theoretical Chemistry at the Friedrich-Alexander-Universität Erlangen-Nürnberg);
Prof. Dr. Joachim Hornegger and *André Aichert* (Department of Computer Science, Pattern Recognition Lab at the Friedrich-Alexander-Universität Erlangen-Nürnberg);
Prof. Dr. Norbert Jux (Chair of Organic Chemistry II at the Friedrich-Alexander-Universität Erlangen-Nürnberg).

For technical support, I gratefully acknowledge *Hans-Peter Bäuml* (who spent many hours to improve the STM setup concerning noise and vibration), *Bernd Kreß*, *Friedhold Wölfel* and all the *members of the mechanical workshop*.

All the members of the Chair of Physical Chemistry II, I thank for the great working atmosphere.

A big thank you goes to the “*Fraunhofer IISB people*” for the cozy atmosphere and the funny stories at lunch, especially to *Martin Wenger*.

Finally, I would like to thank *my family Helga Gläβel and Hans Gläβel* who supported me not only throughout my thesis in manifold ways, but also throughout my studies and especially *Stefan Ditze*, my husband and soul mate, who is always there encouraging me.

Co-Authorship statement:

During my first years I collaborated closely together with *Dr. Florian Buchner*. He is the first author on the publications P1 and P2. Substantial contributions within this two publications, including data acquisition with the scanning tunneling microscope, data analysis (statistics, movie analysis) and input for the manuscript generation was performed by me.

In the framework of this thesis substantial novel results were conducted in collaboration with different Departments of the Friedrich-Alexander-Universität Erlangen-Nürnberg. The publications P3 and P5 present combined STM and XPS studies and therefore I share first authorship with *Michael Röckert* (P3) and *Dr. Jie Xiao* (P5) who did the XPS measurements.

A Appendix

- [P1] [Substrate-Mediated Phase Separation of Two Porphyrin Derivatives on Cu\(111\)](#)
F. Buchner, E. Zillner, M. Röckert, **S. Gläsel**, H.-P. Steinrück and H. Marbach
Chem. Eur. J. 17 (2011) 10226-10229
- [P2] [Diffusion, Rotation, and Surface Chemical Bond of Individual 2H-Tetraphenylporphyrin Molecules on Cu\(111\)](#)
F. Buchner, J. Xiao, E. Zillner, M. Chen, M. Röckert, **S. Ditze**, M. Stark,
H.-P. Steinrück, J. M. Gottfried and H. Marbach *J. Phys. Chem. C* 115 (2011)
24172-24177
- [P3] [Abrupt Coverage-Induced Enhancement of the Self-Metalation of Tetraphenylporphyrin with Cu\(111\)](#)
M. Röckert*, **S. Ditze***, M. Stark, J. Xiao, H.-P. Steinrück, H. Marbach,
and O. Lytken *J. Phys. Chem. C* 118 (2014) 1661-1667
- [P4] [Activation Energy for the Self-Metalation Reaction of 2H-Tetraphenylporphyrin on Cu\(111\)](#)
S. Ditze, M. Stark, M. Drost, F. Buchner, H.-P. Steinrück and H. Marbach
Angew. Chem., Int. Ed. 51 (2012) 10898-10901
[Bestimmung der Aktivierungsenergie für die Selbstmetallierungsreaktion von 2H-Tetraphenylporphyrin auf Cu\(111\)](#)
Angew. Chem. 124 (2012) 11056-11059

- [P5] [Temperature-Dependent Chemical and Structural Transformations from 2H-Tetraphenylporphyrin to Copper\(II\)-Tetraphenylporphyrin on Cu\(111\)](#)
J. Xiao*, **S. Ditze***, M. Chen, F. Buchner, M. Stark, M. Drost, H.-P. Steinrück, J. M. Gottfried and H. Marbach *J. Phys. Chem. C* 116 (2012) 12275-12282
- [P6] [On the Energetics of Conformational Switching of Molecules at and Close to Room Temperature](#)
S. Ditze, M. Stark, F. Buchner, A. Aichert, N. Jux, N. Luckas, A. Görling, W. Hieringer, J. Hornegger, H.-P. Steinrück and H. Marbach *J. Am. Chem. Soc.* 136 (2014) 1609-1616
- [P7] [Towards the engineering of molecular nanostructures: local anchoring and functionalization of porphyrins on model-templates](#)
S. Ditze, M. Röckert, F. Buchner, E. Zillner, M. Stark, H.-P. Steinrück and H. Marbach *Nanotechnology* 24 (2013) 115305-115316

* These authors contributed equally to this contribution and share first authorship.